

Neutrinos and the Stars

GEORG G. RAFFELT

*Max-Planck-Institute für Physik (Werner-Heisenberg-Institut)
Föhringer Ring 6, 80805 München, Germany*

Summary. — The role of neutrinos in stars is introduced for students with little prior astrophysical exposure. We begin with neutrinos as an energy-loss channel in ordinary stars and conversely, how stars provide information on neutrinos and possible other low-mass particles. Next we turn to the Sun as a measurable source of neutrinos and other particles. Finally we discuss supernova (SN) neutrinos, the SN 1987A measurements, and the quest for a high-statistics neutrino measurement from the next nearby SN. We also touch on the subject of neutrino oscillations in the high-density SN context.

1. – Introduction

Neutrinos were first proposed in 1930 by Wolfgang Pauli to explain, among other problems, the missing energy in nuclear beta decay. Towards the end of that decade, the role of nuclear reactions as an energy source for stars was recognized and the hydrogen fusion chains were discovered by Bethe [1] and von Weizsäcker [2]. It is intriguing, however, that these authors did not mention neutrinos—for example, Bethe writes the fundamental pp reaction in the form $H + H \rightarrow D + e^+$. It was Gamow and Schoenberg in 1940 who first stressed that stars must be powerful neutrino sources because beta processes play a key role in the hydrogen fusion reactions and because of the feeble

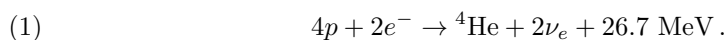
neutrino interactions that allow them to escape unscathed [3]. Moreover, the idea that supernova explosions had something to do with stellar collapse and neutron-star formation had been proposed by Baade and Zwicky in 1934 [5], and Gamow and Schoenberg (1941) developed a first neutrino theory of stellar collapse [4]. Solar neutrinos were first measured by Ray Davis with his Homestake radiochemical detector that produced data over a quarter century 1970–1994 [6] and since that time solar neutrino measurements have become routine in many experiments. The neutrino burst from stellar collapse was observed only once when the star Sanduleak –69 202 in the Large Magellanic Cloud, about 160,000 light years away, exploded on February 23, 1987 (Supernova 1987A). The Sun and SN 1987A remain the only measured astrophysical neutrino sources.

Stars for sure are prime examples for neutrinos being of practical relevance in nature. The smallness of neutrino masses compared with stellar temperatures ensures their role as radiation. The weak interaction strength ensures that neutrinos freely escape once produced, except for the case of stellar core collapse where even neutrinos are trapped, but still emerge from regions where nothing else can directly carry away information except gravitational waves. The properties of stars themselves can sometimes provide key information about neutrinos or the properties of other low-mass particles that may be emitted in analogous ways. The Sun is used as a source of experimental neutrino or particle measurements. The SN 1987A neutrino burst has provided a large range of particle-physics limits. Measuring a high-statistics neutrino light curve from the next nearby supernova will provide a bonanza of astrophysical and particle-physics information. The quest for such an observation and measuring the diffuse neutrino flux from all past supernovae are key targets for low-energy neutrino astronomy.

The purpose of these lectures is to introduce an audience of young neutrino researchers, with not much prior exposure to astrophysical concepts, to the role of neutrinos in stars and conversely, how stars can be used to gain information about neutrinos and other low-mass particles that can be emitted in similar ways. We will describe the role of neutrinos in ordinary stars and concomitant constraints on neutrino and particle properties (Section 2). Next we turn to the Sun as a measurable neutrino and particle source (Section 3). The third topic are collapsing stars and the key role of supernova neutrinos in low-energy neutrino astronomy (Section 4).

2. – Neutrinos from ordinary stars

2.1. *Some basics of stellar evolution.* – An ordinary star like our Sun is a self-gravitating ball of hot gas. It can liberate gravitational energy by contraction, but of course its main energy source is nuclear binding energy. During the initial phase of hydrogen burning, the effective reaction is



In detail, the reactions can proceed through the pp chains (Table I) or the CNO cycle (Table II). The latter contributes only a few percent in the Sun, but dominates in slightly

TABLE I. – *Hydrogen burning by pp chains.*

Termination	Reaction	Branching (Sun)	Neutrino Energy [MeV]	Name
PP I	$p + p \rightarrow d + e^+ + \nu_e$	99.6%	< 0.423	pp
	$p + e^- + p \rightarrow d + \nu_e$	0.44%	1.445	pep
	$d + p \rightarrow {}^3\text{He} + \gamma$			
	${}^3\text{He} + {}^3\text{He} \rightarrow {}^4\text{He} + 2p$	85%		
PP II	${}^3\text{He} + {}^4\text{He} \rightarrow {}^7\text{Be}$	15%		
	${}^7\text{Be} + e^- \rightarrow {}^7\text{Li} + \nu_e$	90%	0.863	Beryllium
	${}^7\text{Be} + e^- \rightarrow {}^7\text{Li}^* + \nu_e$	10%	0.385	Beryllium
	${}^7\text{Li} + p \rightarrow {}^4\text{He} + {}^4\text{He}$			
PP III	${}^7\text{Be} + p \rightarrow {}^8\text{B} + \gamma$	0.02%		
	${}^8\text{B} + p \rightarrow {}^8\text{Be}^* + e^+ + \nu_e$		< 15	Boron
	${}^8\text{Be}^* \rightarrow {}^4\text{He} + {}^4\text{He}$			
hep	${}^3\text{He} + p \rightarrow {}^4\text{He} + e^+ + \nu_e$	3×10^{-7}	< 18.8	hep

more massive stars due to its steep temperature dependence. Neutrinos carry away a few percent of the energy, in detail depending on the reaction channels. Based on the solar photon luminosity of ⁽¹⁾ $L_\odot = 3.839 \times 10^{33}$ erg s⁻¹ one can easily estimate the solar neutrino flux at Earth to be about 6.6×10^{10} cm⁻² s⁻¹.

In the simplest case we model a star as a spherically symmetric static structure, excluding phenomena such as rotation, convection, magnetic fields, dynamical evolution such as supernova explosion, and so forth. Stellar structure is then governed by three conditions. The first is hydrostatic equilibrium, i.e. at each radius r the pressure P must balance the gravitational weight of the material above, or in differential form

$$(2) \quad \frac{dP}{dr} = -\frac{G_N M_r \rho}{r^2},$$

where G_N is Newton's constant, ρ the local mass density, and $M_r = \int_0^r dr' \rho(r') 4\pi r'^2$ the integrated stellar mass up to radius r .

Energy conservation implies that the energy flux L_r flowing through a spherical surface at radius r can only change if there are local sources or sinks of energy,

$$(3) \quad \frac{dL_r}{dr} = 4\pi r^2 \epsilon \rho.$$

The local rate of energy generation ϵ , measured in erg g⁻¹ s⁻¹, is the sum of nuclear and gravitational energy release, reduced by neutrino losses, $\epsilon = \epsilon_{\text{nuc}} + \epsilon_{\text{grav}} - \epsilon_\nu$.

⁽¹⁾ Following astrophysical convention, we will use cgs units, often mixed with natural units, where $\hbar = c = k_B = 1$.

TABLE II. – *Hydrogen burning by the CNO cycle.*

Reaction	Neutrino Energy [MeV]
$^{12}\text{C} + p \rightarrow ^{13}\text{N} + \gamma$	
$^{13}\text{N} \rightarrow ^{13}\text{C} + e^+ + \nu_e$	< 1.199
$^{13}\text{C} + p \rightarrow ^{14}\text{N} + \gamma$	
$^{14}\text{N} + p \rightarrow ^{15}\text{O} + \gamma$	
$^{15}\text{O} \rightarrow ^{15}\text{N} + e^+ + \nu_e$	< 1.732
$^{15}\text{N} + p \rightarrow ^{12}\text{C} + ^4\text{He}$	

Finally the flow of energy is driven by a temperature gradient. If most of the energy is carried by electromagnetic radiation—certainly true at the stellar surface—we may express the thermal energy density by that of the radiation field in the form $\rho_\gamma = aT^4$ where the radiation-density constant is $a = 7.57 \times 10^{-15} \text{ erg cm}^{-3} \text{ K}^{-4}$ or in natural units $a = \pi^2/15$. The flow of energy is then

$$(4) \quad L_r = \frac{4\pi r^2}{3\kappa\rho} \frac{d(aT^4)}{dr},$$

where κ (units $\text{cm}^2 \text{ g}^{-1}$) is the opacity. The photon contribution (radiative opacity) is $\kappa_\gamma\rho = \langle \lambda_\gamma \rangle_{\text{Rosseland}}^{-1}$. In other words, $(\kappa_\gamma\rho)^{-1}$ is a spectral average (“Rosseland mean”) of the photon mean free path λ_γ . Radiative transfer corresponds to photons carrying energy in a diffusive way with typical step size λ_γ . Energy is also carried by electrons (“conduction”), the total opacity being $\kappa^{-1} = \kappa_\gamma^{-1} + \kappa_c^{-1}$.

In virtually all stars there are regions that are convectively unstable and energy transport is dominated by convection, a phenomenon that breaks spherical symmetry. In practice, convection is treated with approximation schemes. In our Sun, the outer layers beyond about $0.7 R_\odot$ (solar radius) are convective.

The stellar structure equations must be solved with suitable boundary condition at the center and stellar surface. From nuclear, neutrino and atomic physics calculations one needs the energy-generation rate ϵ and the opacity κ , both depending on density, temperature and chemical composition. In addition one needs the equation of state, relating the thermodynamic quantities P , ρ and T , again depending on chemical composition. For detailed discussions we refer to the textbook literature [7, 8].

However, simple reasoning can reveal deep insights without solving the full problem. For a self-gravitating system, the virial theorem is one of those fundamental propositions that explain many puzzling features. One way of deriving it in our context is to begin with the equation of hydrostatic equilibrium in eq. (2) and integrate both sides over the entire star, $\int_0^R dr 4\pi r^3 P' = -\int_0^R dr 4\pi r^3 G_N M_r \rho / r^2$ where $P' = dP/dr$. The rhs is the gravitational binding energy E_{grav} of the star. After partial integration of the lhs with the boundary condition $P = 0$ at the surface, one finds $-3 \int_0^R dr 4\pi r^2 P = E_{\text{grav}}$. If we model the stellar medium as a monatomic gas we have the relationship $P = \frac{2}{3} U$ between

pressure and density of internal energy, so the lhs is simply twice the total internal energy which is the sum over the kinetic energies of the gas particles. Then the average energy of a single “atom” of the gas and its average gravitational energy are related by

$$(5) \quad \langle E_{\text{kin}} \rangle = -\frac{1}{2} \langle E_{\text{grav}} \rangle.$$

This is the virial theorem for a simple self-gravitating system and can be applied to everything from stars to clusters of galaxies.

In the latter case, Fritz Zwicky (1933) was the first to study the motion of galaxies that form gravitationally bound systems. We may write $E_{\text{kin}} = \frac{1}{2} m v^2$ and $E_{\text{grav}} = G_{\text{N}} M_r m r^{-1}$ so that the virial theorem reads $\langle v^2 \rangle = G_{\text{N}} M \langle r^{-1} \rangle$. The lhs is the velocity dispersion revealed by Doppler shifts of spectral lines whereas the geometric size of the cluster is directly observed. This allowed Zwicky to estimate the total gravitating mass M of the Coma cluster. It turned out to be far larger than luminous matter, leading to the proposition of large amounts of dark matter in the universe [9].

We next apply the virial theorem to the Sun and estimate its interior temperature. We approximate the Sun as a homogeneous sphere of mass $M_{\odot} = 1.99 \times 10^{33}$ g and radius $R_{\odot} = 6.96 \times 10^{10}$ cm. The gravitational potential of a proton near the center is $E_{\text{grav}} = -\frac{3}{2} G_{\text{N}} M_{\odot} m_p / R_{\odot} = -3.2$ keV. In thermal equilibrium we have $\langle E_{\text{kin}} \rangle = \frac{3}{2} k_{\text{B}} T$, so the virial theorem implies $\frac{3}{2} k_{\text{B}} T = -\frac{1}{2} E_{\text{grav}} = -3.2$ keV or $T \sim 1.1$ keV. This is to be compared with $T_{\text{c}} = 1.56 \times 10^7$ K = 1.34 keV for the central temperature in standard solar models. Without any detailed modeling we have correctly estimated the thermal energy scale relevant for the solar interior and thus for hydrogen burning.

A crucial feature of a self-gravitating system is its “negative heat capacity.” The total energy $\langle E_{\text{kin}} + E_{\text{grav}} \rangle = \frac{1}{2} \langle E_{\text{grav}} \rangle$ is negative. Extracting energy from such a system and letting it relax to virial equilibrium leads to contraction and an *increase* of the average kinetic energy, i.e. to heating. Conversely, pumping energy into the system leads to expansion and cooling. In this way a star self-regulates its nuclear burning processes. If the “fusion reactor” overheats, it builds up pressure, expands and thereby cools, or conversely, if it underperforms it loses pressure, contracts, heats, and thereby increases the fusion rates and thus the pressure.

Nuclear reactions can only occur if the participants approach each other enough for nuclear forces to come into play. To this end nuclei must penetrate the Coulomb barrier. The quantum-mechanical tunneling probability is proportional to $E^{-1/2} e^{-2\pi\eta}$ where $\eta = (m/2E)^{1/2} Z_1 Z_2 e^2$ is the Sommerfeld parameter with m the reduced mass of the two-body system with nuclear charges $Z_1 e$ and $Z_2 e$. Usually one expresses the relevant nuclear cross sections in terms of the astrophysical S-factor $S(E) = \sigma(E) E e^{2\pi\eta(E)}$ which is then a slowly varying function of CM energy E . Thermonuclear reactions take place in a narrow range of energies (“Gamow peak”) that arises from the convolution of the tunneling probability with the thermal velocity distribution. For more than a decade, the relevant low-energy cross sections have been measured in the laboratory, notably the LUNA experiment in the Gran Sasso underground laboratory. Their first results for the

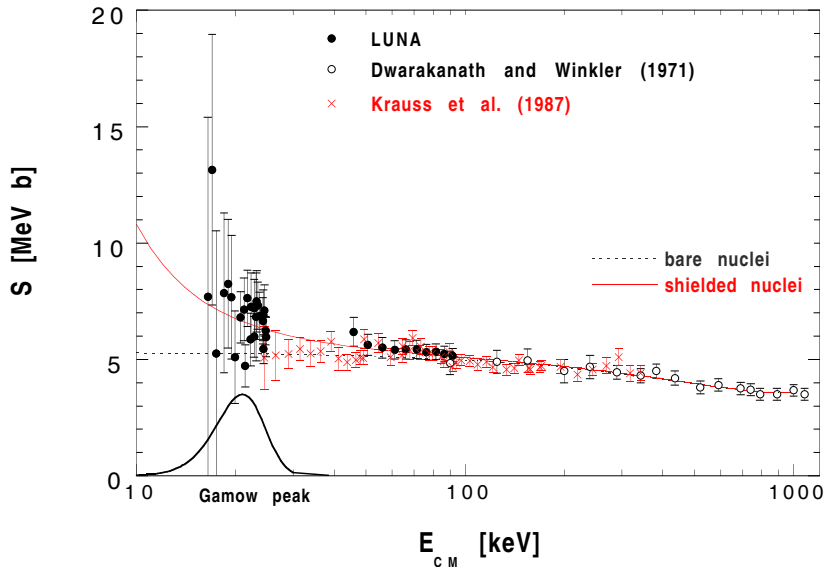


Fig. 1. – First measurements of the ${}^3\text{He} + {}^3\text{He} \rightarrow {}^4\text{He} + 2p$ cross section by the LUNA collaboration [10], together with some previous measurements. The solar Gamow peak is shown in arbitrary units.

${}^3\text{He} + {}^3\text{He}$ fusion cross section [10] are shown in fig. 1 together with the solar Gamow peak. The temperature is about 1 keV, whereas the reaction probability peaks for CM energies of some 20 keV. Thermonuclear reactions depend steeply on temperature: If it is too low, nothing happens, if it were too high, energy generation would be explosive.

One consequence is that hydrogen burning always occurs at roughly the same $T \sim 1$ keV. As discussed earlier, T in the star essentially corresponds to a typical gravitational potential by the virial theorem. Since $E_{\text{grav}} \propto M/R$ where M is the stellar mass and R its radius, this ratio should be roughly the same for all hydrogen burning stars and thus the stellar radius scales roughly linearly with mass.

Once a star has burnt its hydrogen, helium burning sets in which proceeds by the triple alpha reaction ${}^4\text{He} + {}^4\text{He} + {}^4\text{He} \rightarrow {}^8\text{Be} + {}^4\text{He} \rightarrow {}^{12}\text{C}$. There is no stable isotope of mass number 8 and ${}^8\text{Be}$ builds up with a very small concentration of about 10^{-9} . Additional reactions are ${}^{12}\text{C} + {}^4\text{He} \rightarrow {}^{16}\text{O}$ and ${}^{16}\text{O} + {}^4\text{He} \rightarrow {}^{20}\text{Ne}$. Helium burning is extremely temperature sensitive and occurs approximately at $T \sim 10^8$ K, corresponding roughly to 10 keV. The next phase is carbon burning which proceeds by many reactions, for example ${}^{12}\text{C} + {}^{12}\text{C} \rightarrow {}^{23}\text{Na} + p$ or ${}^{12}\text{C} + {}^{12}\text{C} \rightarrow {}^{20}\text{Ne} + {}^4\text{He}$. It burns at $T \sim 10^9$ K, corresponding roughly to 100 keV.

Stable thermonuclear burning, for the different burning phases, occurs in a characteristic narrow range of temperatures, but broad range of densities. Every star initially contains about 25% helium, originating from the big bang, and builds up more by hydrogen burning, but helium burning will not occur at the hydrogen-burning temperatures,

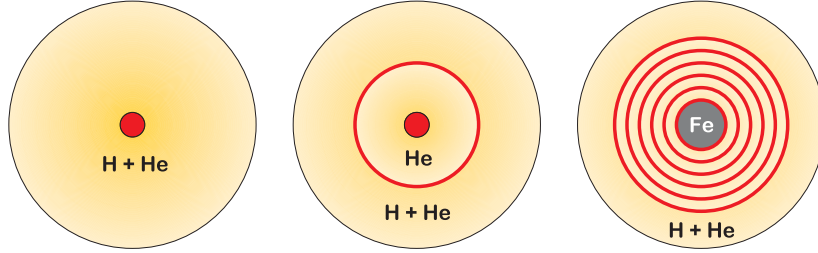


Fig. 2. – Schematic structure of hydrogen and helium burning stars and final “onion skin structure” before core collapse.

and conversely, at the helium-burning T , hydrogen burning would be explosive. Different burning phases must occur in separate regions with different T . When a star exhausts hydrogen in its center, it will make a transition to helium burning which then occurs in its center, but hydrogen burning continues in a shell inside of which we have only helium, outside a mixture of hydrogen and helium (fig. 2). When helium is exhausted in the center, carbon burning is ignited, and so forth. A star more massive than about $6\text{--}8 M_{\odot}$ goes through all possible burning stages until an iron core is produced. As iron is the most tightly bound nucleus, no further burning phase can be ignited.

A normal star is supported by thermal pressure, allowing for self-regulated nuclear burning as explained earlier. A stable configuration without nuclear burning is also possible when the star supports itself by electron degeneracy pressure (white dwarfs). The number density of a cold electron gas is related to the maximum momentum, the Fermi momentum p_F , by $n_e = p_F^3/(3\pi^3)$. A typical electron velocity is then $v = p_F/m_e$, assuming electrons are non-relativistic. The pressure P is proportional to the number density times a typical momentum times a typical velocity and thus $P \propto p_F^5 \propto \rho^{5/3} \propto M^{5/3} R^{-5}$ where we have used that $\rho \propto M R^{-3}$. If we approximate the pressure gradient as $dP/dR \sim P/R$, together with the equation of hydrostatic equilibrium, leads to $P \propto G_N M \rho R^{-1} \propto M^2 R^{-4}$. We have already found $P \propto M^{5/3} R^{-5}$ and the two conditions are consistent for $R \propto M^{-1/3}$. In contrast to normal stars, white dwarfs are smaller for larger mass. From polytropic stellar models one finds numerically

$$(6) \quad R = 10,500 \text{ km} \left(\frac{0.6 M_{\odot}}{M} \right)^{1/3} (2Y_e)^{5/3},$$

where Y_e is the number of electrons per nucleon. In other words, a white dwarf is roughly the size of the Earth for roughly the mass of the Sun.

The inverse mass-radius relation fundamentally derives from electrons producing more pressure if they are squeezed into smaller space, a manifestation of Heisenberg’s uncertainty relation together with Pauli’s exclusion principle. However, if the white-dwarf mass becomes too large and therefore its size very small, eventually electrons become relativistic. In this case their typical velocity is the speed of light and no longer

$v = p_F/m_e$. We lose one power of p_F in the expression for the pressure that becomes $P \propto p_F^4 \propto \rho^{4/3} \propto M^{4/3} R^{-4}$. We no longer obtain a relation between M and R , meaning that there is no stable configuration. In polytropic models one finds explicitly for the limiting white-dwarf mass, the Chandrasekhar limit,

$$(7) \quad M_{\text{Ch}} = 1.457 M_{\odot} (2Y_e)^2.$$

This result, combining quantum mechanics with relativistic effects, was derived by the young Subrahmanyan Chandrasekhar on his way from India to England in 1930 and was published the following year [11]. This fundamental finding was initially ridiculed by the experts, but later helped Chandrasekhar win the 1983 physics Nobel prize.

We finally mention “giant stars” as another important phenomenon of stellar structure. A normal star like our Sun has a monotonically decreasing density from the center to the surface, but on the crudest level of approximation could be described as a homogeneous sphere. On the other hand a star with a core, especially with a small degenerate core, tends to have a hugely inflated envelope and is then a giant star. This behavior follows from the stellar structure equations, but cannot be explained in a few sentences with a simple physical reason. When a low-mass hydrogen-burning star like our Sun has exhausted hydrogen in its center, it will develop a degenerate helium core and at the same time expand its envelope and become a red giant. (For a given luminosity and an expanding surface area, the surface temperature must decline because thermal radiation, by the Stefan-Boltzmann-law, is proportional to the surface area and T^4 .)

We can now roughly understand how stars live and die. If the mass is too small, roughly below 8% of the solar mass, hydrogen burning never ignites, the star contracts and “browns out”, eventually forming a degenerate hydrogen star (table III). For masses up to about $0.8 M_{\odot}$, hydrogen burning will not finish within the age of the universe and even the oldest such stars are still around today. For masses up to a few M_{\odot} , stars ignite helium burning. After its completion they develop a degenerate carbon-oxygen core and

TABLE III. – *Evolution of stars, depending on their initial mass.*

Mass Range	Evolution	End State
$M \lesssim 0.08 M_{\odot}$	Hydrogen burning never ignites	Brown Dwarf
$0.08 M_{\odot} \lesssim M \lesssim 0.8 M_{\odot}$	Hydrogen burning not completed in Hubble time	Low-mass main-sequence star
$0.8 M_{\odot} \lesssim M \lesssim 2 M_{\odot}$	Degenerate helium core after hydrogen exhaustion	Carbon-oxygen white dwarf surrounded by planetary nebula
$2 M_{\odot} \lesssim M \lesssim 6-8 M_{\odot}$	Helium ignition non-degenerate	Neutron star (often pulsar)
$6-8 M_{\odot} \lesssim M$	All burning phases → Onion skin structure → Core-collapse supernova	Sometimes black hole Supernova remnant (SNR) e.g. crab nebula

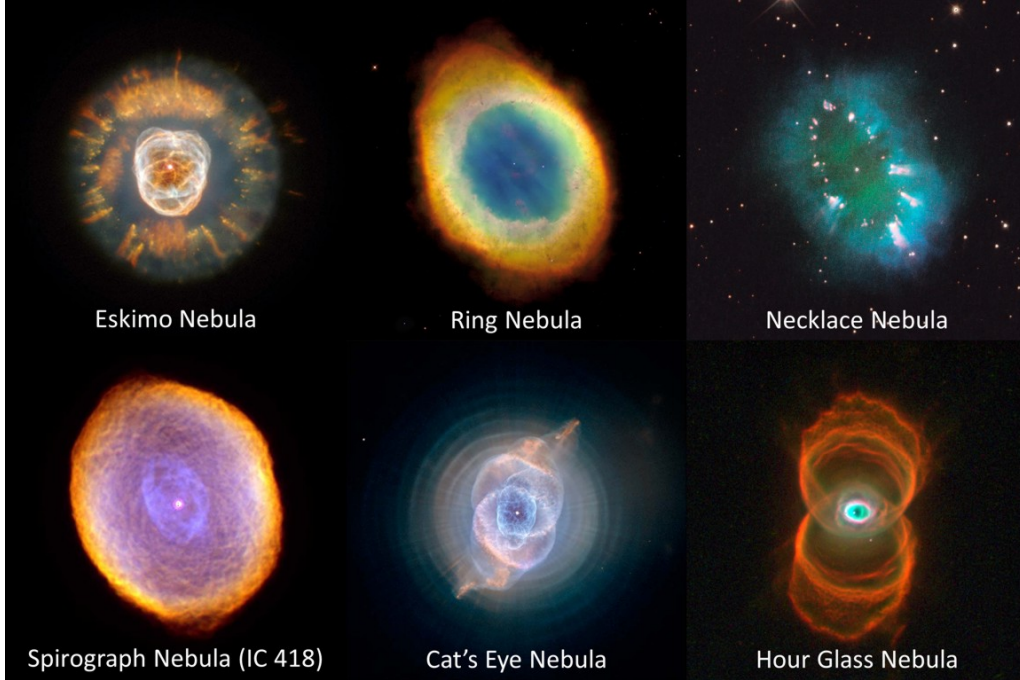


Fig. 3. – Several planetary nebulae, the remnants of stars with initial masses of a few M_{\odot} . Image credits: Necklace and Cat’s Eye Nebula: NASA, ESA, HEIC, and The Hubble Heritage Team (STScI/AURA). Ring Nebula and IC418: NASA and The Hubble Heritage Team (STScI/AURA). Hour Glass Nebula: NASA, R. Sahai, J. Trauger (JPL), and The WFPC2 Science Team. Eskimo Nebula: NASA, A. Fruchter and the ERO Team (STScI).

inflate so much that they shed their envelope, forming what is called a “planetary nebula” with a carbon-oxygen white dwarf as a central star. Planetary nebulae are among the most beautiful astronomical objects (fig. 3). White dwarfs then cool and become ever darker with increasing age. For initial masses above $6\text{--}8 M_{\odot}$, stars will go through all burning phases and eventually develop a degenerate iron core which will grow in mass (and shrink in size) until it reaches the Chandrasekhar limit and collapses, leading to a core-collapse supernova to be discussed later.

2.2. Neutrino emission processes. – During hydrogen burning, for every produced helium nucleus one needs to convert two protons into two neutrons, so inevitably two neutrinos with MeV-range energies emerge. Advanced burning stages consist essentially of combining α particles to larger nuclei and do not produce neutrinos in nuclear reactions. However, neutrinos are still produced by several “thermal processes” that actually dominate the stellar energy losses for carbon burning and more advanced phases.

Thermal neutrino emission arises from processes involving electrons, nuclei and photons of the medium and are based on the neutrino interaction with electrons. Fun-

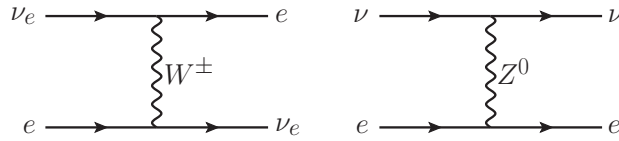


Fig. 4. – Interaction of neutrinos with electrons by W exchange (charged current) and Z exchange (neutral current).

damentally this corresponds to either W or Z exchange (fig. 4). For the low energies characteristic of stellar interiors and even in the collapsed core of a supernova, one can integrate out W and Z and describe neutrino interactions with electrons and nucleons by an effective four-fermion neutral-current interaction of the form

$$(8) \quad \mathcal{H}_{\text{int}} = \frac{G_{\text{F}}}{\sqrt{2}} \bar{\psi}_f \gamma_{\mu} (C_V - C_A \gamma_5) \psi_f \bar{\psi}_{\nu} \gamma^{\mu} (1 - \gamma_5) \psi_{\nu},$$

where $G_{\text{F}} = 1.16637 \times 10^{-5} \text{ GeV}^{-2}$ is the Fermi constant. When f is a charged lepton and ν the corresponding neutrino, this effective neutral-current interaction includes a Fierz-transformed contribution from W exchange. The compound effective $C_{V,A}$ values are given in table IV. (Note that the $C_{V,A}$ for neutral currents are typically $\pm 1/2$, a factor that is sometimes pulled out so that the overall coefficient becomes $G_{\text{F}}/2\sqrt{2}$ and $C_{V,A}$ are twice the values shown in table IV.) For neutrinos interacting with the same flavor, a factor 2 for an exchange amplitude for identical fermions was included. The C_A values for nucleons are often taken to be $\pm 1.26/2$, derived by isospin invariance from the charged-current values. However, the strange-quark contribution to the nucleon spin implies an isoscalar piece as well [13], giving rise to the values shown in table IV. For the effective weak mixing angle a value $\sin^2 \Theta_{\text{W}} = 0.23146$ was used [14].

In the early history of neutrino physics it was thought that neutrinos would be produced only in nuclear β -decay. After Fermi formulated the $V-A$ theory in the late 1950s, however, it became clear that neutrinos could have a direct coupling to electrons, which today we understand as an effective low-energy interaction. Around 1961–63 these ideas led to the proposition of thermal neutrino processes in stars shown in fig. 5, i.e. plasmon

TABLE IV. – *Effective neutral-current couplings for the interaction Hamiltonian of eq. (8).*

Fermion f	Neutrino	C_V	C_A	C_V^2	C_A^2
Electron	ν_e	$+1/2 + 2 \sin^2 \Theta_{\text{W}}$	$+1/2$	0.9376	0.25
	$\nu_{\mu,\tau}$	$-1/2 + 2 \sin^2 \Theta_{\text{W}}$	$-1/2$	0.0010	0.25
Proton	$\nu_{e,\mu,\tau}$	$+1/2 - 2 \sin^2 \Theta_{\text{W}}$	$+1.37/2$	0.0010	0.47
Neutron	$\nu_{e,\mu,\tau}$	$-1/2$	$-1.15/2$	0.25	0.33
Neutrino (ν_a)	ν_a	$+1$	$+1$	1.00	1.00
	$\nu_{b \neq a}$	$+1/2$	$+1/2$	0.25	0.25

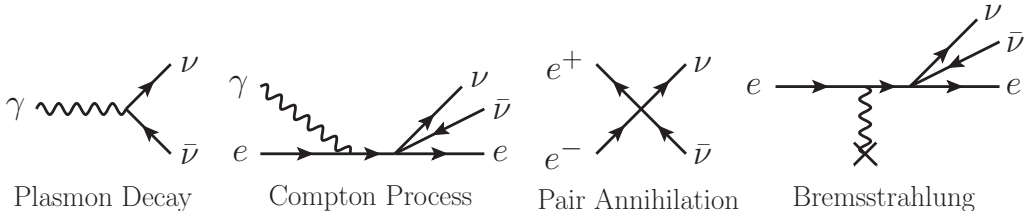


Fig. 5. – Thermal neutrino emission processes in stars.

decay, the photo or Compton production process, pair annihilation, and bremsstrahlung by electrons interacting with nuclei or other electrons. While thermal neutrino emission is negligible in the Sun, the steep temperature dependence of the emission rate implies large neutrino losses in more advanced burning stages where neutrino losses are much more important than surface photon emission (table V). This means that without neutrino losses such giant stars should live much longer and hence one should see more of them in the sky relative to ordinary stars than are actually observed. Richard Stothers (1970) used this argument to show that indeed the direct neutrino-electron interaction should be roughly governed by the same constant G_F as nuclear β decay [15]. Neutral-current interactions were first experimentally observed in 1973 in the Gargamelle bubble chamber at CERN [16].

Once neutrinos have a direct coupling to electrons (in the sense of our low-energy effective theory), the existence of these processes is obvious, except for the plasmon decay which seems impossible because the decay of massless particles (photons) is kinematically forbidden and neutrinos do not interact with photons. However, a photon propagating in a medium has a nontrivial dispersion relation that can be “time like”, $\omega^2 - k^2 > 0$, or “space like”, $\omega^2 - k^2 < 0$. In the former case, typical for a stellar plasma, one may say that the photon has an effective mass in the medium and a decay $\gamma \rightarrow \nu\bar{\nu}$ is kinematically allowed. In the latter case, typical for visible light in air or water, the process $e \rightarrow e + \gamma$ is kinematically allowed and is identical with the well-known Cherenkov effect: a high-energy charged particle moving in water or air emits detectable light.

TABLE V. – Major burning stages of a $15 M_\odot$ star and thermal neutrino losses [12].

Burning stage	Dominant process	T_c [keV]	ρ_c [g/cm ³]	L_γ [$10^4 L_\odot$]	L_ν/L_γ	Duration [years]
Hydrogen	H \rightarrow He	3	5.9	2.1	—	1.2×10^7
Helium	He \rightarrow C, O	14	1.3×10^3	6.0	1.7×10^{-5}	1.3×10^6
Carbon	C \rightarrow Ne, Mg	53	1.7×10^5	8.6	1.0	6.3×10^3
Neon	Ne \rightarrow O, Mg	110	1.6×10^7	9.6	1.8×10^3	7.0
Oxygen	O \rightarrow Si	160	9.7×10^7	9.6	2.1×10^4	1.7
Silicon	Si \rightarrow Fe, Ni	270	2.3×10^8	9.6	9.2×10^5	6 days

In a non-relativistic plasma, typical for ordinary stars, the photon dispersion relation is that of a particle with a mass corresponding to the plasma frequency,

$$(9) \quad \omega^2 - k^2 = \omega_{\text{pl}}^2 \quad \text{where} \quad \omega_{\text{pl}}^2 = \frac{4\pi\alpha n_e}{m_e}.$$

Here m_e and n_e are the electron mass and number density. The general dispersion relation in a relativistic and/or degenerate medium is more complicated [17], but for large photon energies always that of a massive particle. A photon in a medium is sometimes called “transverse plasmon.” In addition there exists a propagating mode with longitudinal polarization called “longitudinal plasmon” or simply “plasmon.” It has no counterpart in vacuum and corresponds to the negative and positive electric charges of the plasma oscillating coherently against each other.

An effective neutrino-photon coupling is mediated by the electrons of the medium. Photon decay can be viewed as the Compton process (fig. 5) when the incoming and outgoing electron have identical momenta, i.e. the electron scatters forward. The electron can then be integrated out to produce an effective neutrino-photon interaction. The main contribution arises from the neutrino-electron vector coupling, so that the truncated matrix element producing the photon mass and the neutrino-photon coupling are actually the same.

Neutrino emission rates have been calculated by different authors over the years and numerical approximation formulas have been derived. In a heroic effort over a decade, neutrino emission rates were calculated and put into numerically useful form for all relevant conditions and processes by N. Itoh and collaborators [18], for the plasma process see Refs. [19, 20]. Different processes dominate in different regions of temperature and density (fig. 6). In cold and dense matter as exists in old white dwarfs, bremsstrahlung dominates where correlation effects among nuclei become very important.

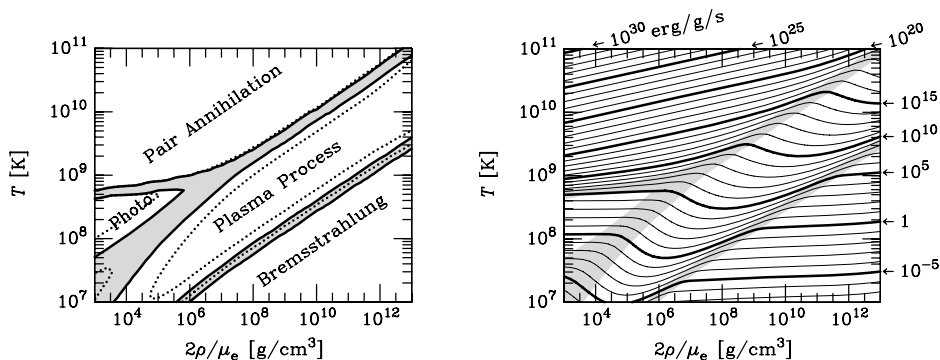


Fig. 6. – Relative dominance of different neutrino emission processes (left) and contours for total energy-loss rate (right). μ_e is the electron “mean molecular weight,” i.e. roughly the number of baryons per electron. Bremsstrahlung depends on the chemical composition (solid lines for helium, dotted lines for iron, right panel for helium).

2.3. Neutrino electromagnetic properties. – The plasmon decay process is an important neutrino emission process in a broad range of temperature and density even though neutrinos do not couple directly to photons. One may speculate, however, that neutrinos could have nontrivial electromagnetic properties, notably magnetic dipole moments, allowing the plasma process to be more efficient. Bernstein, Ruderman and Feinberg (1963) showed that one can then use the observed properties of stars to constrain the possible amount of additional energy loss and thus neutrino electromagnetic properties [21].

Considering all possible interaction structures of a fermion field ψ with the electromagnetic field, one can think of four different terms,

$$(10) \quad \mathcal{L}_{\text{eff}} = -F_1 \bar{\psi} \gamma_\mu \psi A^\mu - G_1 \bar{\psi} \gamma_\mu \gamma_5 \psi \partial_\nu F^{\mu\nu} \\ - \frac{1}{2} F_2 \bar{\psi} \sigma_{\mu\nu} \psi F^{\mu\nu} - \frac{1}{2} G_2 \bar{\psi} \sigma_{\mu\nu} \gamma_5 \psi F^{\mu\nu},$$

where A^μ is the electromagnetic field and $F^{\mu\nu}$ the field-strength tensor. In a matrix element, the coefficients $F_{1,2}$ and $G_{1,2}$ are functions of the energy-momentum transfer Q^2 and play the role of form factors. In the limit $Q^2 \rightarrow 0$, the meaning of the form factors is that of an electric charge $e_\nu = F_1(0)$, an anapole moment $G_1(0)$, a magnetic dipole moment $\mu = F_2(0)$ and an electric dipole moment $\epsilon = G_2(0)$. In the standard model, neutrinos are of course electrically neutral and $F_1(0) = 0$. The anapole moment also vanishes and for non-vanishing Q^2 the form factors F_1 and G_1 represent radiative corrections to the tree-level couplings.

The F_2 and G_2 form factors couple left- with right-handed fields and vanish if all neutrino interactions are purely left-handed as would be the case for massless neutrinos in the standard model. Today we know that neutrinos have small masses, and hence small dipole moments are inevitable that are proportional to the neutrino mass. These dipole moments can connect neutrinos of the same flavor or of different flavors (transition moments). If neutrinos are Majorana particles, their (diagonal) dipole moments must vanish, whereas they still have transition moments. A Dirac neutrino mass eigenstate has a magnetic dipole moment

$$(11) \quad \frac{\mu}{\mu_B} = \frac{6\sqrt{2} G_F m_e}{(4\pi)^2} m_\nu = 3.20 \times 10^{-19} \frac{m_\nu}{\text{eV}},$$

where $\mu_B = e/2m_e$ is the Bohr magneton, the usual unit to express neutrino dipole moments. Standard transition moments are even smaller because of a ‘‘GIM cancelation’’ in the relevant loop diagram. Diagonal electric dipole moments violate the CP symmetry, whereas electric dipole transition moments exist for massive mixed neutrinos even in the standard model. Large neutrino dipole moments would signify physics beyond the standard model and are thus important to measure or constrain.

Neutrino dipole moments would have a number of phenomenological consequences. In a magnetic field, these particles spin precess, turning left-handed states into right-handed ones and vice versa. Since neutrino flavor mixing is now established, it is clear that such processes would also couple neutrinos of different flavor, leading to spin-flavor

oscillations [22, 23, 24]. Stars usually have magnetic fields that can be very large and would induce spin and spin-flavor oscillations. It is now clear that the solar neutrino observations are explained by ordinary flavor oscillations, not by spin-flavor oscillations. Still, if one were to observe a small $\bar{\nu}_e$ flux from the Sun, which produces only ν_e in its nuclear reactions, this could be explained by spin-flavor oscillations of Majorana neutrinos [25, 26, 27]. Much larger magnetic fields exist in supernovae, leading to complicated spin and spin-flavor oscillation phenomena [28]. It would appear almost hopeless to disentangle spin-flavor oscillations in a supernova neutrino signal, except if one were to observe a strong burst of antineutrinos in the prompt de-leptonization burst [29].

A dipole moment contributes to the scattering cross section $\nu_e + e \rightarrow e + \nu$ where the final-state ν has opposite spin and may have different flavor. The photon mediating this process renders the cross section forward peaked, allowing one to disentangle it from the ordinary weak-interaction process. The difference is most pronounced for the lowest-energy neutrinos and the most restrictive limit, $\mu_\nu < 3.2 \times 10^{-11} \mu_B$ at 90% CL, arises from a reactor neutrino experiment [30]. Dipole and transition moments that do not involve ν_e are experimentally less well constrained.

Transition moments inevitably allow for the radiative decay $\nu_2 \rightarrow \nu_1 + \gamma$ between two mass eigenstates $m_2 > m_1$. In terms of the transition moment μ_ν the decay rate is

$$(12) \quad \Gamma_{\nu_2 \rightarrow \nu_1 \gamma} = \frac{\mu_\nu^2}{8\pi} \left(\frac{m_2^2 - m_1^2}{m_2} \right)^3 = 5.308 \text{ s}^{-1} \left(\frac{\mu_\nu}{\mu_B} \right)^2 \left(\frac{m_\nu}{\text{eV}} \right)^3,$$

where the numerical expression assumes $m_\nu = m_2 \gg m_1$. Mass dependent μ_ν constraints from the absence of cosmic excess photons are shown in fig. 7. They become very weak for small μ_ν due to the m_ν^3 phase-space factor in the expression for $\Gamma_{\nu_2 \rightarrow \nu_1 \gamma}$.

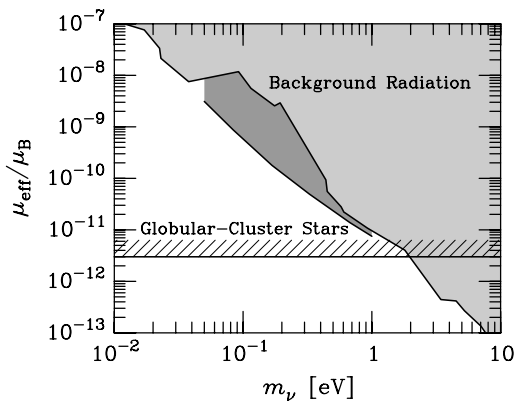


Fig. 7. – Exclusion range for neutrino transition moments [31]. The light-shaded region is ruled out by the contribution of radiative neutrino decays to the cosmic photon backgrounds [32], the dark-shaded region is excluded by TeV-gamma ray limits for the infrared background [33]. Values above the hatched bar are excluded by plasmon decay in globular-cluster stars.

The most restrictive limit arises from the plasmon decay in low-mass stars. If μ_ν is too large, neutrino emission by $\gamma \rightarrow \nu\bar{\nu}$ would affect stars more than is allowed by the observations discussed below. The volume energy loss rates caused by a putative neutrino “milli charge” e_ν , a dipole moment μ_ν , and the effective standard coupling caused by the electrons of the medium are [34]

$$(13) \quad Q = \frac{8\zeta_3}{3\pi} T^3 \times \begin{cases} \alpha_\nu \frac{\omega_{\text{pl}}^2}{4\pi} Q_1 & \text{Millicharge} \\ \frac{\mu_\nu^2}{2} \left(\frac{\omega_{\text{pl}}^2}{4\pi}\right)^2 Q_2 & \text{Dipole Moment} \\ \frac{C_V^2 G_F^2}{\alpha} \left(\frac{\omega_{\text{pl}}^2}{4\pi}\right)^3 Q_3 & \text{Standard Model} \end{cases}$$

where $Q_{1,2,3}$ are numerical factors that are 1 in the limit of a very small plasma frequency and if we neglect the contribution of longitudinal plasmons. Relative to the standard-model (SM) case, the “exotic” emission rates are

$$(14) \quad \frac{Q_{\text{charge}}}{Q_{\text{SM}}} = \frac{\alpha_\nu \alpha (4\pi)^2}{C_V^2 G_F^2 \omega_{\text{pl}}^4} \frac{Q_1}{Q_3} = 0.664 e_{14}^2 \left(\frac{10 \text{ keV}}{\omega_{\text{pl}}}\right)^4 \frac{Q_1}{Q_3},$$

$$(15) \quad \frac{Q_{\text{dipole}}}{Q_{\text{SM}}} = \frac{\mu_\nu^2 \alpha 2\pi}{C_V^2 G_F^2 \omega_{\text{pl}}^2} \frac{Q_2}{Q_3} = 0.318 \mu_{12}^2 \left(\frac{10 \text{ keV}}{\omega_{\text{pl}}}\right)^2 \frac{Q_2}{Q_3}.$$

From these ratios we directly see when the exotic contribution would roughly dominate. The observations described below finally provide the limits

$$(16) \quad e_\nu \lesssim 2 \times 10^{-14} e \quad \text{and} \quad \mu_\nu \lesssim 3 \times 10^{-12} \mu_{\text{B}}.$$

This is the most restrictive limit on diagonal dipole moments. From fig. 7 we conclude that for $m_\nu \lesssim 2 \text{ eV}$ this is also the most restrictive limit on transition moments.

2.4. Globular clusters testing stellar evolution and particle physics. – The theory of stellar evolution can be quantitatively tested by using the stars in globular clusters. Our own Milky Way galaxy has at least 157 of these gravitationally bound “balls” of stars that surround the galaxy in a spherical halo [35]. Each cluster consists of up to a million stars. Once a globular cluster has formed, new star formation is quenched because the first supernovae sweep out the gas from which new stars might otherwise form. Therefore, as a first approximation we may assume that all stars in a globular cluster have the same age and chemical composition and differ only in their mass. Since stellar evolution proceeds faster for higher-mass stars, in a globular cluster today we see a snapshot of stars in different evolutionary stages. Moreover, since the advanced stages after hydrogen burning are fast, for those stages we essentially see a star of a certain initial mass simultaneously in all advanced stages of evolution.

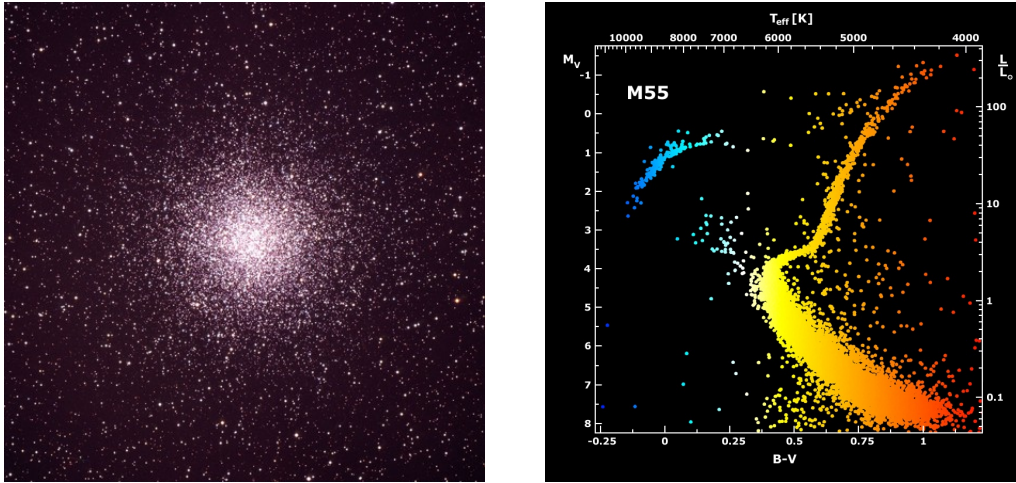


Fig. 8. – Globular cluster M55 (NGC 6809) in the constellation Sagittarius, as imaged by the ESO 3.6 m telescope on La Silla (Credit: ESO). Right panel: Color magnitude diagram of M55 (Credit: B. J. Mochejska and J. Kaluzny, CAMK, see also Astronomy Picture of the Day, <http://apod.nasa.gov/apod/ap010223.html>).

As an example we show the large globular cluster M55 in fig. 8. The theoretically relevant information is revealed when the stars are arranged in a color-magnitude diagram where the stellar brightness is plotted on the vertical axis, the color (essentially surface temperature) on the horizontal axis. (The brightness is a logarithmic measure of luminosity.) The different loci in the color-magnitude diagram correspond to different evolutionary phases as indicated in fig. 9.

- **Main Sequence (MS).** Hydrogen burning stars like our Sun, the lower-mass ones being dimmer and redder. The MS turnoff corresponds to a mass of around $0.8 M_{\odot}$, whereas more massive stars have completed hydrogen burning and are no longer on the MS.
- **Red Giant Branch (RGB).** After hydrogen is exhausted in the center, the star develops a degenerate helium core with hydrogen burning in a shell. Along the RGB, brighter stars correspond to a larger core mass, smaller core radius, and larger gravitational potential, which in turn causes hydrogen to burn at a larger T so that these stars become brighter as the core becomes more massive. The RGB terminates at its tip, corresponding to helium ignition in the core.
- **Horizontal Branch (HB).** Helium ignition expands the core which develops a self-regulating non-degenerate structure. The gravitational potential decreases, hydrogen burns less strongly, and the star dims, even though helium has been ignited. The structure of the envelope depends strongly on mass and other properties, so these stars spread out in T_{surface} at an almost fixed brightness. The blue HB down-

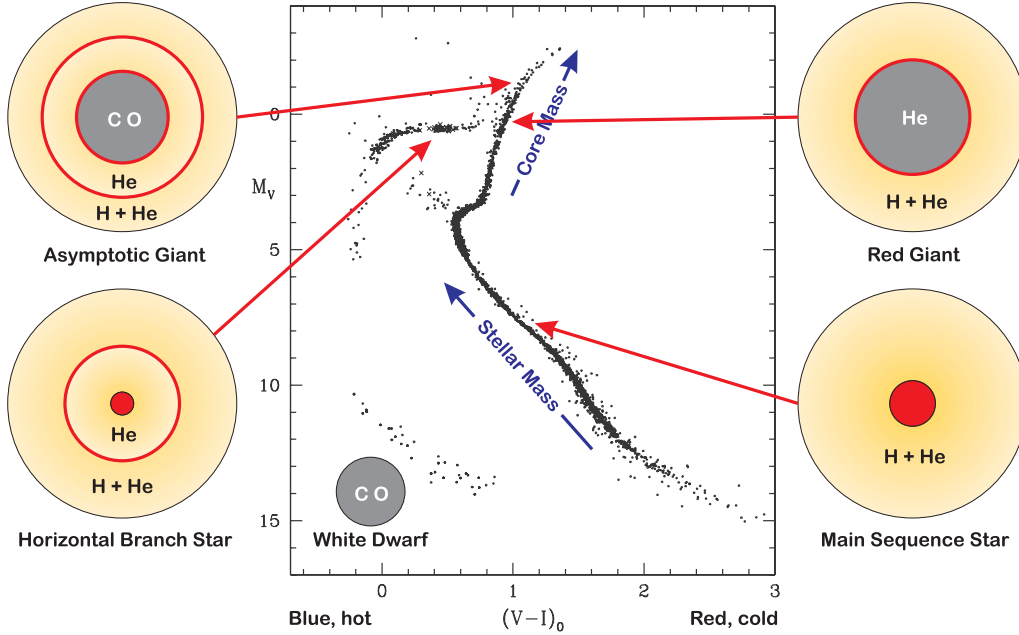


Fig. 9. – Schematic color-magnitude diagram for a globular cluster produced from selected stars of several galactic globular clusters [36]. The structure of stars corresponding to the different branches of the diagram are indicated.

turn is an artifact of the visual filter—if measured in total (bolometric) brightness, the HB is truly horizontal. For a certain T_{surface} , the envelope of these stars is not stable and they pulsate: the class of RR Lyrae stars.

- **Asymptotic Giant Branch (AGB).** After helium is exhausted, a degenerate carbon-oxygen core develops and the star now has two shell sources. As the core becomes more massive, it shrinks in size, increases its gravitational potential, and thus brightens quickly: the star ascends the red giant branch once more. Mass loss is now strong and eventually the star sheds all of its envelope to become a planetary nebula with a hot white dwarf in its center.
- **White Dwarfs.** The compact remnants are very small and thus very dim, but at first rather hot. White dwarfs then cool and become dimmer and redder. They will cross the instability strip once more, forming the class of ZZ Ceti stars.

In any of these phases, a new energy-loss channel modifies the picture. Increased neutrino losses on the RGB imply an increased core mass to ignite helium and the tip of the RGB brightens. A larger core mass at helium ignition also implies a brighter HB. Excessive particle emission on the HB implies that helium is consumed faster, the HB phase finishes more quickly for each star, implying that we see fewer HB stars. Therefore,

the number of HB stars in a globular cluster relative to other phases is a direct measure for the helium-burning lifetime. Comparing theoretical predictions with these and other observables for several globular clusters reveals excellent agreement [34, 37, 38]. The core mass at helium ignition agrees with predictions approximately to within 5–10%. This implies that the true energy loss can be at most a few times larger than the standard neutrino losses. The helium burning lifetime agrees to within 10–20%.

The helium core before ignition, essentially a helium white dwarf, has a central density of around 10^6 g cm^{-3} , an average density of around $2 \times 10^5 \text{ g cm}^{-3}$, and an almost constant temperature of 10^8 K . The average standard neutrino losses, mainly from the plasma process, are about $4 \text{ erg g}^{-1} \text{ s}^{-1}$. To avoid the helium core growing too massive, the core-averaged emission rate of any novel process should fulfill

$$(17) \quad \epsilon_x \lesssim 10 \text{ erg g}^{-1} \text{ s}^{-1}.$$

Coincidentally the same constraint applies to the energy losses from the helium burning core during the HB phase, but now to be calculated at a typical average density of about $0.6 \times 10^4 \text{ g cm}^{-3}$ and $T \sim 10^8 \text{ K}$, detailed average values given in Ref. [34].

This argument has been applied to many cases of novel particle emission, ranging from neutrino magnetic dipole moments and milli charges to new scalar or pseudoscalar particles [34, 39, 40]. The limits on neutrino electromagnetic properties were already stated in eq. (16). In addition we mention explicitly the case of axions [41, 42, 43, 44], new very low-mass pseudoscalars that are closely related to neutral pions and could be the dark matter of the universe. Axions have a two-photon interaction of the form

$$(18) \quad \mathcal{L}_{a\gamma} = -\frac{g_{a\gamma}}{4} F_{\mu\nu} \tilde{F}^{\mu\nu} a = g_{a\gamma} \mathbf{E} \cdot \mathbf{B} a, \quad \text{where} \quad g_{a\gamma} = \frac{\alpha}{2\pi f_a} \left(\frac{E}{N} - \frac{2(4+z)}{3(1+z)} \right).$$

Here, F is the electromagnetic field-strength tensor, \tilde{F} its dual, a the axion field, $z = m_u/m_d \sim 0.5$ the up/down quark mass ratio, and E/N a model-dependent ratio of small integers reflecting the ratio of electromagnetic to color anomaly of the axion current. The energy scale f_a is the axion decay constant, related to the Peccei-Quinn scale of spontaneous breaking of a new $U(1)_{\text{PQ}}$ symmetry of which the axion is the Nambu-Goldstone boson. By mixing with the π^0 - η - η' mesons, axions acquire a small mass

$$(19) \quad m_a = \frac{\sqrt{z}}{1+z} \frac{m_\pi f_\pi}{f_a} = 6 \text{ meV} \frac{10^9 \text{ GeV}}{f_a}.$$

Finally, they would interact with fermions f , notably nucleons and possibly electrons, with a derivative axial-vector structure

$$(20) \quad \mathcal{L}_{af} = \frac{C_f}{2f_a} \bar{\psi}_f \gamma^\mu \gamma_5 \psi_f \partial_\mu a \quad \text{and} \quad g_{af} = \frac{C_f m_f}{f_a},$$

where C_f is a model-dependent numerical coefficient of order unity and g_{af} a dimensionless Yukawa coupling of the axion field to the fermion f .

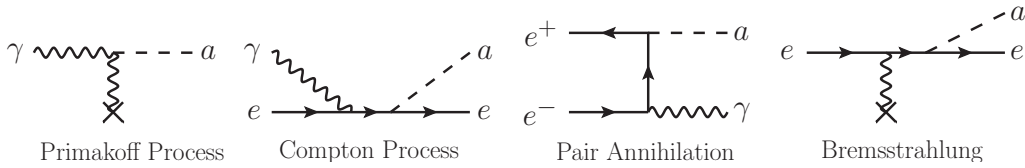


Fig. 10. – Thermal axion emission processes in normal stars.

In normal stars, these interactions allow for the axion emission processes shown in fig. 10. The Compton, pair-annihilation and bremsstrahlung processes are analogous to the corresponding neutrino processes based on the axial-current interaction. The main difference is the axion phase space compared with the two-neutrino phase space, implying a less steep temperature dependence of axion emission, so the relative importance of axion losses is greater in cooler stars. The plasmon decay does not exist for axions, but instead we have the Primakoff conversion of photons to axions in the electric fields of charged particles in the medium that is enabled by the two-photon vertex.

In globular-cluster stars, the Primakoff process is much more effective during the HB phase in the non-degenerate helium core than during the RGB phase when the helium core is degenerate. Therefore, the helium-burning lifetime will be shortened by excessive axion emission without affecting the RGB evolution. As discussed earlier, the number of HB stars in globular clusters relative to RGB stars can then be used to constrain the axion-photon interaction strength and leads to a limit [43]

$$(21) \quad g_{a\gamma} \lesssim 1 \times 10^{-10} \text{ GeV}^{-1}.$$

Similar constraints have been established by the CAST experiment searching for solar axions to be discussed later. For axion models with $E/N = 0$ this corresponds to $f_a \gtrsim 2 \times 10^7 \text{ GeV}$ or $m_a \lesssim 0.3 \text{ eV}$.

Axions are a QCD phenomenon, but in a broad class of models they also interact with electrons, the DFSZ model [45, 46] being the usual benchmark example for which $E/N = 8/3$. The limit on $g_{a\gamma}$ then translates into the weaker constraint $m_a \lesssim 0.8 \text{ eV}$. The axion-electron coupling is determined by $C_e = \frac{1}{3} \cos^2 \beta$ with $\cos \beta$ a model-dependent parameter. The dominant effect on globular cluster stars is axion emission by bremsstrahlung and the Compton process from degenerate red giant cores, delaying helium ignition. The established core mass at helium ignition then leads to the bound [47] $g_{ae} \lesssim 3 \times 10^{-13}$, translating to $m_a \lesssim 9 \text{ meV} / \cos^2 \beta$ and $g_{a\gamma} \lesssim 1.2 \times 10^{12} \text{ GeV} / \cos^2 \beta$.

2'5. White dwarf cooling. – More restrictive limits on the axion-electron interaction arise from white-dwarf (WD) cooling. When a WD has formed after an asymptotic red giant has shed its envelope, forming a planetary nebula, the compact remnant is a carbon-oxygen WD. It is supported by degeneracy pressure and simply cools and dims without igniting carbon burning. Assuming WDs are born at a constant rate in the galactic disk, the number of observed WDs per brightness interval, the “luminosity function”

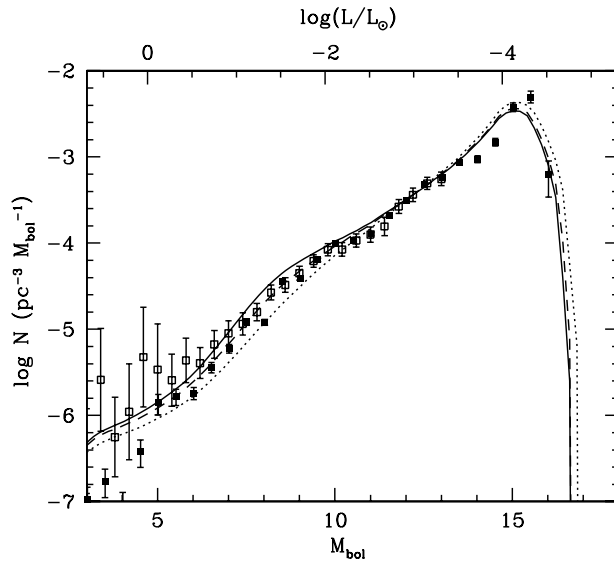


Fig. 11. – White dwarf luminosity function [49]. Open and filled squares correspond to different methods for identifying white dwarfs. Solid line: Theoretical luminosity function for a constant formation rate and 11 Gyr for the age of the galactic disk. Dashed and dotted lines: Including axion cooling corresponding to $m_a \cos^2 \beta = 5$ meV and 10 meV.

(fig. 11), then represents the cooling speed of an average WD. Any new energy-loss channel accelerates the cooling speed and, more importantly, deforms the luminosity function. A new energy-loss channel mostly affects hot WDs, whereas late-time cooling is dominated by surface photon emission.

An early application of this argument provided a limit on the axion-electron coupling of $g_{ae} \lesssim 4 \times 10^{-13}$ [48], comparable to the globular cluster limit. Revisiting WD cooling with modern data and cooling simulations [49, 50] reveals that the standard theory does not provide a perfect fit (solid line in fig. 11). On the other hand, including a small amount of axion cooling considerably improves the agreement between observations and cooling theory (dashed line in fig. 11). If interpreted in terms of axion cooling, a value $g_{ae} = 0.6\text{--}1.7 \times 10^{-13}$ is implied, not in conflict with any other limit.

In the early 1990s it became possible to test the cooling speed of pulsating WDs, the class of ZZ Ceti stars, by their measured period decrease \dot{P}/P . In particular, the star G117-B15A was cooling too fast, an effect that could be attributed to axion losses if $g_{ae} \sim 2 \times 10^{-13}$ [51]. Over the past twenty years, observations and theory have improved and the G117-B15A cooling speed still favors a new energy-loss channel [52, 53].

It is perhaps premature to be certain that these observations truly require a new WD energy-loss channel. Moreover, the interpretation in terms of axion emission is, of course, speculative. Still, these findings suggest that one should investigate other consequences of the “meV frontier” of axion physics, for example for supernovae [54].

3. – Neutrinos from the Sun

3'1. Solar neutrino measurements and flavor oscillations. – The Sun produces energy by fusing hydrogen to helium, primarily by the pp chains (table I) and a few percent through the CNO cycle (table II), emitting ν_e fluxes by the tabulated processes. In addition, a low-energy flux of keV-range thermal neutrinos emerges [57] which is negligible for energy loss. The predicted flux spectrum is shown in fig. 12. The largest flux consists of the low-energy pp neutrinos, whereas the ${}^8\text{B}$ flux with the largest energies is much smaller. The predicted fluxes (table VI) depend somewhat on the assumed solar abundance of CNO elements which is not entirely settled (section 3'2), but this uncertainty is not crucial for our present discussion.

The first solar neutrino experiment was proposed by Ray Davis in 1964 [59], accompanied by the first solar flux predictions by John Bahcall [60]. The detection principle, going back to an idea of Bruno Pontecorvo in 1946, is based on the radiochemical technique where a tank is filled with carbon tetrachloride, allowing for the reaction $\nu_e + {}^{37}\text{Cl} \rightarrow {}^{37}\text{Ar} + e^-$. The argon noble gas atoms can be washed out, concentrated, collected in a counter, and finally one can count them by observing their electron capture decay, emitting several Auger electrons. Davis used such a detector to establish in 1955 an upper limit on the ν_e flux from a reactor [61], which of course emits primarily $\bar{\nu}_e$. Around the same time, Reines and Cowan observed the first $\bar{\nu}_e$ events in their detector and in this way were the first to observe neutrinos. Davis then turned to measuring solar neutrinos with a much bigger tank, holding 615 tons of tetrachlorethylene, C_2Cl_4 , that was located deep underground in the Homestake gold mine in South Dakota. First solar neutrino results were published in 1968 [62]. After some improvements, the finally used data were taken during a quarter century 1970–1994 [6], producing in 108 extractions

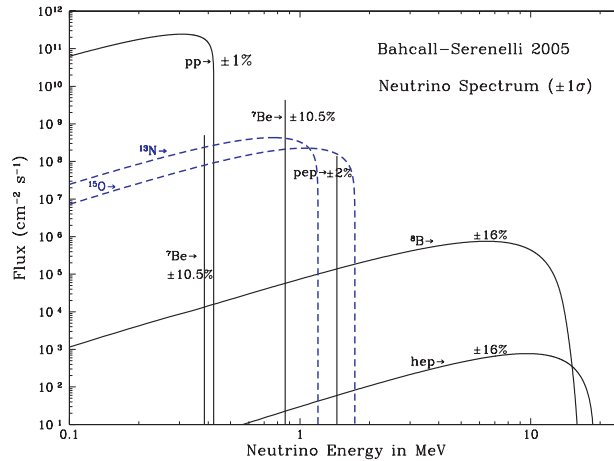


Fig. 12. – Predicted solar neutrino spectrum [55] according to the solar model of Bahcall and Serenelli (2005) [56], based on traditional opacities.

TABLE VI. – *Solar neutrino fluxes predicted with the GS98 and AGSS09 opacities compared with experimentally inferred fluxes, assuming neutrino flavor oscillations [58].*

Source	Old opacities (GS98)		New opacities (AGSS09)		Best measurements	
	Flux $\text{cm}^{-2} \text{s}^{-1}$	Error %	Flux $\text{cm}^{-2} \text{s}^{-1}$	Error %	Flux $\text{cm}^{-2} \text{s}^{-1}$	Error %
pp	5.98×10^{10}	± 0.6	6.03×10^{10}	± 0.6	6.05×10^{10}	+0.3/−1.1
pep	1.44×10^8	± 1.1	1.47×10^8	± 1.2	1.46×10^8	+1/−1.4
hep	8.04×10^3	± 30	8.31×10^3	± 30	18×10^3	+40/−50
${}^7\text{Be}$	5.00×10^9	± 7	4.56×10^9	± 7	4.82×10^9	+5/−4
${}^8\text{B}$	5.58×10^6	± 14	4.59×10^6	± 14	5.00×10^6	± 3
${}^{13}\text{N}$	2.96×10^8	± 14	2.17×10^8	± 14	$< 6.7 \times 10^8$	
${}^{15}\text{O}$	2.23×10^8	± 15	1.56×10^8	± 15	$< 3.2 \times 10^8$	

a total of around 800 registered argon atoms. This heroic effort was awarded with the physics nobel prize of 2002, shared between Ray Davis and Masatoshi Koshiba who built the first water Cherenkov detector (Kamiokande) to see solar neutrinos.

For a given exposure, only a handful of argon atoms is produced so that the measurements show huge statistical fluctuations. Still, it quickly became clear that there was a deficit of measured ν_e relative to predictions. The detection threshold of 0.814 MeV means that one picks up primarily the rather uncertain ${}^8\text{B}$ flux, so for a long time the “solar neutrino problem” was widely attributed to solar model, nuclear cross section, and experimental uncertainties. However, already in 1969 Gribov and Pontecorvo proposed neutrino flavor oscillations $\nu_e \rightarrow \nu_\mu$ as a possible interpretation [63]. It is assumed that the flavor and mass eigenstates are related by a rotation with mixing angle θ

$$(22) \quad \begin{pmatrix} \nu_e \\ \nu_\mu \end{pmatrix} = \begin{pmatrix} \cos \theta & \sin \theta \\ -\sin \theta & \cos \theta \end{pmatrix} \begin{pmatrix} \nu_1 \\ \nu_2 \end{pmatrix}.$$

At ν_e production, actually a coherent superposition of the mass eigenstates ν_1 and ν_2 emerges which propagate with different momenta $p_{1,2} = (E^2 - m_{1,2}^2)^{1/2} \approx E - m_{1,2}^2/2E$, so that after some distance L their interference provides for a nonvanishing ν_μ amplitude. It is easy to work out that the ν_μ appearance probability is (fig. 13)

$$(23) \quad P_{\nu_e \rightarrow \nu_\mu} = \sin^2(2\theta) \sin^2\left(\frac{\Delta m^2}{4E} L\right) \quad \text{and} \quad L_{\text{osc}} = \frac{4\pi E}{\Delta m^2} = 2.5 \text{ m} \frac{E}{\text{MeV}} \frac{\text{eV}^2}{\Delta m^2},$$

where $\Delta m^2 = m_2^2 - m_1^2$ and L_{osc} is the oscillation length.

One reason for being skeptical about the flavor oscillation hypothesis was the required large mixing angle to achieve a large ν_e deficit, in contrast to the known small mixing angles among quarks. This perception changed when the impact of matter on flavor oscillations was recognized. Wolfenstein (1978) showed that neutrino refraction in matter

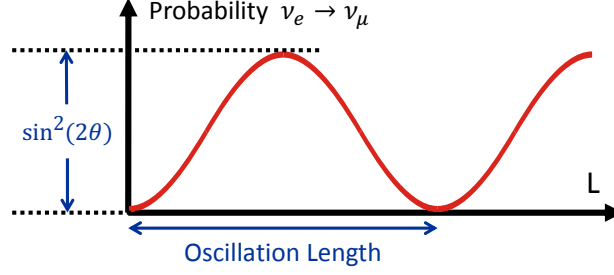


Fig. 13. – Flavor oscillations.

strongly influences flavor oscillations if neutrino mass differences are indeed small [64]. Neutrinos in normal unpolarized matter feel an effective weak potential

$$(24) \quad V_{\text{weak}} = \pm \sqrt{2} G_{\text{F}} \times \begin{cases} n_e - \frac{1}{2} n_n & \text{for } \nu_e, \\ -\frac{1}{2} n_n & \text{for } \nu_{\mu, \tau}, \end{cases}$$

where n_e and n_n are the electron and neutron densities. The potential depends on flavor because ν_e has an additional contribution to its effective neutral-current interaction with e from W exchange (fig. 4). The positive sign applies to neutrinos, the negative sign to antineutrinos. In the Earth, taking a typical density of 5 g cm^{-3} , the ν_e - ν_μ weak potential difference is $\Delta V_{\text{weak}} = \sqrt{2} G_{\text{F}} n_e \sim 2 \times 10^{-13} \text{ eV} = 0.2 \text{ peV}$. The flavor variation along the propagation direction z is now governed by the Schrödinger-like equation

$$(25) \quad i \frac{\partial}{\partial z} \begin{pmatrix} \nu_e \\ \nu_\mu \end{pmatrix} = \mathbf{H} \begin{pmatrix} \nu_e \\ \nu_\mu \end{pmatrix}$$

where the Hamiltonian 2×2 matrix is

$$(26) \quad \mathbf{H} = \frac{\Delta m^2}{4E} \begin{pmatrix} -\cos 2\theta & \sin 2\theta \\ \sin 2\theta & \cos 2\theta \end{pmatrix} \pm \sqrt{2} G_{\text{F}} \begin{pmatrix} n_e - n_n/2 & 0 \\ 0 & -n_n/2 \end{pmatrix}$$

The first term is the neutrino mass-squared matrix in the weak-interaction basis. In the matter term, the neutron contribution is the same for both flavors. It only provides an overall common phase and thus is usually removed.

The matter contribution has the effect that the eigenstates of \mathbf{H} , the propagation eigenstates, are not identical with the vacuum mass eigenstates. In particular, when the density is large, propagation and flavor eigenstates become more and more similar and neutrinos are essentially “un-mixed.” A completely new effect arises when neutrinos propagate through a density gradient as in the Sun. What happens is best explained if one plots the energy eigenvalues of \mathbf{H} in eq. (26) as a function of density (fig. 14). The sign of the matter term changes for antineutrinos, so we can extend the plot to “negative densities” to include neutrinos and antineutrinos in the same plot. Neutrinos propagating

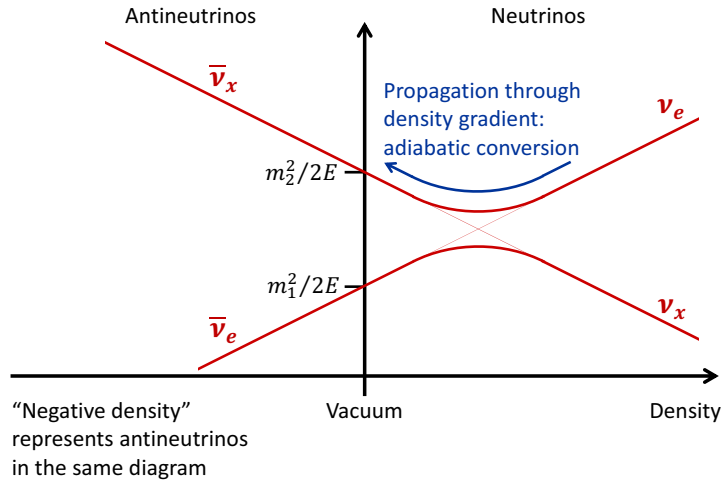


Fig. 14. – Eigenvalue diagram of the 2×2 Hamiltonian matrix for 2-flavor oscillations in matter.

through a density gradient amount to solving the Schrödinger equation with a slowly changing Hamiltonian. If a system is prepared in an eigenstate of the Hamiltonian and if the latter changes adiabatically, then the system will always stay in an eigenstate that slowly changes. So if the neutrino is born as ν_e at high density, it is essentially in a propagation eigenstate. As the density slowly decreases on the neutrino’s way out of the Sun, it always stays in a propagation eigenstate and thus emerges at the surface (vacuum) as the mass eigenstate ν_2 connected to ν_e in the level diagram (fig. 14). If it were prepared as a $\bar{\nu}_e$ at high density (far to the left on the plot), it would emerge as a ν_1 eigenstate. The crucial point is that the eigenvalues are unique and do not cross as a function of density—they “repel” and “avoid each other.” If the mixing angle is small and ν_e is essentially the lower mass eigenstate ν_1 , it still emerges as ν_2 and thus essentially as ν_μ , i.e. we obtain a large flavor conversion effect even though the mixing angle is small. This is the celebrated Mikheev-Smirnov-Wolfstein (MSW) effect that was discovered in 1985 by Stanislav Mikheev and Alexei Smirnov [65]. The interpretation in terms of an “avoided level crossing” as in fig. 14 was given in the same year by Hans Bethe [66]. These results completely changed the particle physicists’ attitude toward the solar neutrino problem in that a beautiful mechanism had been found where a small mixing angle could cause large flavor conversion.

After more than 20 years of data taking with the Homestake Cl detector, new experiments were coming online. The radiochemical technique was used with gallium as a target, $\nu_e + {}^{71}\text{Ga} \rightarrow {}^{71}\text{Ge} + e^-$. The low energy threshold of 233 keV allows one to pick up neutrinos from all source reactions, including the dominant pp flux. The GALLEX experiment, later Gallium Neutrino Observatory (GNO), used dissolved gallium and was located in the Gran Sasso laboratory. GALLEX/GNO took data 1991–2003 and confirmed the solar neutrino problem [67]. The Soviet American Gallium Experiment

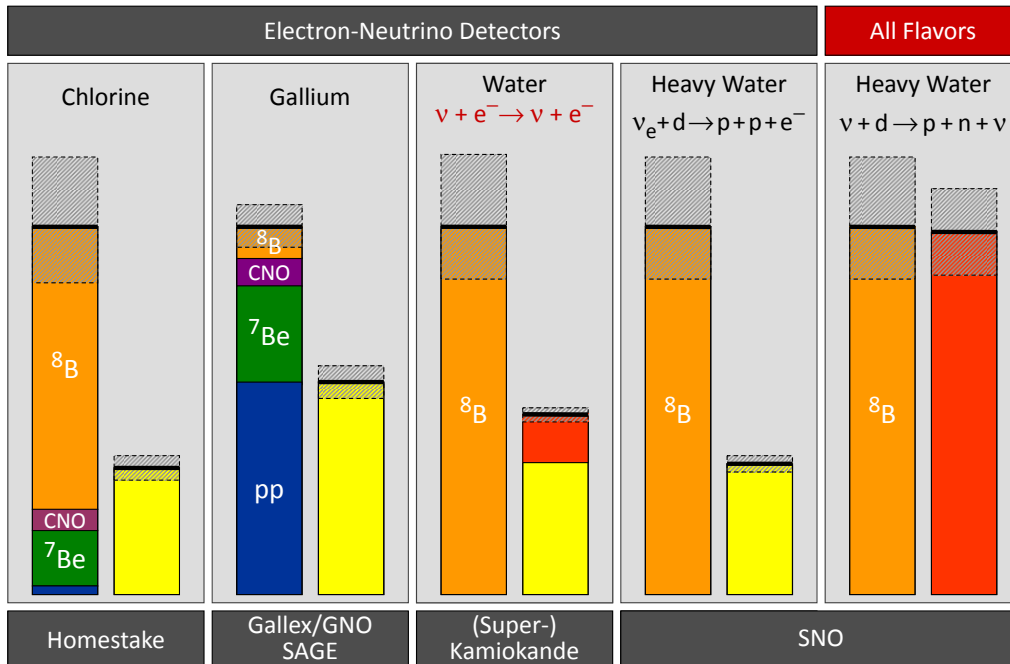


Fig. 15. – Solar neutrino predictions and measurements in different experiments circa 2002. For each experiment, the total prediction (in arbitrary units normalized to one) and its error bar are shown as well as the fractional contribution of different source reactions. Juxtaposed is the experimental measurement with its uncertainties. Yellow experimental bars are for ν_e , red bars for all flavors. (Adapted after a similar plot frequently shown by John Bahcall.)

(SAGE) uses metallic gallium. It took its first extraction in 1990 and is still running today, with 1990–2007 data published [68]. The expected contribution of the different source reactions juxtaposed with the measured rate is shown in fig. 15.

The next step forward was the advent of water Cherenkov detectors, measuring electron scattering $\nu + e \rightarrow e + \nu$ where all flavors contribute, although the $\nu_e e$ cross section is much larger. The challenge was to lower the energy threshold enough to pick up solar ^8B neutrinos. This feat was first achieved with the Japanese Kamiokande detector, originally built in 1982–1983 to search for proton decay. It was ready for solar neutrino detection in January 1987, consisting of 2140 tons of pure water viewed by 948 photomultipliers, providing 20% photosensitive area. Almost immediately, on 23 February 1987, it saw the neutrino burst from Supernova 1987A. Solar neutrino data were taken January 1987–February 1995 and yielded an ^8B neutrino flux of $2.80 \pm 0.19(\text{stat}) \pm 0.33(\text{syst}) \times 10^6 \text{ cm}^{-2} \text{ s}^{-1}$, about 49–64% of standard solar model predictions, if a pure ν_e flux is assumed.

The era of high-statistics solar neutrino measurements began when the 50 kton water Cherenkov detector Super-Kamiokande (fig. 16) took up operation on 1 April 1996 and

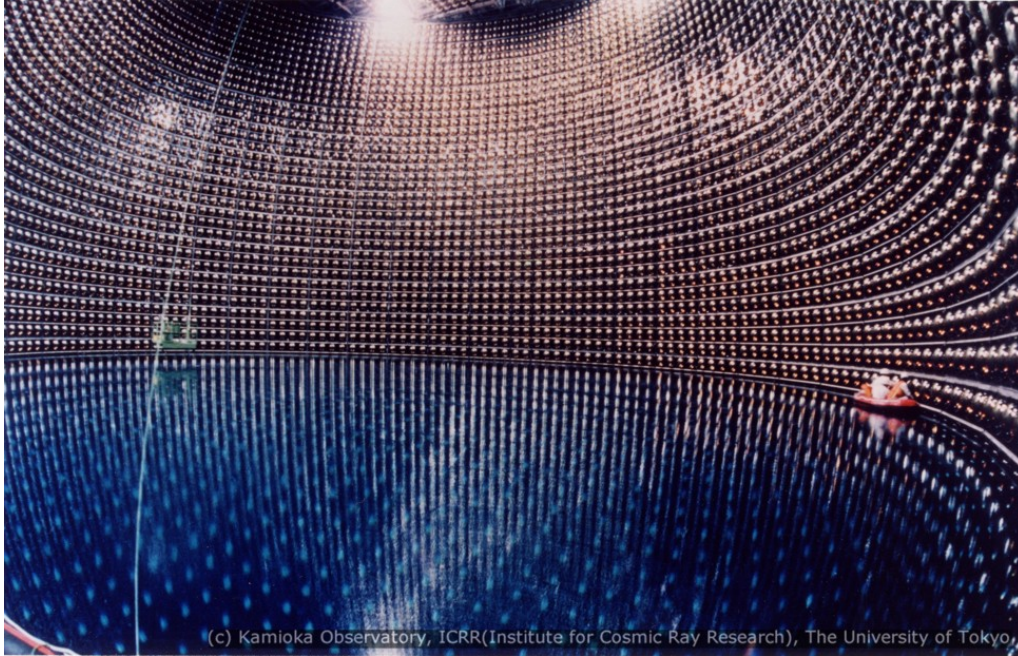


Fig. 16. – Super-Kamiokande water Cherenkov detector being filled in January 1996 (Copyright: Kamioka Observatory, ICRR, The University of Tokyo).

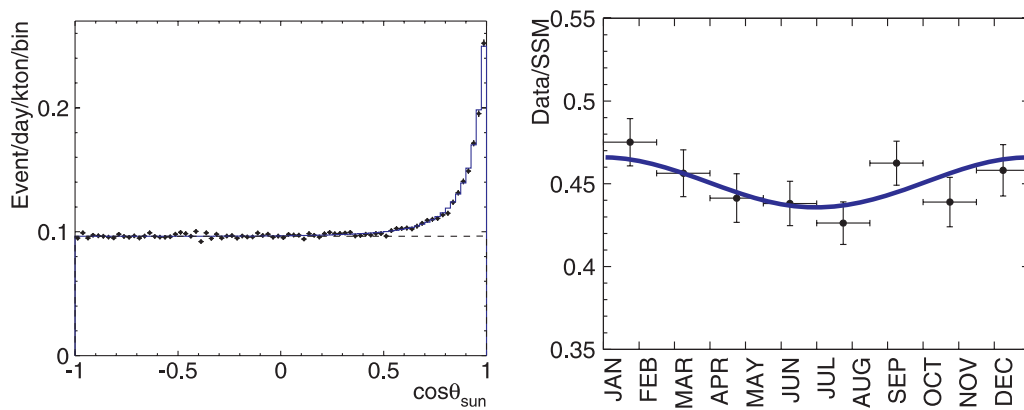


Fig. 17. – Solar neutrino measurements with 1258 days of Super-Kamiokande [69]. Left: Positron direction relative to Sun, including a uniform background on the level of 0.1. Right: Seasonal variation of the total flux.

has taken data since with some interruptions for repairs and upgrades. Super-K registers about 15 solar neutrinos per day, i.e. about as many in two months as Homestake did in a quarter century. The latest published results are those of Super-K phase III that ended in August 2008 [70], when the electronics was replaced, giving way to Super-K IV as the currently operating detector. The ^8B flux, under the assumption of pure ν_e , was measured by Super-K III to be $2.32 \pm 0.04(\text{stat}) \pm 0.05(\text{syst}) \times 10^6 \text{ cm}^{-2} \text{ s}^{-1}$.

With such high statistics one can perform true neutrino astronomy. The electron recoil events crudely maintain the neutrino direction and therefore statistically point back to the Sun (fig. 17, left panel). Likewise, the annual neutrino flux variation reveals the ellipticity of the Earth orbit around the Sun (fig. 17, right panel).

Interpreting the solar neutrino observations of Homestake, GALLEX, SAGE and Super-Kamiokande in terms of two-flavor oscillations led around 1998 to the situation shown in fig. 18. There were three MSW solutions where the matter effect in the Sun is important, the small-mixing angle solution (SMA), the large mixing-angle solution (LMA) and the LOW solution. In addition there was a solution with large mixing angle and pure vacuum oscillations (VAC), corresponding to an oscillation length of the Sun-Earth distance of 150 million km. The SMA solution, where a small mixing angle gives a large flavor conversion by the MSW mechanism, was still favored by many.

Then the situation changed quickly with Super-K in 1998 producing first unambiguous evidence for atmospheric $\nu_\mu \rightarrow \nu_\tau$ oscillations with a near-maximal mixing angle [72], showing neutrino flavor oscillations with a large mixing angle. Moreover, when Super-K began including high-statistics spectral and zenith-angle information for solar neutrinos, the SMA and VAC solutions became less and less of a good fit [73].

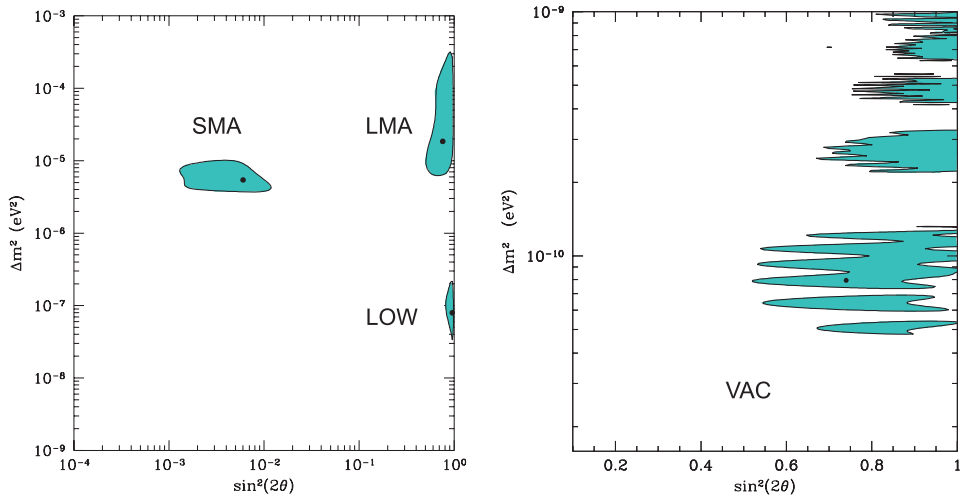


Fig. 18. – Best-fit regions circa 1998 in a two-flavor oscillation interpretation of the measured rates of Homestake, GALLEX, SAGE and Super-Kamiokande together with the predictions of the Bahcall and Pinsonneault (1998) standard solar model. (Adapted from Ref. [71].)



Fig. 19. – Sudbury neutrino observatory (SNO), Cherenkov detector with 1000 tons of heavy water. Left: Artists rendition of detector. Right: Fish-eye picture. (Photos courtesy of SNO.)

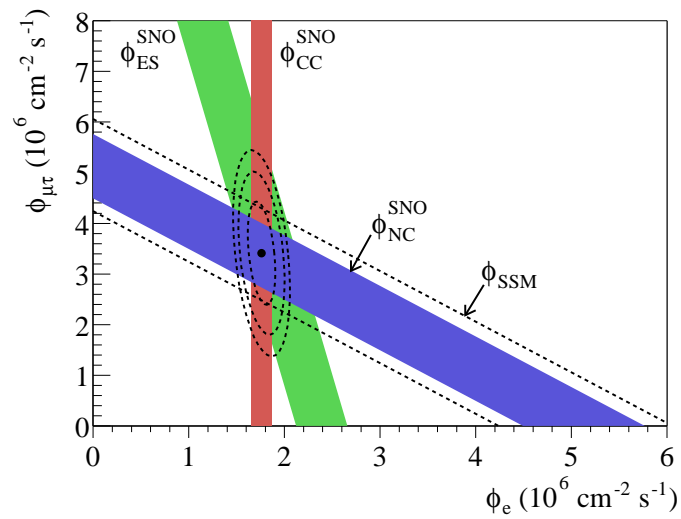


Fig. 20. – SNO solar neutrino measurements (2002) for charged current (CC) and neutral current (NC) deuterium disintegration and electron scattering (ES) [74].

The solar oscillation story was finally wrapped up by two new experiments. One was the Sudbury Neutrino Observatory (SNO) in Canada, a water Cherenkov detector that used 1000 t of heavy water, D_2O , as a target, taking data 1999–2006 (fig. 19). It uses electron scattering (ES) that is sensitive primarily to ν_e and also the other flavors. It further uses a pure ν_e channel by charged-current (CC) deuteron disintegration, $\nu_e + d \rightarrow p + p + e^-$, and an all-flavor channel by neutral-current (NC) disintegration, $\nu + d \rightarrow p + n + \nu$. When first results from all three channels became available in 2002, the iconic picture of fig. 20 revealed a consistent solution where the all-flavor 8B flux was as predicted by solar models and the ν_e deficit was clearly explained by flavor conversion [74].

After Super-K had been built, the old Kamiokande water Cherenkov detector was replaced with KamLAND, a scintillator detector, with correspondingly lower energy threshold that could measure the neutrino flux from the Japanese nuclear power reactors, the dominant distance being around 180 km. In this way the solar LMA solution could be tested with a laboratory experiment, of course against theoretical advice, favoring the SMA solution. The year 2002 became the *annus mirabilis* of neutrino physics in that KamLAND indeed found ν_e disappearance corresponding to the solar LMA solution [75]. With more statistics, KamLAND later produced the beautiful L/E plot of fig. 21. The flavor oscillation probability of eq. (23) varies with L/E so that one can see an oscillation pattern when plotting the measurements as a function of this variable. This is probably the most convincing evidence for the reality of flavor oscillations.

Combining all solar neutrino measurements and the KamLAND reactor results in a two-flavor oscillation interpretation yields the best-fit parameters shown in fig. 22. It is essentially KamLAND that fixes Δm^2 with high precision, whereas the solar measure-

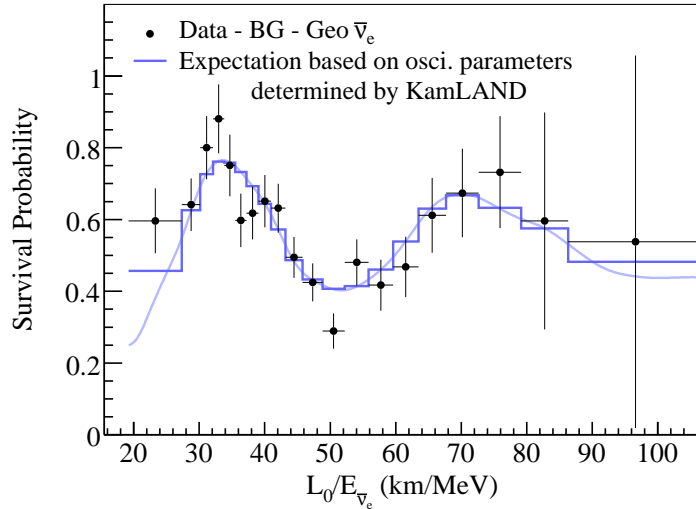


Fig. 21. – Energy variation in terms of L/E of the KamLAND reactor neutrino measurements [76], clearly showing flavor oscillations.

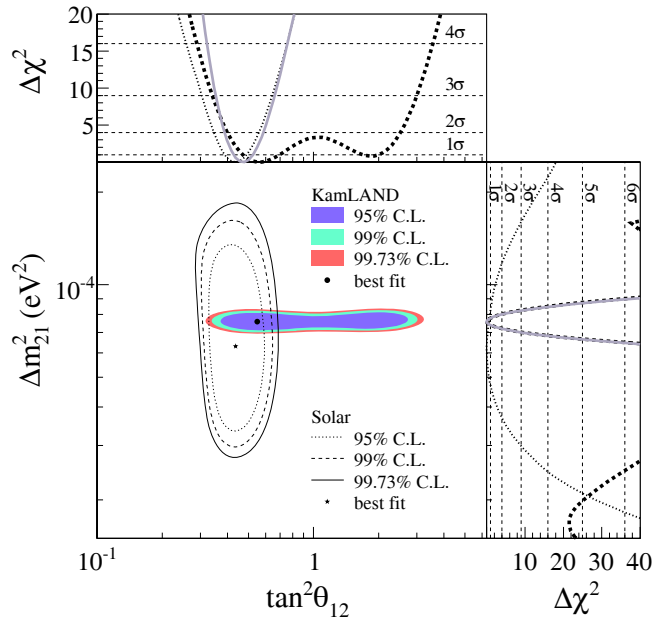


Fig. 22. – Allowed region for neutrino oscillation parameters from KamLAND and solar neutrino experiments [76]. The side-panels show the χ^2 -profiles for KamLAND (dashed) and solar experiments (dotted) individually, as well as the combination of the two (solid).

ments fix the mixing angle. The values above and below 45° are not symmetric because of the matter effect in the Sun. In other words, the solar matter effect fixes the mass ordering to be $m_1 < m_2$ and the mixing angle is large but not maximal.

While the solar neutrino problem has been settled since 2002, this is not the end of solar neutrino measurements. The task now is precision and detailed tests. One new contribution in solar neutrino spectroscopy comes from the Borexino experiment in the Gran Sasso laboratory. It is an ultrapure scintillator detector (278 tons) and measures solar neutrinos by electron scattering. It is particularly sensitive to the monochromatic ${}^7\text{Be}$ neutrinos (0.863 MeV) and pep neutrinos (1.445 MeV) because they produce a distinct shoulder in the electron recoil spectrum. After many delays, data taking began in August 2007 and the detector worked beautifully. The most recent result provides the ν_e equivalent ${}^7\text{Be}$ flux of $(3.10 \pm 0.15) \times 10^9 \text{ cm}^{-2} \text{ s}^{-1}$ and under the assumption of flavor oscillations a ν_e survival probability of 0.51 ± 0.07 at 862 keV [77]. Most recently, a measurement of the much smaller pep flux was also reported [78].

The ν_e survival probability P_{ee} in the Sun at $E \lesssim 1$ MeV is essentially given by vacuum oscillations because $\Delta m^2/2E$ is too large to be much affected by solar matter, so $P_{ee} \sim 1 - \frac{1}{2} \sin^2 2\theta$ (fig. 23). On the other hand, for $E \gtrsim 6$ MeV it is given by the MSW value $P_{ee} \sim \sin^2 \theta$. The energy-dependent solar measurements confirm this picture. Borexino has made this crucial test much more precise (fig. 23).

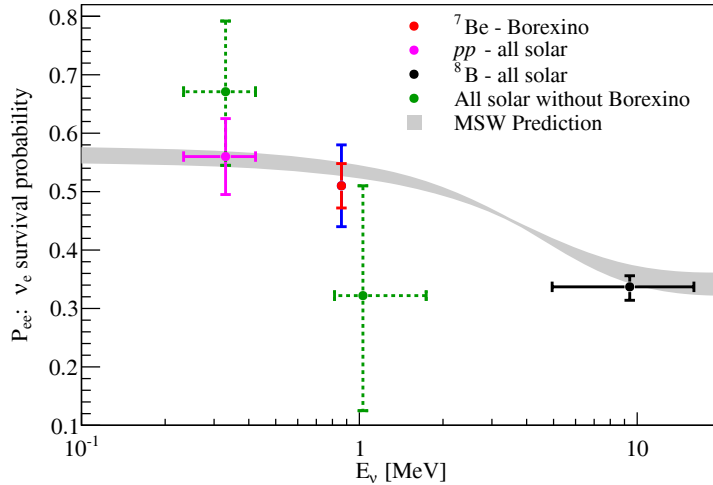


Fig. 23. – Energy-dependent survival probability P_{ee} for solar ν_e [77]. The grey band indicates the standard solar model (SSM) expectation together with the best-fit LMA solution. For the ${}^7\text{Be}$ point, measured by Borexino, the inner (red) error bars show the experimental uncertainty, while the outer (blue) error bars show the total (experimental + SSM) uncertainty. The remaining points were obtained from a combined analysis of the results of all solar neutrino experiments. The green (dashed) points are calculated without Borexino data.

Solar neutrino oscillations are usually analyzed in a two-flavor context, but of course we have three active flavors that are superpositions of three mass eigenstates,

$$(27) \quad \begin{pmatrix} \nu_e \\ \nu_\mu \\ \nu_\tau \end{pmatrix} = \mathbf{U} \begin{pmatrix} \nu_1 \\ \nu_2 \\ \nu_3 \end{pmatrix},$$

where the unitary transformation can be parameterized in the form

$$(28) \quad \mathbf{U} = \begin{pmatrix} 1 & 0 & 0 \\ 0 & c_{23} & s_{23} \\ 0 & -s_{23} & c_{23} \end{pmatrix} \begin{pmatrix} c_{13} & 0 & e^{-i\delta}s_{13} \\ 0 & 1 & 0 \\ -e^{i\delta}s_{13} & 0 & c_{13} \end{pmatrix} \begin{pmatrix} c_{12} & s_{12} & 0 \\ -s_{12} & c_{12} & 0 \\ 0 & 0 & 1 \end{pmatrix},$$

where $c_{12} = \cos\theta_{12}$, $s_{12} = \sin\theta_{12}$ and so forth. Besides two mass differences $m_{21}^2 = m_2^2 - m_1^2$ and $m_{31}^2 = m_3^2 - m_1^2$, flavor oscillations depend on three mixing angles θ_{12} , θ_{23} , and θ_{13} as well as a CP-violating phase (Dirac phase) δ .

The current best-fit values for the oscillation parameters are summarized in table VII according to Fogli et al. [79] (see Gonzalez-Garcia et al. [80] for an alternative analysis). The third mixing angle θ_{13} is small so that flavor oscillations approximately factorize into the two-flavor oscillation problems of the 12 sector (“solar oscillations”) and the 23 sector (“atmospheric oscillations”). Until recently, all data were compatible with a

TABLE VII. – *Neutrino oscillation parameters from a global fit of all solar, reactor, atmospheric and long-baseline experiments [80]. The preliminary value on θ_{13} is based on T2K and first Double Chooz data [81].*

Parameter	Units	Best-fit	1σ range	3σ range
$\delta m^2 = m_2^2 - m_1^2$	meV ²	+75.8	73.2–78.0	69.9–81.8
$\Delta m^2 = m_3^2 - \frac{1}{2}(m_2^2 + m_1^2)$	meV ²	± 2350	$\pm(2260-2470)$	$\pm(2060-2670)$
$\sin^2 \theta_{12}$		0.306	0.291–0.324	0.259–0.359
$\sin^2 \theta_{23}$		0.42	0.39–0.50	0.34–0.64
$\sin^2 \theta_{13}$		$0.085 \pm 0.029(\text{stat}) \pm 0.042(\text{sys})$		
δ		$0^\circ-360^\circ$		

vanishing θ_{13} , although a global analysis provided first hints for a nonvanishing value at the 3σ level [79]. Most recently (Nov. 2011), additional evidence came from the Double Chooz reactor experiment [81]. This question will be convincingly settled within a few years with more data from the T2K long baseline experiment and the reactor experiments Double Chooz, Reno, and Daya Bay. If indeed θ_{13} is not very small, then the next step will be to measure the Dirac phase δ , causing CP violation in oscillation experiments. The other parameter that remains to be settled is the mass hierarchy, i.e. if $\Delta m^2 > 0$ (normal hierarchy) or $\Delta m^2 < 0$ (inverted hierarchy). In the 12 sector, the mass ordering $\delta m^2 > 0$ has been settled by the matter effect in the Sun.

3.2. Helioseismology and the solar opacity problem. – The inner properties of the Sun can be studied with neutrinos and helioseismology. For many years, helioseismology yielded perfect agreement with standard solar models, whereas the neutrino measurements were plagued by the mysterious ν_e deficit that was finally explained by flavor oscillations. Just as the neutrino problem got sorted out, the helioseismic agreement began to sour and today poses a new problem about the Sun.

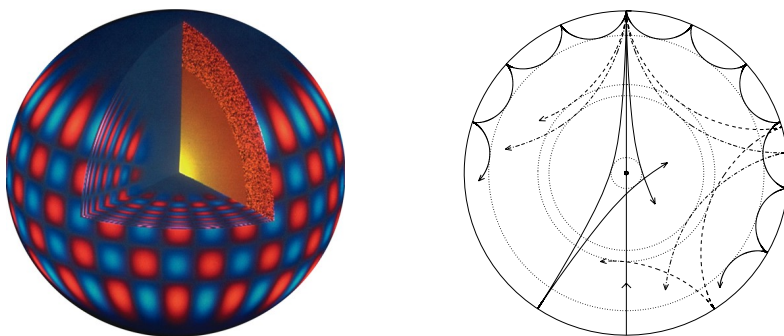


Fig. 24. – Left: One example for solar p-mode oscillations (Credit: Global Oscillation Network Group/National Solar Observatory/AURA/NSF). Right: Propagation of p-modes in the Sun [82] (Credit: J. Christensen-Dalsgaard, TAC Aarhus).

The solar structure can vibrate around its hydrostatic equilibrium configuration in different ways. Of main interest are the p-modes (pressure modes), essentially sound waves with few-minute frequencies, that get constantly excited by the convective overturns in the outer layers of the Sun. Depending on their frequency, these seismic waves probe more or less deep into the solar interior (fig. 24), allowing one to probe the solar sound-speed profile as a function of radius. One needs to measure the p-mode frequencies as a function of multipole order ℓ . To this end one measures the motion of the solar surface by the Doppler effect and can produce a “Dopplergram” as shown in fig. 25 where one can also see the global rotation of the Sun by the systematic speed variation across the solar disk. To determine the frequencies one needs a long uninterrupted time series for Fourier transformation. This is achieved either by satellite observations such as the MDI instrument on the SOHO satellite (<http://sohowww.nascom.nasa.gov>) or by networks of terrestrial telescopes that offer 24h vision of the Sun such as BiSON (<http://bison.ph.bham.ac.uk>) and GONG (<http://gong.nso.edu>). A typical power spectrum derived by this method is also shown in fig. 25. The theory of how to invert this information to derive a solar sound speed profile is described, for example, in the lecture notes of J. Christensen-Dalsgaard [82]. In this way one can derive a “seismic model” of the Sun that allows for comparison with standard solar models. Besides the sound-speed profile, one also derives the depth of the convective zone R_{CZ} and the surface helium mass fraction Y_S , an adjustable solar-model parameter that is not directly observable.

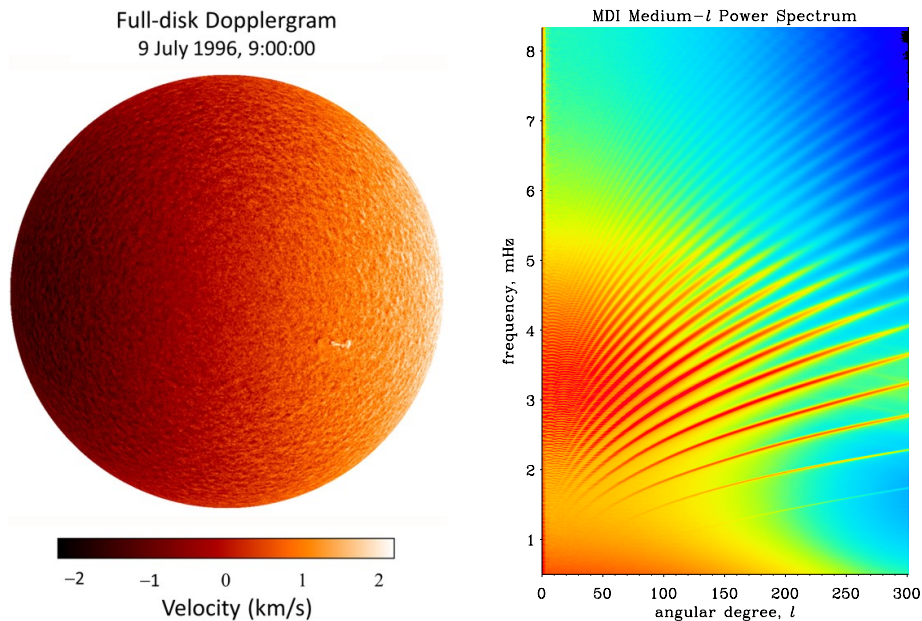


Fig. 25. – Full-disk Dopplergram of the Sun taken with the MDI instrument on the SOHO satellite (left). Power spectrum of p-modes (right). Credit: SOHO (ESA & NASA).

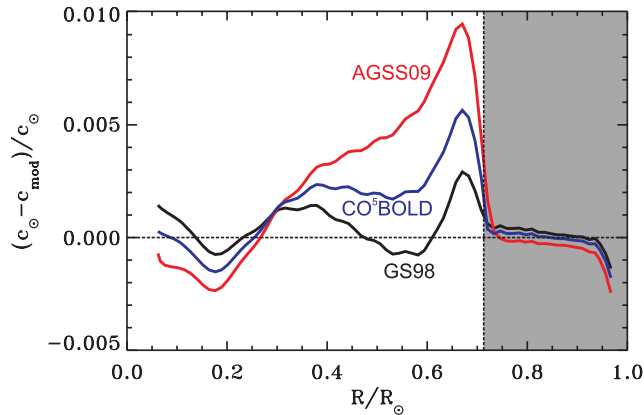


Fig. 26. – Solar soundspeed profile relative to helioseismic model for the indicated cases of opacities. The grey region is the convection zone. (Adapted from Serenelli 2011 [83].)

A traditional solar model compared with helioseismology is shown by the black line (GS98) in fig. 26. The perfect agreement, taken for a long time as evidence for our excellent understanding of the Sun, depends crucially on the solar opacities, which in turn depend on the abundances of chemical elements. Traditional models are based on the Grevesse and Sauval 1998 (GS98) opacities [84]. Since 2005, however, Martin Asplund and collaborators have provided new solar element abundances based on a 3D-hydrodynamics model atmosphere, better selection of spectral lines (identification of blends) and detailed treatment of radiative transport in the line-formation modeling. This leads to a 30–40% reduction of the CNO and Ne abundances. Solar models based on the Asplund, Grevesse, Sauval and Scott 2009 (AGSS09) opacities [85] lead to significant modifications of the sound-speed profile, depth of convection zone and surface helium abundance (fig. 26 and table VIII), in stark conflict with the seismic model. Caffau and collaborators (CO⁵BOLD) have embarked on a similar task, but arrive at different abundances [86]. The corresponding solar models are halfway between GS98 and AGSS09. Either way, the discrepancy with helioseismology remains unresolved. For example, phases of accretion during solar evolution do not seem to be successful [58].

TABLE VIII. – *Properties of solar models with different opacities [83].*

Model	Metallicity Z/X	Depth Convection Zone R_{CZ}/R_{\odot}	Surface He Abundance Y_{S}
Seismic		0.713 ± 0.001	0.2485 ± 0.0035
GS98	0.0229	0.713	0.243
CO ⁵ BOLD	0.0209	0.717	0.237
AGSS09	0.0178	0.723	0.232

The solar neutrino flux predictions are also modified as shown in table VI. However, the directly measured ${}^8\text{B}$ and ${}^7\text{Be}$ fluxes are roughly halfway between the GS98 and AGSS09 models and agree with either within uncertainties. On the other hand, the predicted CNO-cycle neutrino fluxes naturally are much smaller, but for the moment only crude experimental upper limits exist. Sufficiently precise neutrino observations of the CNO neutrino fluxes could settle the question of the element abundances in the deep solar interior, but it appears doubtful that Borexino can measure these fluxes with sufficient precision, even if it achieves to measure them.

The new question of solar element abundances has opened up a new frontier for solar neutrino astronomy. Evidently our understanding of flavor oscillations is crucial for using neutrinos as legitimate astrophysical probes. Solar neutrino measurements began to prove that nuclear reactions were the power source of stars. After the “distraction” of flavor oscillations, the field is back to its roots as a probe of the solar interior.

3.3. Sun as a particle source. – The Sun is a very well understood neutrino source and has provided invaluable information on neutrino oscillation parameters. Some of the solar ν_e fluxes, notably the pp flux, arguably are better known than the $\bar{\nu}_e$ flux from a power reactor where a possible adjustment of several percent has recently caused a lot of attention [87]. The Sun as a ν_e source can provide additional information beyond oscillation parameters. For example, a hypothetical $\nu_e \rightarrow \bar{\nu}_e$ conversion, perhaps by Majorana transition moments, has been constrained by Borexino to a probability of less than 1.3×10^{-4} (90% CL) for $E_{\bar{\nu}} > 1.8$ MeV, the most restrictive limit of this kind [88]. One can also constrain radiative neutrino decays $\nu_2 \rightarrow \nu_1 + \gamma$ by the absence of solar γ rays [89], but the small neutrino mass differences render such constraints on the effective transition moment less interesting than, for example, the globular cluster limit from plasmon decay given in eq. (16).

The Sun can also emit hypothetical low-mass particles other than neutrinos where both nuclear reactions and thermal plasma process can be the source. For example, in the reaction $d + p \rightarrow {}^3\text{He} + \gamma$ of the solar pp chains (table I) the photon can be substituted with an axion that can subsequently decay outside of the Sun, producing γ rays, an argument that has led to an early constraint on “standard axions” [90]. Today, “invisible axions” are of much greater interest with such low masses that they are easily produced in the thermal processes of fig. 10 that are based either on the axion-electron or the axion-photon coupling. In the so-called DFSZ axion model, the axion-photon interaction strength is given by $E/N = 8/3$ in eq. (18). If we assume $C_e = 1/6$, the solar axion flux prediction at Earth is shown in fig. 27, based on the white-dwarf inspired axion-electron coupling of $g_{ae} = 10^{-13}$ (section 2.5).

Solar axions can be searched with the “helioscope” technique [91]. Particles with a two-photon vertex can transform into photons and vice versa in an external electromagnetic field. For a microscopic target this is a scattering process with photon exchange, the Primakoff process shown in fig. 10. In a macroscopic field, the conversion $a \rightarrow \gamma$ is more akin to a flavor oscillations [92]. The “flavor variation” along a beam in z direction is then given, in full analogy to neutrino flavor oscillations, by the Schrödinger-like

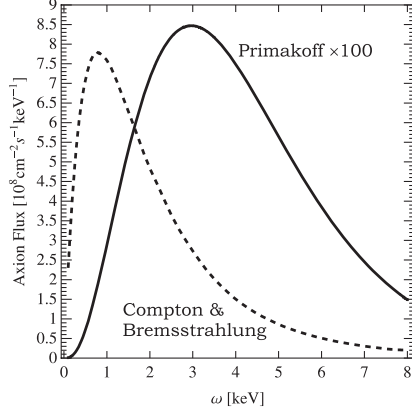


Fig. 27. – Solar axion flux at Earth from electron processes, assuming $g_{ae} = 1 \times 10^{-13}$ (dashed line) and from the Primakoff process, assuming an axion-photon coupling of $g_{a\gamma} = 10^{-12} \text{ GeV}^{-1}$, corresponding to DFSZ axions with $f_a = 0.85 \times 10^9 \text{ GeV}$, $C_e = 1/6$ and $E/N = 8/3$ [103].

equation

$$(29) \quad i \frac{\partial}{\partial z} \begin{pmatrix} \gamma \\ a \end{pmatrix} = \frac{1}{2\omega} \begin{pmatrix} \omega_{\text{pl}}^2 & g_{a\gamma} B \omega \\ g_{a\gamma} B \omega & m_a^2 \end{pmatrix} \begin{pmatrix} \gamma \\ a \end{pmatrix},$$

where ω is axion or photon energy, B is the transverse magnetic field, and we have included an effective photon mass in terms of the plasma frequency if the process does not take place in vacuum. The conversion probability after a distance L is

$$(30) \quad P_{a \rightarrow \gamma} = \left(\frac{g_{a\gamma} B L}{2} \right)^2 \frac{\sin^2(qL/2)}{(qL/2)^2},$$

where the required momentum transfer is

$$(31) \quad q = \sqrt{\left(\frac{\omega_{\text{pl}}^2 - m_a^2}{2\omega} \right)^2 + (g_{a\gamma} B)^2}.$$

To detect solar axions one would thus orient a dipole magnet toward the Sun and search for keV-range x-rays at the far end of the conversion pipe. After a pioneering effort in Brookhaven [93], a fully steerable instrument was built in Tokyo [94, 95, 96]. The largest helioscope yet is the CERN Axion Solar Telescope (CAST), using a refurbished LHC test magnet ($L = 9.26 \text{ m}$, $B \sim 9.0 \text{ T}$) mounted to follow the Sun for about 1.5 h both at dawn and dusk [97, 98, 99, 100], see fig. 28. CAST began operation in 2003 and after two years of data taking achieved a limit of $g_{a\gamma} < 0.88 \times 10^{-10} \text{ GeV}^{-1}$ at 95% CL for $m_a \lesssim 0.02 \text{ eV}$. For these parameters, the conversion probability is $P_{a \rightarrow \gamma} \sim 1.3 \times 10^{-17}$. The limit on $g_{a\gamma}$ is comparable to the globular cluster limit from the energy loss in

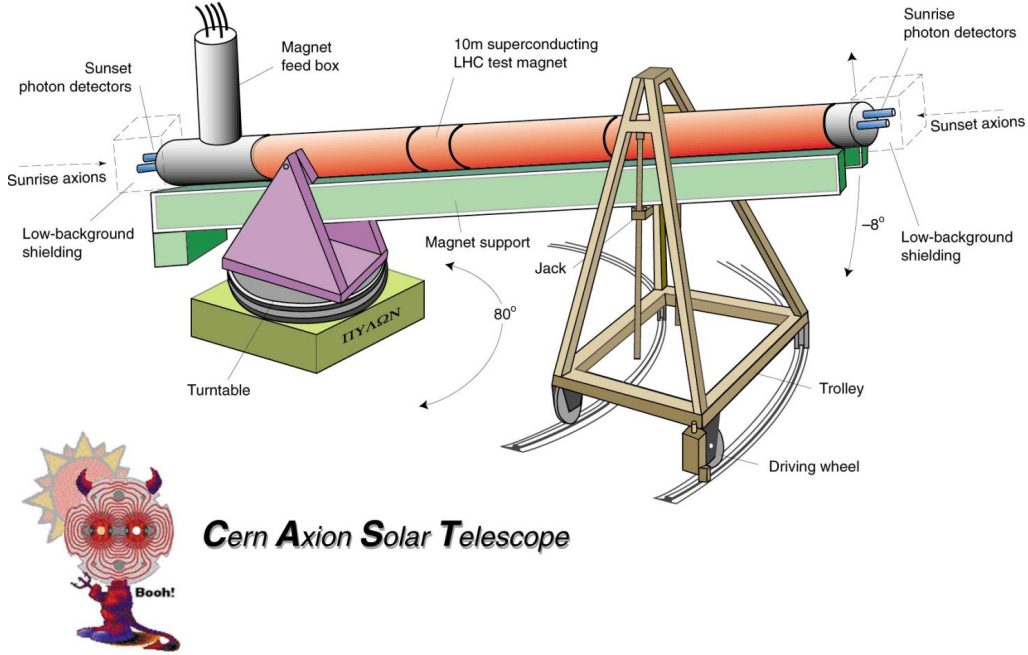


Fig. 28. – CAST experiment at CERN to search for solar axions.

horizontal-branch stars (fig. 29). Of course, it is only interesting for those axion models where they do not interact with electrons (hadronic axion models) because otherwise the white-dwarf limit is more restrictive. For axion-like particles with a two-photon vertex and small masses, CAST provides the most restrictive limit on $g_{a\gamma}$.

For $m_a \gtrsim 0.02$ eV the inverse momentum transfer becomes of order L and the oscillating term $\sin^2(qL/2)/(qL/2)^2$, which is 1 for small m_a , reduces the maximum transition probability. In other words, the axion-photon oscillation length becomes smaller than L , the conversion probability saturates and the CAST limits on $g_{a\gamma}$ degrade with increasing mass. To extend the search to larger masses one can fill the conversion pipe with helium as buffer gas to provide the photons with a refractive mass ω_{p1} . For an axion masses around $m_a \sim \omega_{p1}$ one can thus restore the full conversion efficiency [101]. This effect is rather comparable to the matter effect in neutrino flavor oscillations. Varying the gas pressure allows one to step through many search masses and extend the sensitivity to larger masses. This method was applied both in the Tokyo axion helioscope and CAST using ^4He as buffer gas, extending the limits as shown in fig. 29. For CAST, the maximum possible ^4He pressure, the vapor pressure at the liquid helium temperature of the superconducting magnet, corresponds to $\omega_{p1} \sim 0.4$ eV. To reach yet larger masses, CAST used ^3He as buffer gas; first results are shown in fig. 29. For the first time, the mass-coupling relation for KSVZ axions was crossed, the prototype hadronic axion model. Meanwhile, a search mass of 1.17 eV has been reached, essentially the largest achievable with this

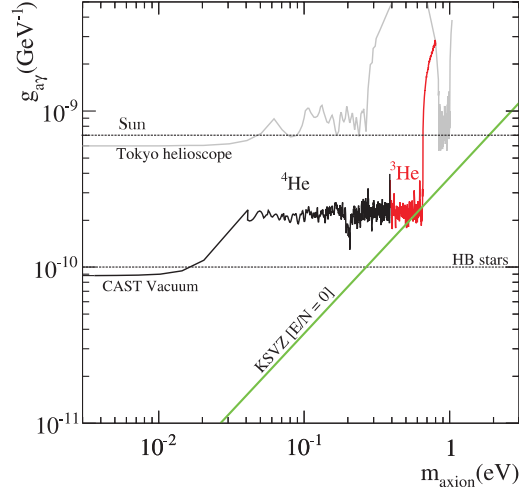


Fig. 29. – Axion $g_{a\gamma}$ - m_a exclusion range by the CAST solar axion search at CERN. (Adapted from Ref. [100].)

method because for larger gas densities absorption is becoming a serious problem. In any event, the CAST constraints now connect seamlessly to cosmological hot dark matter bounds, $m_a \lesssim 0.7$ eV, that apply because axions with the relevant parameters would have been thermally produced in the early universe [102]. To cover more realistic model space one needs to push towards smaller $g_{a\gamma}$ values. This may be achieved with a next generation axion helioscope (NGAH) [103] with comparable L and B , but much larger magnetic-field cross section (fig. 30).

We should finally make sure that using the Sun as an axion source in this way is self consistent. Axion emission represents a new energy-loss channel for the Sun and would require increased fuel consumption and thus an increased central temperature T_c . This

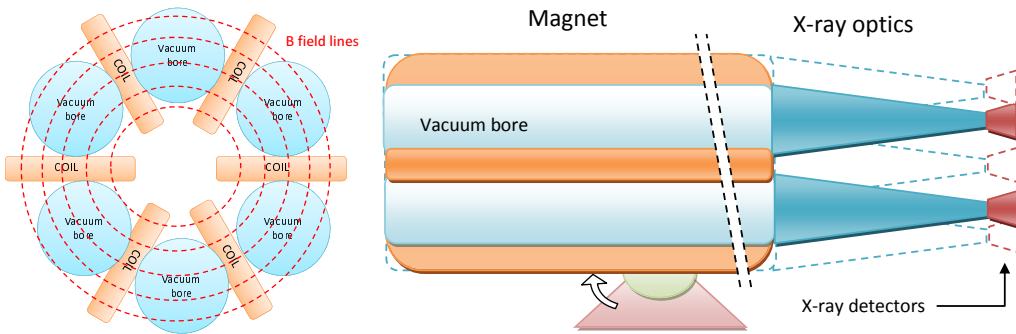


Fig. 30. – Possible design of a next-generation axion helioscope (NGAH) [103]. Each vacuum bore could have a cross section of 1 m^2 .

effect, in turn, would show up as increased neutrino fluxes, notably an increased ${}^8\text{B}$ flux that varies approximately as T_c^{18} . Based on numerical solar models with axion losses by the Primakoff process [104] one finds that the ${}^8\text{B}$ neutrino flux increases with axion luminosity L_a relative to the unperturbed flux as [105]

$$(32) \quad \Phi_{\text{B}8}^a = \Phi_{\text{B}8}^0 \left(\frac{L_\odot + L_a}{L_\odot} \right)^{4.6}.$$

After accounting for neutrino flavor oscillations, the measured $\Phi_{\text{B}8}$ agrees well with standard solar model predictions within errors, although the dominant uncertainty of the calculated fluxes evidently comes from the assumed element abundances and concomitant opacity. It appears reasonably conservative to assume the true neutrino flux does not exceed the prediction by more than 50% so that

$$(33) \quad L_a < 0.1 L_\odot.$$

This limit implies the conservative bound

$$(34) \quad g_{a\gamma} < 7 \times 10^{-10} \text{ GeV}^{-1},$$

shown as a horizontal line “Sun” in fig. 29. The Tokyo limits are just barely self-consistent whereas CAST probes to much lower $g_{a\gamma}$ values than are already excluded by the measured solar neutrino flux.

4. – Supernova neutrinos

4.1. Classification of supernovae. – Supernova (SN) explosions are the most energetic astrophysical events since the big bang [106, 107, 108]. A star suddenly brightens and at the peak of its light curve shines as bright as the host galaxy (fig. 31). Baade and Zwicky identified SNe as a new class of objects in the late 1920s and in 1934 speculated that a SN may be the end state of stellar evolution and that the energy source was provided by the gravitational binding energy from the collapse to a neutron star [5]. They also speculated that SNe were the energy source for cosmic rays. A few years later, Gamow and Schoenberg (1941) developed first ideas about the connection between core collapse and neutrinos [4], fifteen years before neutrinos were experimentally detected.

Today we believe indeed that a star with mass exceeding 6–8 M_\odot , after going through all nuclear burning stages (fig. 2), ends its life when its degenerate core has reached the Chandrasekhar limit and collapses, in the process ejecting the stellar mantle and envelope. When the core, a mass of about 1.5 M_\odot , collapses to a compact star with nuclear density and a radius of around 12 km, almost the complete gravitational binding energy of about 3×10^{53} erg is released in neutrinos of all flavors in a burst lasting a few seconds. For that period, the neutrino luminosity of a core-collapse SN is comparable to the combined photon luminosity of all stars in the visible universe. About one core collapse takes place per second in the visible universe, so on average stars liberate as much



Fig. 31. – The blue supergiant star Sanduleak –69 202 in the Large Magellanic Cloud, before and after it exploded on 23 February 1987 (SN 1987A). This was the closest observed SN since Kepler’s SN of 1603 and was the first example of a SN where the progenitor star could be identified. © Australian Astronomical Observatory.

energy in neutrinos (from core collapse) as they release in photons (from nuclear binding energy). The diffuse SN neutrino background (DSNB) in the universe from all past SNe thus provides an energy density comparable to that of the extra-galactic background light. Detecting the DSNB is the next milestone of low-energy neutrino astronomy.

What remains of a SN explosion is the dispersed ejected gas, as for example the Crab Nebula (fig. 32), the remnant of the historical SN of 1054 that was reported in Chinese records. While 99% of the liberated energy appears as neutrinos, about 1% goes into the kinetic energy of the explosion, and only about 0.01% into the optical SN outburst. The remaining neutron star usually appears as a fast-spinning pulsar, the Crab Pulsar being a prime example (fig. 32). Many pulsars receive a “kick” at birth, moving with velocities of up to 2000 km s^{-1} relative to the ejecta, implying that they even can be shot out of their host galaxy. Modern multi-dimensional SN simulations seem to be able to explain pulsar kicks by the asymmetry of the hydrodynamical explosion [109, 110].

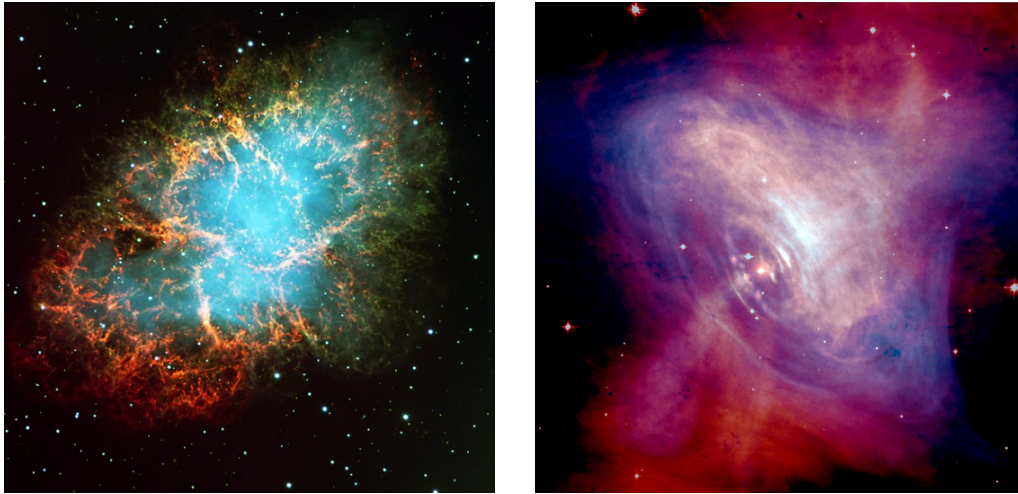


Fig. 32. – Remnant of the historical supernova of 1054. Left: Crab Nebula, the dispersed ejecta from the explosion. Credit: ESO (see also <http://apod.nasa.gov/apod/ap991122.html>). Right: Crab Pulsar in the center of the Crab Nebula, the compact neutron star remaining from the collapse, as a superposition of an HST optical image (red) and a false-color Chandra x-ray image (blue). Credit: J. Hester (ASU) et al., CXC, HST, NASA (see also <http://apod.nasa.gov/apod/ap050326.html>).

The astronomically observed SNe correspond to two entirely different classes of physical phenomena [111], i.e. core-collapse and thermonuclear SNe, the latter appearing as spectral type Ia (fig. 33). Astronomically, SN types differ in their spectra and shape of the light curves. A thermonuclear SN is thought to arise from a white dwarf that accretes matter from a companion star in a binary system. When the companion enters its giant phase, it inflates and matter can be transferred to the white dwarf. Its mass increases until it reaches its Chandrasekhar limit and collapses. However, the white dwarf consists of carbon and oxygen and the collapse triggers explosive nuclear burning, leading to complete disruption of the star. Nuclear burning beyond helium formation releases around 1 MeV energy per nucleon. A core-collapse SN, on the other hand, releases gravitational binding energy of 100–200 MeV per nucleon, of which 99% emerge as neutrinos. So both types of SN release around 1 MeV visible energy per nucleon, explaining the superficial similarity. Of course, a thermonuclear SN does not leave a pulsar behind. The spectral type Ia corresponds to a thermonuclear SN, whereas the spectral types Ib, Ic and II correspond to core collapse (fig. 33). The spectral types Ib and Ic are core-collapse events where the progenitor star has shed its hydrogen envelope before collapse.

Thermonuclear SNe are surprisingly reproducible. Their light curves form a one-parameter class of functions that can be made uniform with an empirical transformation, the Phillips relationship, that connects the peak luminosity with the duration of the light curve. In this way, SNe Ia can be used as cosmic standard candles and because they can

Spectral Type	Ia	Ib	Ic	II
Spectrum	No Hydrogen			Hydrogen
	Silicon	No Silicon		
		Helium	No Helium	
Physical Mechanism	Nuclear explosion of low-mass star	Core collapse of evolved massive star (may have lost its hydrogen or even helium envelope during red-giant evolution)		
Light Curve	Reproducible	Large variations		
Neutrinos	Insignificant	~ 100 × Visible energy		
Compact Remnant	None	Neutron star (typically appears as pulsar) Sometimes black hole		
Rate / h ² SNu	0.36 ± 0.11	0.14 ± 0.07		0.71 ± 0.34
Observed	Total ~ 5600 as of 2011 (Asiago SN Catalogue)			

Fig. 33. – Spectral classification of supernovas. The rate is measured in the supernova unit, 1 SNu = 1 SN per century per $10^{10} L_{\odot,B}$ (B-band solar luminosity).

be seen across the entire visible universe, they have been systematically used to study the expansion of the universe [112]. The 1998 detection of accelerated cosmic expansion by this method [113, 114] was awarded with the 2011 physics noble prize to Saul Perlmutter, Brian Schmidt and Adam Riess. Core-collapse SNe, on the other hand, show diverse light curves, depending on the mass and envelope structure of the progenitor star, and typically are dimmer than SNe Ia. At the time of this writing, a total of around 5600 SNe have been detected, primarily by the automated searches used for cosmology. A table of all detected SNe is maintained by the Padova Astronomical Observatory, the Asiago Supernova Catalogue (<http://graspa.oapd.inaf.it>). Note that the first observed SN in a given year, for example 2011, is denoted as SN 2011A, counting until 2011Z, and then continuing with small letters as SN 2011aa, 2011ab, and so forth. The simple alphabet was exhausted for the first time in 1988. For historical SNe, the type is clear when a pulsar or neutron star is seen in the remnant, or by the historical record of the peak luminosity and light curve. For Tycho’s SN of 1572, a spectrum could be taken in 2008 by virtue of a light echo, confirming the suspected type Ia [115].

4.2. Explosion mechanism. – While a thermonuclear SN explosion is intuitively easy to understand as a “fusion bomb,” core collapse is primarily an implosion and how to turn this into an explosion of the stellar mantle and envelope is far from trivial and indeed not yet fully resolved. The explosion could be a purely hydrodynamic event in form of the “bounce and shock” scenario, first proposed in 1961 by Colgate, Grasberger and White [116]. As the core collapses it will finally reach nuclear density where the equation of state (EoS) stiffens—essentially nucleon degeneracy provides a new source of pressure. When the collapse suddenly halts (core bounce), a shock wave forms at

its edge and travels outward, expelling the overlying layers of the star. Alternatively, Colgate and White (1966) appealed to the large neutrino luminosity that carries away the gravitational binding energy of the collapsed core [117]. Neutrinos stream through the overlying star and, by occasional interactions, transfer momentum and expel matter.

The modern picture of the “delayed explosion scenario,” or “neutrino mechanism,” incorporates elements of both ideas. It was first found by Wilson (1982) in a numerical simulation [118] and spelled out in 1984 by Bethe and Wilson [119]. In a series of cartoons (fig. 34), the events from collapse to explosion are:

- (a) **Initial phase of collapse.** A Chandrasekhar-mass iron-nickel core of an evolved massive star becomes unstable. Electrons squeezed into high-energy states begin to dissociate the heavy nuclei, convert to neutrinos, escape, and in this way accelerate the loss of pressure. Photo dissociation of heavy nuclei is also important.
- (b) **Neutrino trapping.** The core collapses, separated into a nearly homologous inner core that remains in hydrodynamic contact with itself, and the outer core with supersonic collapse. When densities of about 10^{12} g cm⁻³ are reached, neutrinos are trapped by coherently enhanced elastic scattering on large nuclei.
- (c) **Bounce and shock formation.** The inner core reaches nuclear density of about 3×10^{14} g cm⁻³, the EoS stiffens, the collapse halts, and the supersonic infall rams into a “solid wall” and gets reflected, forming a shock wave. Across the outward moving shock wave, the velocity field jumps discontinuously from supersonic inward to outward motion. The density also jumps discontinuously across the shock wave.
- (d) **Shock propagation and ν_e burst.** The shock propagates outward and eventually reaches the edge of the iron core. The dissociation of this layer allows for electron capture, $e^- + p \rightarrow n + \nu_e$, producing the “prompt ν_e burst” or “prompt deleptonization burst.” Only the outer $\sim 0.1 M_\odot$ of the former iron core deleptonizes in this way, deeper layers deleptonize slowly on the diffusion time scale of seconds.
- (e) **Shock stagnation, neutrino heating, explosion.** The shock wave runs out of pressure and stagnates at a radius of 150–200 km. Matter keeps falling in (“accretion shock”), i.e. the shock wave surfs on the infalling material that deposits energy near the nascent neutron star and powers a strong neutrino luminosity that is dominated by $\nu_e \bar{\nu}_e$ pairs. Convection sets in. Neutrino streaming continues to heat the material behind the shock wave, building up renewed pressure. After several hundred ms the shock wave takes off, expelling the overlying material.
- (f) **Neutrino cooling and neutrino-driven wind.** The neutron star settles to about 12 km radius and cools by diffusive neutrino emission over seconds. A wind of matter is blown off with chemical composition governed by neutrino processes. Nucleosynthesis takes place in this “hot bubble” region, conceivably including the r-process production of heavy neutron-rich elements.

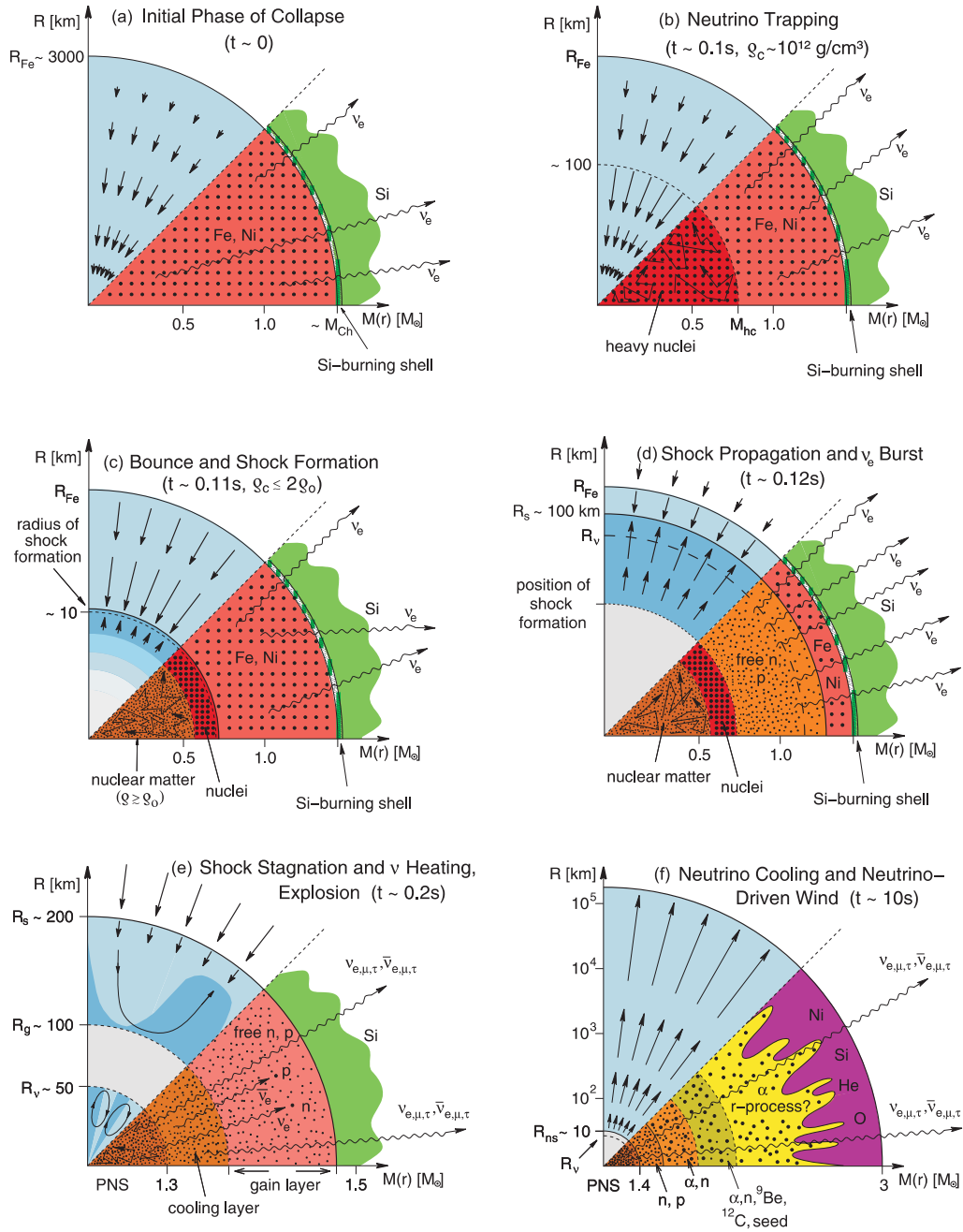


Fig. 34. – Stages of core collapse and supernova explosion as described in the text [108].

Some of these events deserve additional comments, notably the effect of neutrino trapping. In the final hot nuclear-density core, neutrinos are trapped by elastic scattering on nucleons and in addition by beta processes for the electron flavor, a typical mean free path after collapse being of order meters. However, for the SN dynamics, the early trapping at around $10^{12} \text{ g cm}^{-3}$ is crucial because the electron lepton number, initially in the form of electrons, cannot escape during infall in the form of ν_e . Therefore, the collapsed core will have essentially the same number of electrons per baryon, $Y_e \sim 0.42$, that was present in the pre-collapse nickel-iron core. In other words, radiation and thus entropy (in the form of neutrinos) cannot escape and the collapse is essentially isentropic with crucial impact on the hydrodynamics.

This “low-density” trapping occurs because of coherent enhancement of the elastic scattering cross section first pointed out in 1973 by Daniel Freedman [120] immediately after the discovery of neutral-current neutrino interactions [16]. Whenever some particle or radiation scatters on a collection of N targets, and when the momentum transfer in the collision is so small that the target is not “resolved” (the inverse momentum transfer exceeds the geometric size of the target), the targets will act as one coherent scatterer. The scattering amplitudes then add up in phase, implying that the scattering cross section is N^2 times the individual cross section. Elastic low-energy neutrino-nucleus scattering by Z^0 exchange sees N neutrons and Z protons with the effective coupling constants given in table IV. The axial-current interaction is essentially proportional to the overall nuclear spin which is small because nucleon spins tend to pair off and coherent scattering leads to a reduced overall axial-current cross section. For the vector current, the “weak charges” add coherently, but are very small for protons, $C_V \sim 0$, because $\sin^2 \Theta_W = 0.23 \sim 1/4$. So essentially only the neutrons contribute and the scattering cross section scales as N^2 for neutrino energies up to a few ten MeV. The collapsing core of an evolved star consists of iron-group elements with $N \sim 30$ so that coherently enhanced cross sections will be important [121]. Measuring coherent neutrino-nucleus scattering in the laboratory remains an open task.

Concerning the bounce-and-shock delayed explosion mechanism, a crucial point is that the edge of the inner homologous core is inside the iron core, i.e. the shock wave dissociates iron on its way out. Behind the shock wave, matter is composed of free protons, neutrons, electrons and neutrinos. Dissociating $0.1 M_\odot$ of iron requires an energy of 1.7×10^{51} erg, comparable to the explosion energy.⁽²⁾ This effect robs the shock wave of the energy to explode the star, and without neutrino heating, it re-collapses and the end state would be a black hole. Pressure can build up again by neutrino energy deposition behind the shock wave that can lead to a delayed explosion. This was first observed by Jim Wilson, a pioneer of numerical SN modeling, in 1982 with the result shown in fig. 35. On balance, the hot material above the SN core loses energy by neutrino emission, whereas the colder material behind the shock wave gains energy. The “gain radius” between the SN core and the shock wave separates the two regimes.

⁽²⁾ 10^{51} erg is sometimes denoted 1 foe for “(ten to) fifty one ergs” or more lately as 1 Bethe.

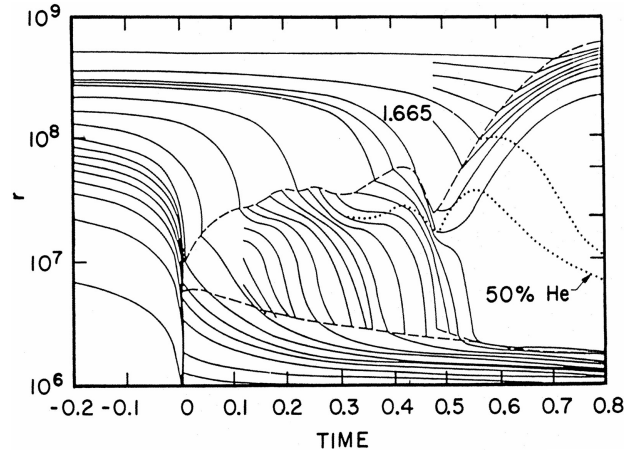


Fig. 35. – Delayed explosion scenario in Wilson’s numerical simulation (1982) [118] and explained by Bethe and Wilson [119]. Shown are the trajectories of various mass points (radius in cm, time in s). The lower dashed curve is the position of the neutrino sphere, the upper one is the shock. At $t = 0.48$ s, two neighboring trajectories begin to diverge. The region between them is the matter-depleted hot bubble region.

However, modern simulations do not produce explosions in spherical symmetry except for very low-mass progenitor stars (fig. 36). The Livermore simulations of the Wilson group used simplified neutrino transport methods and the effect of neutron-finger convection, no longer considered realistic, was used to increase the early neutrino luminosity. Sometimes it has been speculated that the explosion is aided by new channels

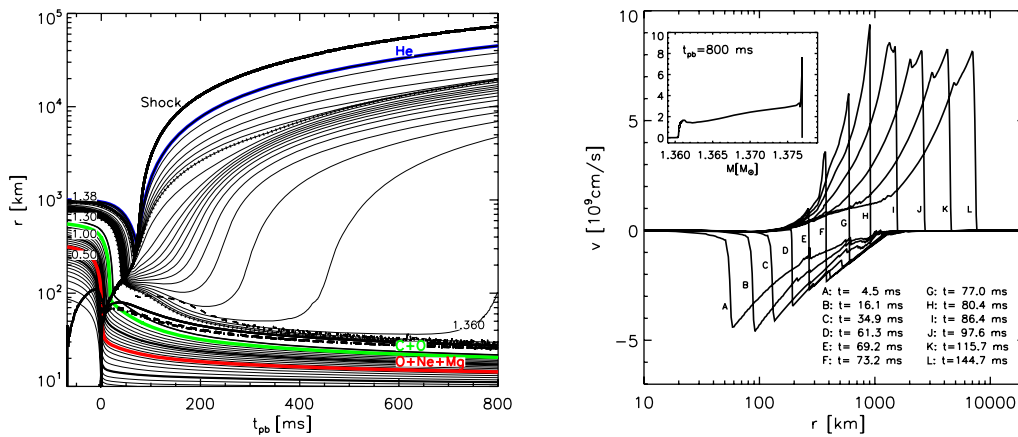


Fig. 36. – Explosion in spherical symmetry of an O-Ne-Mg-core SN, characteristic for progenitor masses $8\text{--}10 M_{\odot}$, where the accretion phase is very short [129]. Left: Trajectories of various mass shells. Right: Velocity profiles at different times.

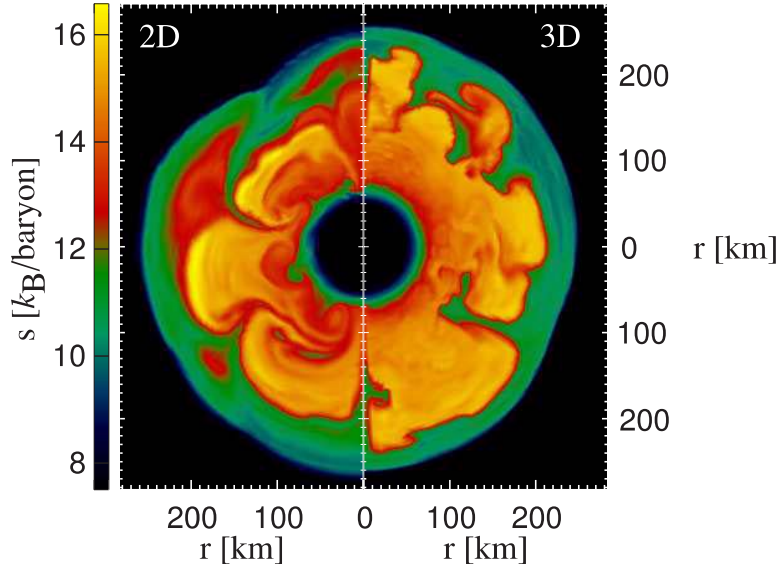


Fig. 37. – Convection between proto neutron star and stagnating shock wave [130]. Shown are entropy contours at 400 ms post bounce (pb) of an $11.2 M_{\odot}$ model from a 2D and 3D simulation which both explode at about 550 ms pb.

of energy transfer, for example by axion-like particles [122, 123], neutrino flavor oscillations [124, 125, 126], or sterile neutrinos [127, 128], but the required particle parameters are either now excluded or not necessarily well motivated.

The most probable solution of the SN explosion problem is of more mundane origin. The assumption of approximate spherical symmetry is poorly satisfied because the region between SN core and standing accretion shock is convectively unstable. Already the first 2D numerical simulations (axial symmetry) and later 3D simulations revealed the development of large-scale convective overturns (fig. 37). In addition, the standing accretion shock instability (SASI) leads to spectacular dipolar oscillations of the SN core against the “cavity” formed by the standing shock wave [131, 132, 133]. The strong deviation from spherical evolution leads to powerful gravitational wave emission (fig. 38) that can be observed from the next nearby SN with the upcoming generation of gravitational wave observatories [134, 135].

Convection and SASI activity can help with shock reheating in several ways. Hot material is dredged up from deeper layers to the region behind the shock wave. Moreover, the material is exposed to the neutrino flux for a longer time and absorbs more energy. 2D simulations lead to successful explosions for some range of progenitor masses [136]. Self-consistent 3D simulations do not yet exist because of the numerical challenge of implementing neutrino transport without simplifying assumptions in the most general case [137]. Parametric studies are not yet conclusive whether going from 2D to 3D will further enhance or perhaps even diminish the impact of non-sphericity on the final

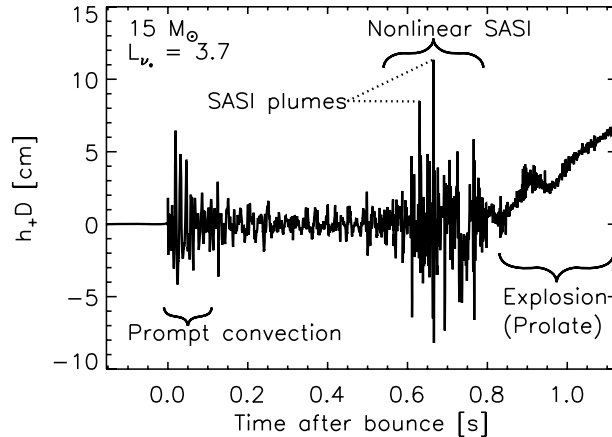


Fig. 38. – Schematic gravitational wave signal (gravitational strain h_+ times distance D) from a core-collapse SN [135]. Prompt convection, which results from a negative entropy gradient left by the stalling shock, is the first distinctive feature from approximately 0–50 ms post bounce (pb). For about 50–550 ms pb, the signal is dominated by proto neutron star (PNS) and post shock convection. Afterward and until the onset of explosion (800 ms), strong nonlinear SASI motions dominate. The most distinctive features are spikes that correlate with dense and narrow down-flowing plumes striking the PNS surface (~ 50 km). The aspherical (predominantly prolate) explosion manifests in a monotonic rise in h_+D that is similar to the “memory signature” of asymmetric neutrino emission.

explosion [130, 138]. It appears unlikely that fast rotation is crucial for the explosion because most progenitor stars do not seem to rotate fast enough. Likewise, magnetic fields would have to be exceedingly strong to have a major impact on the explosion dynamics. Transferring energy to the shock by acoustic waves [139], generated by neutron-star ringing, is probably too slow to trigger the explosion before the neutrino mechanism does the job. The final verdict on the delayed neutrino driven explosion mechanism will depend on careful numerical 3D modeling and observational input from gravitational wave and neutrino observations from the next nearby SN.

4.3. Characteristics of neutrino signal. – Observing a high-statistics neutrino signal from the next nearby SN is a major goal of low-energy neutrino astronomy and interpreting the SN 1987A signal is a crucial test for SN theory, so we first discuss what to expect for different flavors. Usually one distinguishes between three species ν_e , $\bar{\nu}_e$ and ν_x , where the latter refers to any of $\nu_{\mu,\tau}$ or $\bar{\nu}_{\mu,\tau}$. The dominant source of opacity is $\nu_e n \leftrightarrow p e^-$ and $\bar{\nu}_e p \leftrightarrow n e^+$ for the electron flavor and elastic neutral-current scattering $\nu_x N \leftrightarrow N \nu_x$ for the others. The absence of muons (mass 106 MeV) and τ -leptons (mass 1777 MeV) prevents charged-current reactions for the heavy-lepton neutrinos, although some thermal muons may exist in the innermost core if T becomes large enough. Note that νN scattering differs somewhat between $\nu_{\mu,\tau}$ and $\bar{\nu}_{\mu,\tau}$ due to weak magnetism [140], but the small difference is often ignored.

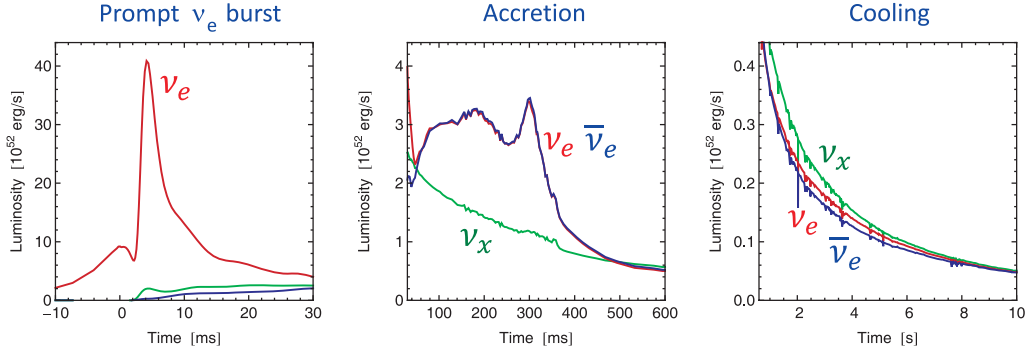


Fig. 39. – Neutrino signal using data from a spherically symmetric $10.8 M_{\odot}$ simulation of the Basel group [141]. The explosion was manually triggered.

The detectable neutrino signal has three main phases shown in fig. 39 from a numerical simulation of a $10.8 M_{\odot}$ spherically symmetric simulation of the Basel group. The explosion was triggered manually by increasing the numerical energy absorption rate in the gain region behind the shock wave. The neutrino signal has three distinct phases, corresponding to three phases of the collapse and explosion dynamics.

- (1) **Prompt ν_e burst.** The shock wave breaks through the edge of the core, allowing for fast electron capture on free protons. A ν_e burst (5–10 ms) from deleptonization of the outer core layer emerges, the emission of $\bar{\nu}_e$ and ν_x is slowly beginning. This phase should not depend much on the progenitor mass.
- (2) **Accretion phase.** The shock wave stagnates and matter falls in, releasing gravitational energy that powers neutrino emission. The ν_e and $\bar{\nu}_e$ luminosities are similar, but the ν_e number flux is larger, carrying away the lepton number of the infalling material. The heavy-lepton flavors are emitted closer to the SN core, and their flux is smaller, but their energies larger. So we typically have a hierarchy $L_{\nu_e} \sim L_{\bar{\nu}_e} > L_{\nu_x}$ and $\langle E_{\nu_e} \rangle < \langle E_{\bar{\nu}_e} \rangle < \langle E_{\nu_x} \rangle$, with $\langle E_{\bar{\nu}_e} \rangle \sim 12\text{--}13$ MeV. The duration of the accretion phase, typically a few hundred ms, and the detailed neutrino signal depend on the mass profile of the accreted matter.
- (3) **Cooling phase.** The shock wave takes off, accretion stops, the SN core settles to become a neutron star, and cools by neutrino emission. The energy stored deep in its interior, largely in the form of e and ν_e degeneracy energy, emerges on a diffusion time scale of seconds. The luminosities of all species are similar $L_{\nu_e} \sim L_{\bar{\nu}_e} \sim L_{\nu_x}$ and decrease roughly exponentially with time. The ν_e number flux is larger because of deleptonization. The average energies follow the hierarchy $\langle E_{\nu_e} \rangle < \langle E_{\bar{\nu}_e} \rangle \sim \langle E_{\nu_x} \rangle$ and decrease with time. The characteristics of the cooling phase probably do not depend strongly on the progenitor mass.

Overall, a total energy of $2\text{--}4 \times 10^{53}$ erg is emitted, depending on the progenitor mass and equation of state, very roughly equipartitioned among all flavors.

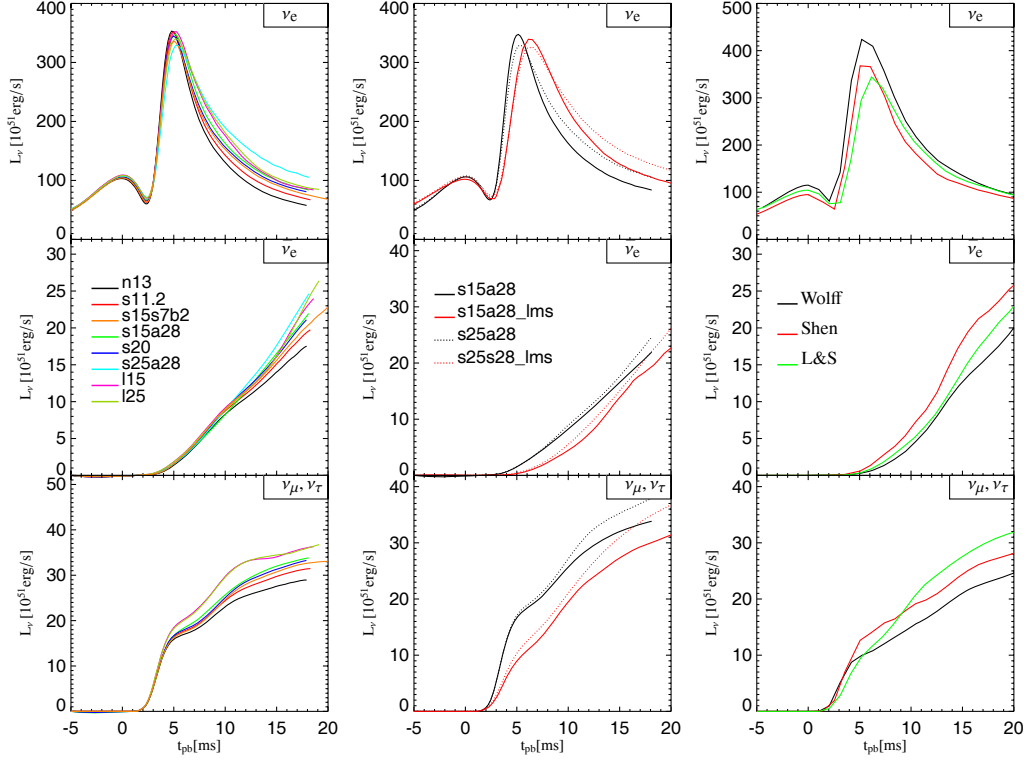


Fig. 40. – Onset of neutrino luminosity and prompt ν_e burst for a broad range of model assumptions [142]. Rows from top to bottom for the indicated flavors. Left column: Progenitor masses 11.2–25 M_\odot where the mass is indicated by the number after the first letter of the shown model name. Center column: New treatment of electron captures by nuclei [143] (red lines) compared to the traditional description (black lines) for a 15 M_\odot and 25 M_\odot star. Right column: Three different nuclear equations of state applied to a 15 M_\odot progenitor.

The most generic of these phases is the prompt ν_e burst that does not seem to depend much on the progenitor mass, assumed equation of state (EoS), or details of neutrino opacities (fig. 40). When the ν_e burst is released, the associated large chemical potential suppresses $\bar{\nu}_e$ emission, showing a slow start compared with the heavy-lepton flavors. A possible observation of the prompt ν_e burst from the next nearby SN requires a sensitive ν_e detector, in contrast to the existing large-scale $\bar{\nu}_e$ experiments that are primarily sensitive to the inverse beta reaction $\bar{\nu}_e + p \rightarrow n + e^+$. Moreover, flavor oscillations will lead to large $\nu_e \rightarrow \nu_x$ flavor conversion, depending on the value of the neutrino mixing angle θ_{13} and the atmospheric mass hierarchy.

It is only recently that SN neutrino signals have been simulated all the way to the cooling phase with modern Boltzmann solvers of neutrino transport [141, 144]. Previously expectations were often gauged after the long-term neutrino signal published by the Livermore group [145]. This pioneering work combined relativistic hydrodynamics with

multigroup three-flavor neutrino diffusion in spherical symmetry (1D), simulating the entire evolution self-consistently. The spectra were hard over a period of at least 10 s with increasing hierarchy $\langle E_{\nu_e} \rangle < \langle E_{\bar{\nu}_e} \rangle < \langle E_{\nu_x} \rangle$. These models, however, included significant numerical approximations and omitted neutrino reactions that were later recognized to be important [146]. Relativistic calculations of proto neutron star (PNS) cooling with a flux-limited equilibrium [147, 148] or multigroup diffusion treatment [149] found monotonically decreasing neutrino energies after no more than a short (~ 100 ms) period of increase. Pons et al. [150] studied PNS cooling for different EoS and masses, using flux limited equilibrium transport with diffusion coefficients adapted to the underlying EoS. They always found spectral hardening over 2–5 s before turning over to cooling.

However, the strong hierarchy of average energies, especially during the cooling signal, that was often discussed in the context of flavor oscillations, is certainly unrealistic. For the electron flavor, neutrinos are trapped by charged-current reactions and begin to stream freely at a radius where these reactions become inefficient (fig. 41). The energy-dependent decoupling radius is called “neutrino sphere” and the spectra of ν_e and $\bar{\nu}_e$ are determined by the temperature of the matter in that region. The excess of neutrons over protons implies that ν_e decouple at a larger radius and thus lower T , explaining the traditional hierarchy $\langle E_{\nu_e} \rangle < \langle E_{\bar{\nu}_e} \rangle$.

For the other species, decoupling is a two-step process, although the main opacity always arises from neutrino-nucleon scattering (fig. 41). Deep inside, other processes are important that produce $\nu_x \bar{\nu}_x$ pairs and exchange energy, notably νe and $\nu \nu$ scattering, nucleon-nucleon bremsstrahlung, and $e^- e^+$ and $\nu_e \bar{\nu}_e$ annihilation. The textbook wisdom that heavy-lepton neutrinos primarily emerge from $e^- e^+$ annihilation is incorrect. Older simulations only used νN scattering and $e^- e^+$ annihilation, missing some of the crucial processes. The energy-exchanging processes decouple at the “energy sphere,” but the

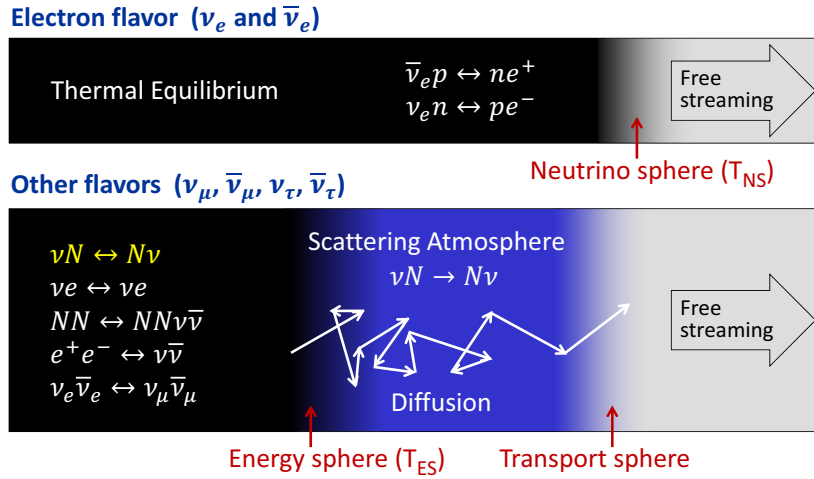


Fig. 41. – Spectra formation for neutrinos of different flavors as they stream from a SN core [151].

matter temperature in this region does not directly fix the spectrum of the ν_x that stream from the “transport sphere” where νN scattering has become ineffective. The “scattering atmosphere” between these regions, by the E^2 dependence of the νN cross section, acts as a “low pass filter,” skewing the emerging spectrum to lower energies and leading to a flux spectrum with an effective T as low as 60% of the matter T at the energy sphere [151]. Moreover, nucleon recoils, often neglected in numerical simulations, further soften the emerging spectrum. Even though the ν_x energy sphere is at much larger T than the ν_e and $\bar{\nu}_e$ neutrino sphere, the emerging spectrum at late cooling times need not be harder, and actually can be softer.

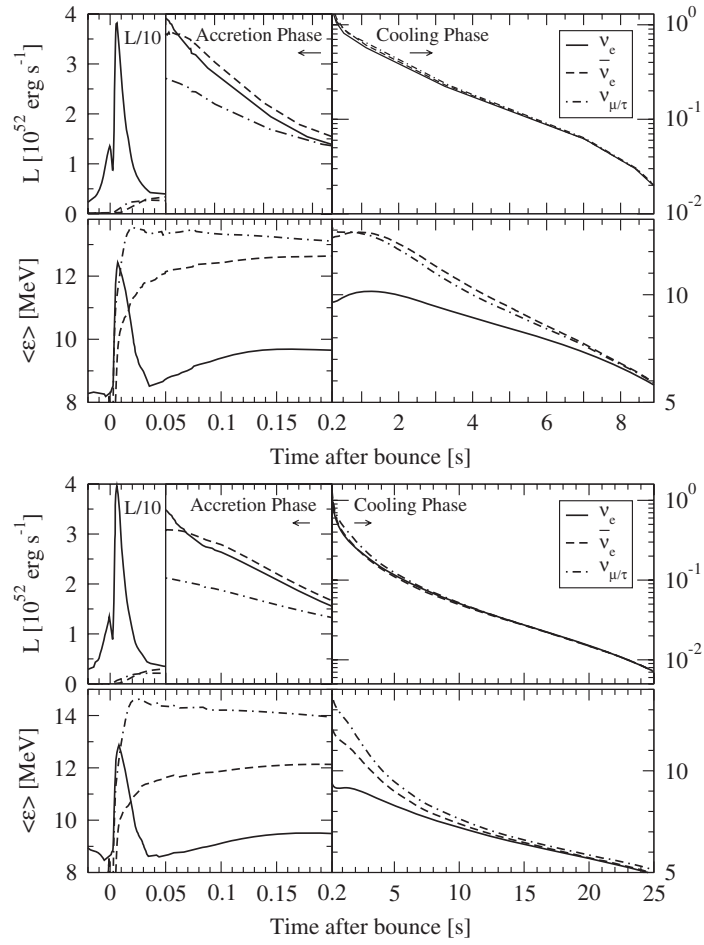


Fig. 42. – Neutrino signal from an electron capture SN (progenitor mass $8.8 M_{\odot}$) that explodes in a spherically symmetric simulation of the Garching group [144]. Top: Full set of neutrino opacities, including NN correlations that reduce the opacities. Bottom: Reduced set of opacities, no NN correlations and no nucleon recoil in νN collisions.

The impact of opacity details was studied by the Garching group for a low-mass progenitor ($8.8 M_{\odot}$) that collapses after developing a degenerate O-Ne-Mg core and explodes in a spherically symmetric simulation [144]. In fig. 42 (upper panel) we show the neutrino signal for the full set of opacities described in the Appendix of Ref. [152] that includes all processes indicated in fig. 41. In addition, nucleon-nucleon correlations in dense nuclear matter are included that significantly reduce the neutrino scattering rate. In the lower panel, these correlations and nucleon recoils are switched off, corresponding roughly to the opacities used, for example, in the Basel simulations. As a result, the cooling time increases (no NN correlations) and the emerging $\langle E_{\nu_x} \rangle$ increases (no N recoils). So the $\langle E_{\nu_x} \rangle$ values found in the long-term Basel simulations [141] probably should be reduced by 1–2 MeV to account for N recoils.

4.4. Supernova 1987A and its neutrino signal. – One of the most important events in the history of neutrino astronomy was the observation of the neutrino signal of SN 1987A that exploded on 23 February 1987 in the Large Magellanic Cloud, a satellite galaxy of our Milky Way at a distance of about 50 kpc (160,000 light years). The exploding star was the blue supergiant Sanduleak –69 202 (fig. 31), this being the first SN that could be associated with an observed progenitor star. SN 1987A was the closest visible SN in modern times. Previous historical SNe in our galaxy of the second millennium occurred in 1006 (the brightest ever observed SN), 1054 (leading to the crab nebula), Tycho’s SN of 1572, Kepler’s of 1604 and one around 1680 (Cas A). While it is believed that a few SNe occur in our galaxy per century, most are obscured by dust in the galactic plane, so one expects only about 15% of all galactic SNe to become directly visible.

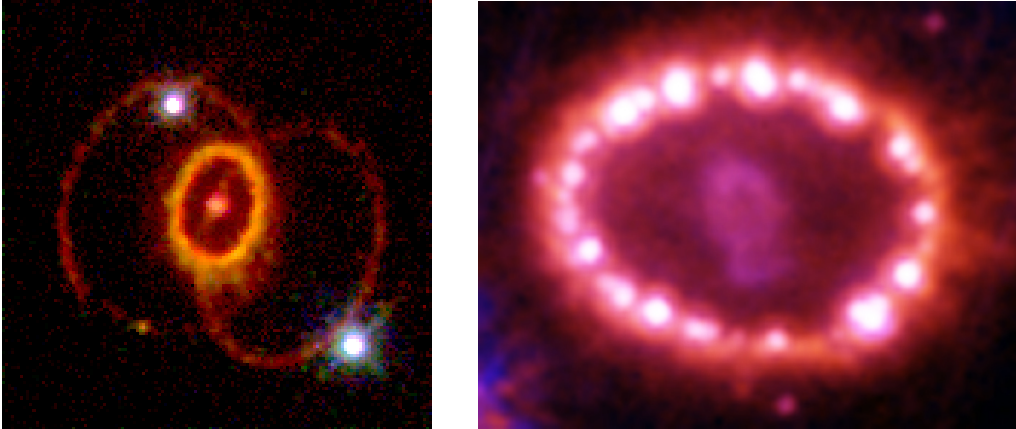


Fig. 43. – Rings of SN 1987A illuminated by the explosion. Left: Hubble Space Telescope image, taken in Feb. 1994. Credit: C. Burrows, ESA/STScI and NASA. Right: Image of inner ring, taken 28 Nov. 2003, showing bright spots caused by the supernova shock wave hitting the gas. The elongated “nebula” inside the ring is the supernova remnant. Credit: NASA, P. Challis, R. Kirshner (Harvard-Smithsonian Center for Astrophysics) and B. Sugerman (STScI).

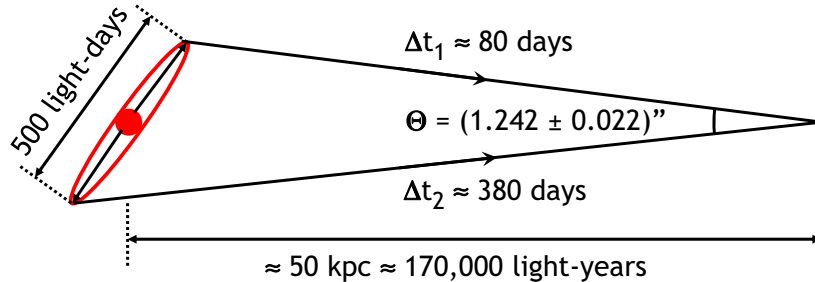


Fig. 44. – SN 1987A distance determination by the arrival time difference between the first light from the near and far side of the inner ring. The implied distance is 51.4 ± 1.2 kpc according to Panagia [153] or 47.2 ± 0.9 kpc according to Gould and Uza [154].

One of the most spectacular SN 1987A images (fig. 43) was provided by the Hubble Space Telescope after its repair, revealing a complicated ring system consisting of one inner ring and two symmetrically located outer rings, all of which derive from material ejected by the progenitor star and have nothing to do with the SN itself. The rings were illuminated by the UV flash from the SN 1987A explosion. The diameter of the inner ring is about 500 light days, so it turned on significantly after the SN explosion, and the outer rings even later. The inner ring is tilted relative to the line of sight, so the arrival time at Earth of light from different parts of the ring allows one to determine the SN distance in a purely geometric way (fig. 44). Once the shock wave reaches the inner ring years after the SN, it lights up again with knot-like structures showing up (right panel in fig. 43). Within the inner ring one sees an elongated nebula, representing the SN ejecta, providing direct evidence for the lack of spherical symmetry of the explosion. SN 1987A has provided a host of crucial astronomical information on the core collapse phenomenon and nucleosynthesis in the SN environment.

Turning to the SN 1987A neutrino detection, in the late 1970s and early 1980s, dedicated detectors were built to search for neutrinos from galactic core-collapse events. The core-collapse rate was thought to be fairly large, perhaps one every decade. The Baksan Scintillator Telescope (BST) in the Caucasus Mountains (200 tons) took up continuous operation on 30 June 1980 and has watched the neutrino sky ever since. The smaller 90 ton Liquid Scintillator Detector (LSD) took up operation in a side cavern of the Mont Blanc tunnel in October 1984 and operated until the catastrophic tunnel fire (24 March 1999). LSD was equipped with a real-time SN alert system. Moreover, in the early 1980s the search for proton decay, predicted in grand unified theories, led to the construction of the Irvine-Michigan-Brookhaven (IMB) water Cherenkov detector (6800 tons) in the USA, reporting first results in 1982 and operating until 1991. Likewise, Kamiokande (2140 tons of water) in Japan took up operation in April 1983. In order to search for solar neutrinos it was refurbished to lower the energy threshold. It began operation as Kamkiokande-II in January 1987, only weeks before SN 1987A, and took solar neutrino data until February 1995.

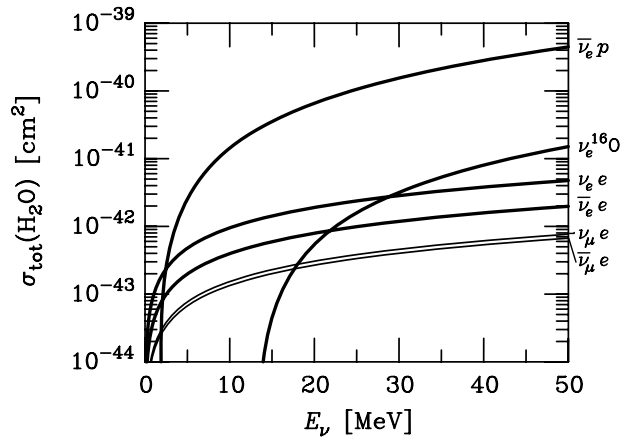


Fig. 45. – Total cross section per water molecule for the measurement of neutrinos in a water Cherenkov detector. A factor of 2 for protons and 10 for electrons is already included. A SN neutrino signal is primarily detected by inverse beta decay $\bar{\nu}_e + p \rightarrow n + e^+$.

These detectors see SN neutrinos primarily in the $\bar{\nu}_e$ channel from inverse beta decay (fig. 45). All of them reported events associated with SN 1987A arriving a few hours before the optical SN explosion as expected (fig. 46). The Kamiokande [155, 156], IMB [157, 158] and Baksan [159, 160] observations (fig. 47) are contemporaneous within

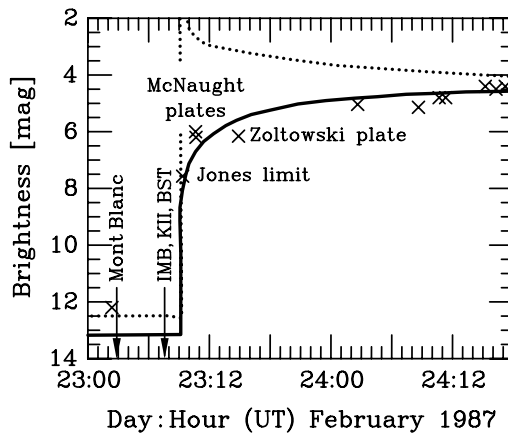


Fig. 46. – Early optical observations of SN 1987A according to the IAU Circulars, notably No. 4316 of February 24, 1987. The times of the IMB, Kamiokande II (KII) and Baksan (BST) neutrino observations (23:07:35) and of the Mont Blanc events (23:02:53) are also indicated. The solid line is the expected visual brightness, the dotted line the bolometric brightness according to model calculations. (Adapted, with permission, from Arnett et al. 1989 [166], Annual Review of Astronomy and Astrophysics, Volume 27, © 1989, by Annual Reviews Inc.)

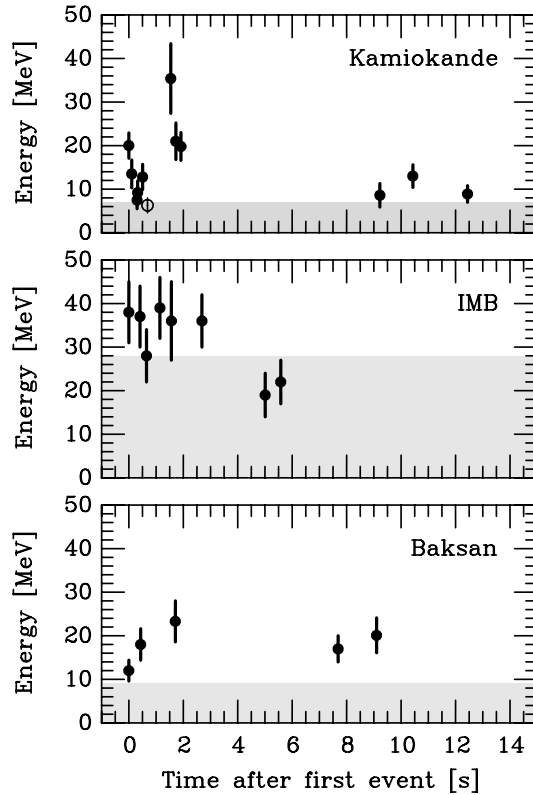


Fig. 47. – SN 1987A neutrino observations at Kamiokande [155, 156], IMB [157, 158] and Baksan [159, 160]. The energies refer to the secondary positrons from $\bar{\nu}_e p \rightarrow n e^+$. In the shaded area the trigger efficiency is less than 30%. The clock uncertainties are reported to be ± 1 min in Kamiokande, ± 50 ms in IMB, and $+2/-54$ s in BST; in each case the first event was shifted to $t = 0$. In Kamiokande, the event marked as an open circle is attributed to background.

clock uncertainties. A 5-event cluster in the LSD experiment [161, 162] was observed 4.72 h earlier and had no counterpart in the other detectors and vice versa. Moreover, the LSD detector was too small to expect a signal from as far away as the Large Magellanic Cloud. It can be associated with SN 1987A only if one invokes very non-standard double-bang scenarios of stellar collapse [163]. Still, no similar event cluster was ever observed again in LSD over its 15 years of operation and its origin remains unresolved. A lively account of the exciting and somewhat confusing history of the SN 1987A neutrino detection was given by M. Koshiba [164] and A. Mann [165].

The event energies and signal duration roughly agree with theoretical expectations. The IMB event energies are larger than those in Kamiokande, in part because IMB had a higher energy threshold—it had not been optimized for low-energy neutrino detection. While the instantaneous neutrino spectra tend to be “pinched,” i.e. a bit narrower than

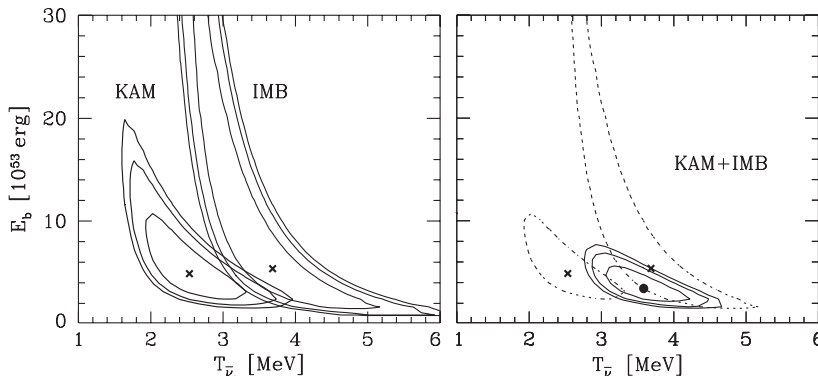


Fig. 48. – Confidence contours for the signal fit parameters E_b (total released binding energy) and $\bar{\nu}_e$ spectral temperature $T_{\bar{\nu}_e}$ based on the Kamiokande and IMB data and a combined fit [167]. The confidence contours are for 68.3%, 90% and 95.4%.

a simple thermal spectrum, the time-integrated flux probably can be reasonably well approximated by the Maxwell-Boltzmann form $F_{\bar{\nu}_e}(E) \propto E^2 e^{-E/T_{\bar{\nu}_e}}$. With this assumption one can derive the fit parameters $T_{\bar{\nu}_e}$ and total emitted energy E_b , assuming 1/6 of the total energy arrived in the $\bar{\nu}_e$ channel. Confidence contours for the fit parameters E_b and $T_{\bar{\nu}_e}$ are shown in fig. 48; other authors have found similar results. The Kamiokande data alone imply a rather soft spectrum, so there is tension between the data sets, but they are statistically compatible. Theoretically one expects $E_b = 2\text{--}4 \times 10^{53}$ erg and $T_{\bar{\nu}_e} = \frac{1}{3} \langle E_{\bar{\nu}_e} \rangle \sim 4$ MeV if one ignores the possibility of flavor oscillations. Flavor oscillations are unavoidable, so if the $\langle E_{\bar{\nu}_e} \rangle$ predictions are roughly correct, $\langle E_{\bar{\nu}_x} \rangle$ at the source cannot be much larger than $\langle E_{\bar{\nu}_e} \rangle$, in contrast to the older simulations, but in agreement with the more recent picture.

Much more sophisticated analyses have been performed [168, 169, 170], but in the end the information contained in a sparse signal is limited. The SN 1987A neutrino observations have provided a general confirmation of the neutrino emission scenario with appropriate energies over a diffusion time scale of seconds. A serious quantitative test of the core collapse paradigm, however, requires a high-statistics observation, ideally in several complementary detectors, including gravitational wave observatories.

4.5. Neutrinos from the next nearby supernova. – Galactic SNe are rare, perhaps a few per century (table X), so measuring a high-statistics neutrino signal from the next nearby SN is a once-in-a-lifetime opportunity that should not be missed. Many currently operating detectors with a primary physics focus on other topics have good SN sensitivity (table IX), providing for an optimistic outlook that a high-statistics SN neutrino light curve will be measured eventually [173]. When it occurs, because neutrinos arrive a few hours before the visual SN explosion, an early warning can be issued. To this end, several detectors together form the Supernova Early Warning System (SNEWS), issuing an alert if they measure candidate signals in coincidence [174, 175, 176].

TABLE IX. – *Existing and near-future SN neutrino detectors and event rates for a SN at 10 kpc, emission of 5×10^{52} erg in $\bar{\nu}_e$, average energy 12 MeV, and thermal energy distribution. For HALO and ICARUS, the event rates depend on assumptions about the other species. For references and details see Ref. [173].*

Detector	Type	Location	Mass [kt]	Events	Status
IceCube	Ice Cherenkov	South Pole	0.6/OM	10^6	Running
Super-K IV	Water	Japan	32	7000	Running
LVD	Scintillator	Italy	1	300	Running
KamLAND	Scintillator	Japan	1	300	Running
SNO+	Scintillator	Canada	1	300	Commissioning 2013
MiniBOONE	Scintillator	USA	0.7	200	Running
Borexino	Scintillator	Italy	0.3	80	Running
BST	Scintillator	Russia	0.2	50	Running
HALO	Lead	Canada	0.079	tens	Almost ready
ICARUS	Liquid argon	Italy	0.6	200	Running

The workhorse process remains inverse beta decay, $\bar{\nu}_e + p \rightarrow n + e^+$, either in water Cherenkov detectors consisting of H_2O as target, or in scintillator detectors, consisting primarily of mineral oil with an approximate chemical composition C_nH_{2n} . Therefore, 1 kt of water contains about 6.7×10^{31} protons, whereas 1 kt of mineral oil about 8.6×10^{31} protons. The total inverse beta cross section is at lowest order [171, 172]

$$(35) \quad \sigma_{\bar{\nu}_e p} = 9.42 \times 10^{-44} \text{ cm}^2 (E_\nu / \text{MeV} - 1.3)^2.$$

To estimate the expected event rate we assume a fiducial SN at a distance of 10 kpc that emits a total of 3×10^{53} erg in the form of neutrinos, and 1/6 of that in the form of $\bar{\nu}_e$ with an average energy $E_{\text{av}} = \langle E_{\bar{\nu}_e} \rangle = 12$ MeV as suggested by recent numerical work and compatible with SN 1987A. These assumptions provide for a total number of 2.6×10^{57} emitted $\bar{\nu}_e$ and a fluence (time-integrated flux) at Earth of

$$(36) \quad F_{\bar{\nu}_e} = 2.18 \times 10^{11} \text{ cm}^{-2} \frac{L_{\bar{\nu}_e}}{5 \times 10^{52} \text{ erg}} \frac{12 \text{ MeV}}{E_{\text{av}}} \left(\frac{10 \text{ kpc}}{D} \right)^2.$$

We assume that the time-integrated spectrum follows a Maxwell-Boltzmann distribution

$$(37) \quad f(E_\nu) = \frac{27}{2} \frac{E_\nu^2}{E_{\text{av}}^3} e^{-3E_\nu/E_{\text{av}}}$$

that could also be written in terms of the spectral temperature $T = E_{\text{av}}/3$. We then expect 223 produced positrons per kiloton water, the exact event rate depending on the detector threshold and efficiency, and about 287 positrons per kiloton mineral oil.

Somewhat surprisingly, the largest SN neutrino detector to date is the high-energy neutrino telescope IceCube at the South Pole (fig. 49), where 1 km^3 of ice is instrumented

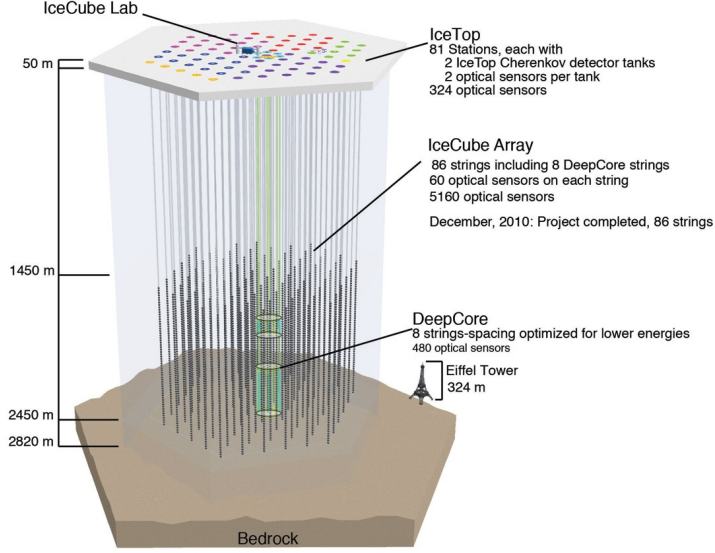


Fig. 49. – IceCube neutrino observatory at the South Pole. Credit: IceCube Collaboration.

with a total of 5160 optical modules (OMs). It consists of 78 sparsely instrumented strings (17 m vertical distance between OMs, 125 m horizontal string distance) and 8 densely instrumented strings (7–10 m vertical distance, 60 m horizontal distance), forming the deep core sub-detector that is optimized for lower-energy neutrinos in the range 10–300 GeV. When a SN neutrino burst passes through the ice, the inverse beta reaction produces positrons which in turn produce Cherenkov light, but typically at most one photon from any one $\bar{\nu}_e$ is picked up, no Cherenkov rings can be reconstructed, and the SN burst simply adds to the noise in the OMs. For our fiducial SN at 10 kpc, each OM picks up a total of around 300 Cherenkov photons over a few seconds, compared with an internal singles noise rate of 286 Hz. The correlated noise among all OMs therefore provides a highly significant signal [177, 178, 179, 180], even though there is no spectral information. For neutrino telescopes in water, this method is strongly constrained by the high level of radioactive backgrounds, notably potassium, that is dissolved in sea water.

Assuming for simplicity an exact E_ν^2 dependence of the inverse beta cross section, an approximate expression for the count rate above background in IceCube is [181]

$$(38) \quad R_{\bar{\nu}_e} = 114 \text{ ms}^{-1} \frac{L_{\bar{\nu}_e}}{10^{52} \text{ erg s}^{-1}} \left(\frac{10 \text{ kpc}}{D} \right)^2 \left(\frac{E_{\text{rms}}}{15 \text{ MeV}} \right)^2 \quad \text{where} \quad E_{\text{rms}}^2 = \frac{\langle E_{\bar{\nu}_e}^3 \rangle}{\langle E_{\bar{\nu}_e} \rangle}.$$

Note that for a Maxwell-Boltzmann spectrum one finds $E_{\text{rms}} = \sqrt{20/9} E_{\text{av}} \sim 1.49 E_{\text{av}}$. However, the instantaneous spectra tend to be pinched and so a realistic E_{rms} would be

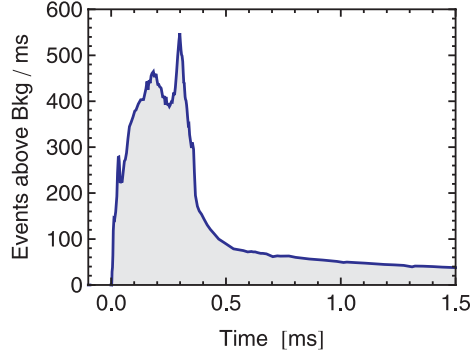


Fig. 50. – Neutrino signal above background in Icecube for a fiducial SN at 10 kpc, based on the $10.8 M_{\odot}$ model of the Basel group shown in figure 39.

smaller. Based on the Basel SN model of fig. 39 we show the expected counting rate above background in fig. 50. This is to be compared with a typical IceCube background rate of 1300 ms^{-1} , larger than the signal and thus dominating the shot noise. If one were to use 5 ms bins, the 1σ shot noise would be $\pm 16 \text{ ms}^{-1}$ or about 5% during the accretion phase in fig. 50.

The strength of IceCube as a SN neutrino detector is the large rate of uncorrelated Cherenkov photons that minimizes the shot noise relative to the number of events and thus offers superior resolution for the signal time variation. One application is to determine the signal onset to within a few ms that would be particularly useful in combination with gravitational wave detection of the bounce time [182, 183]. Another application is to resolve fast time variations caused by convective overturns and strong SASI activity, leading to significant signal modulations on time scales of tens of ms (fig. 51). The shown

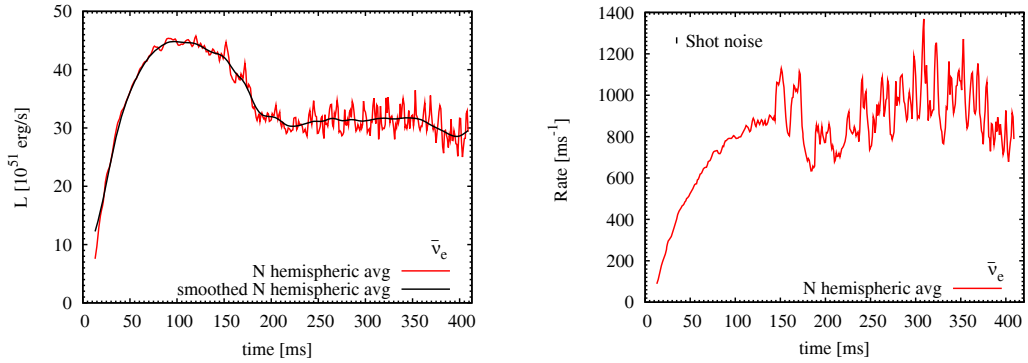


Fig. 51. – Supernova $\bar{\nu}_e$ signal [181] from a 2D Garching simulation [134]. Left: Luminosity and an approximate time average in the north polar direction. Right: Corresponding IceCube detection rate and 1σ shot noise for an assumed 1 ms bin width.

example is based on a 2D simulation where the SASI activity may be stronger than in 3D. It depends both on the strength of the modulations and the distance of the SN whether these features can be resolved.

The other existing large detector is Super-Kamiokande, after refurbished electronics in its incarnation IV, with a lowered energy threshold. Its main detection channel is once more inverse beta decay, but of course it obtains event-by-event energy and directional information. Like IceCube, it will provide a superb neutrino light curve, except with less power to resolve fast time variations. As a sub-dominant channel, Super-K can statistically identify electron recoil events by their angular distribution, $\nu + e \rightarrow e + \nu$, that is primarily sensitive to ν_e and $\bar{\nu}_e$ (fig. 52). In this way, the SN can be located in the sky by neutrinos alone [203, 204], a possibility that is of particular interest if the SN is visually obscured.

Telling $\nu e \rightarrow e\nu$ from $\bar{\nu}_e p \rightarrow ne^+$ on an event-by-event basis requires to identify the final-state neutron. It recombines with a proton to form a deuteron, emitting a 2.2 MeV γ -ray that is below threshold in a water Cherenkov detector. If a sufficient amount of gadolinium, one of the most efficient neutron catchers, is dissolved in the tank, the subsequent 8 MeV γ cascade could be measured, tagging the inverse beta reaction [184, 185]. A dedicated R&D program, the ongoing EGADs project, evaluates the full-scale realistic feasibility of this approach. Without neutron tagging, the SN pointing accuracy is 7.8° for the 95% CL half-cone opening angle, whereas for a 90% tagging efficiency this would improve to 3.2° . For a megaton water Cherenkov detector ($30\times$ Super-K), these numbers improve to 1.4° and 0.6° , respectively [204].

The ongoing long-baseline neutrino oscillation programs worldwide suggest that at least one megaton-class water Cherenkov detector will be built in the foreseeable future [173]. Such projects are discussed in Japan (“Hyper-Kamiokande”), in Europe (“Memphys”) and the US (“LBNE”). Such developments will boost the SN detection capabilities even further and provide yet more statistics for a SN neutrino light curve.

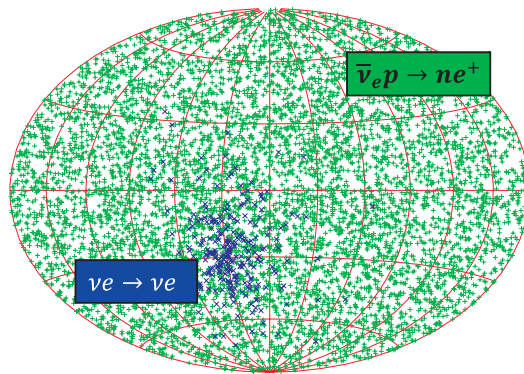


Fig. 52. – Angular distribution of $\bar{\nu}_e p \rightarrow ne^+$ events (green) and elastic scattering events $\nu e \rightarrow e\nu$ (blue) of a simulated SN [204].

Scintillator detectors are another class of $\bar{\nu}_e$ detectors that can be scaled to large volume. One advantage is the low energy threshold and concomitant native neutron-tagging capability as well as stronger light output implying superior energy resolution. Of course, there is hardly any directional information except in a weak statistical sense by the displacement of the positron annihilation and neutron capture vertices [186, 187]. Each of the existing detectors (table IX) would provide a significant SN neutrino light curve and energy information, and taken together they provide formidable statistics. A 50 kt scintillator detector, Low Energy Neutrino Astronomy (LENA), is under discussion [188] that combines the advantage of the scintillator technique with the size of Super-Kamiokande. For the SN parameters assumed earlier, it would register about 1.1×10^4 inverse beta events, somewhat more than Super-K, with better energy resolution and about 600 electron scattering events. One may also measure proton recoil [189, 190], $\nu p \rightarrow p\nu$, with around 1300 events in LENA. Other subdominant channels that may become detectable with a few hundred events each are the carbon reactions (i) $\nu + {}^{12}\text{C} \rightarrow {}^{12}\text{C}^* + \nu$ followed by ${}^{12}\text{C}^* \rightarrow {}^{12}\text{C} + \gamma$, (ii) $\bar{\nu}_e + {}^{12}\text{C} \rightarrow {}^{12}\text{B} + e^+$ followed by ${}^{12}\text{B} \rightarrow {}^{12}\text{C} + e^- + \bar{\nu}_e$, and (iii) $\nu_e + {}^{12}\text{C} \rightarrow {}^{12}\text{N} + e^-$ followed by ${}^{12}\text{N} \rightarrow {}^{12}\text{C} + e^+ + \nu_e$.

A new type of SN detector, HALO, is being realized in SNO Lab, using 79 tons of existing lead as a target. The relevant processes are the dominant charged-current reactions $\nu_e + {}^{208}\text{Pb} \rightarrow {}^{207}\text{Bi} + n + e^-$ and $\nu_e + {}^{208}\text{Pb} \rightarrow {}^{206}\text{Bi} + 2n + e^-$ as well as the neutral-current reactions $\nu + {}^{208}\text{Pb} \rightarrow {}^{207}\text{Pb} + n$ and $\nu + {}^{208}\text{Pb} \rightarrow {}^{206}\text{Pb} + 2n$. In all cases, one measures the produced neutrons with ${}^3\text{He}$ detectors remaining from the decommissioned SNO solar neutrino experiment. HALO provides complementary information on the spectrum because its high threshold makes it especially sensitive to the high-energy tail of the neutrino distribution [194, 195, 196].

In the SN neutrino signal, the spectral differences between different flavors are much larger in the ν channel than the $\bar{\nu}$ channel, and in particular the prompt ν_e burst is a dramatic feature, yet the existing large detectors are all primarily sensitive to $\bar{\nu}_e$. A large ν_e detector could be based on the liquid argon time projection chamber technique, with the recently commissioned 600 t ICARUS module in Gran Sasso being an operational prototype [191]. SN neutrinos are detected by the main reaction $\nu_e + {}^{40}\text{Ar} \rightarrow {}^{40}\text{K} + e^-$ plus some subdominant channels, so one has an excellent ν_e detector [192]. While ICARUS would measure a few hundred events from a SN at 10 kpc, a much bigger detector, perhaps up to 100 kt, is discussed in Europe under the name of GLACIER [193].

How often can we expect a signal from any of these detectors? Even the largest of the existing instruments can only cover our own galaxy and its satellites such as the Large Magellanic Clouds. Reaching the Andromeda galaxy, the Milky Way's large partner galaxy at a distance of around 760 kpc, requires bigger detectors such as a megaton class water Cherenkov instrument that could then get a few tens of events. For a high-statistics observation we remain constrained to our own galaxy and its satellites. The estimated SN rates by various techniques are summarized in table X, i.e. we can expect a few core collapses per century. Except for SN 1987A in the Large Magellanic Cloud, no core collapse was observed over more than 30 years of neutrino observations, already implying a nontrivial upper limit on the rate of possible failed SNe.

TABLE X. – *Estimated rate of galactic core-collapse SNe per century.*

Method	Rate	Authors	Refs.
Scaling from external galaxies	2.5 ± 0.9	van den Bergh & McClure (1994)	[197, 199]
	1.8 ± 1.2	Cappellaro & Turatto (2000)	[198, 111]
Gamma-rays from galactic ^{26}Al	1.9 ± 1.1	Diehl et al. (2006)	[199]
Historical galactic SNe (all types)	5.7 ± 1.7	Strom (1994)	[200]
	3.9 ± 1.7	Tammann et al. (1994)	[201]
No neutrino burst in 30 years ^a	< 7.7 (90% CL)	Alekseev & Alekseeva (2002)	[202]

^aWe have scaled the limit of Ref. [202] to 30 years of neutrino sky coverage.

The possible distribution of core-collapse SNe in the galaxy must follow the regions of star formation, notably in the spiral arms. The expected distance distribution for two simple models are shown in fig. 53. While being different in detail, the main point is that the distributions are very broad and that 10 kpc is probably a reasonable benchmark value. Sometimes our distance to the galactic center of 8.5 kpc is used for this purpose, but SNe are not especially likely in the galactic center region. However, the expected distribution is so broad that any specific distance is unlikely to be “typical” for the next nearby SN. In this sense, any forecast of what can be learnt should, in principle, cover a broad range of cases. Since any distance, say, between 2 and 20 kpc is almost equally likely, the dynamical range of plausible event statistics is about a factor of 100.

Of course, we may be especially lucky and the next galactic SN happens very nearby in that the red supergiant Betelgeuze in the constellation Orion could explode (fig. 54), causing around 4×10^7 events in Super-Kamiokande. To handle the possibility of such a

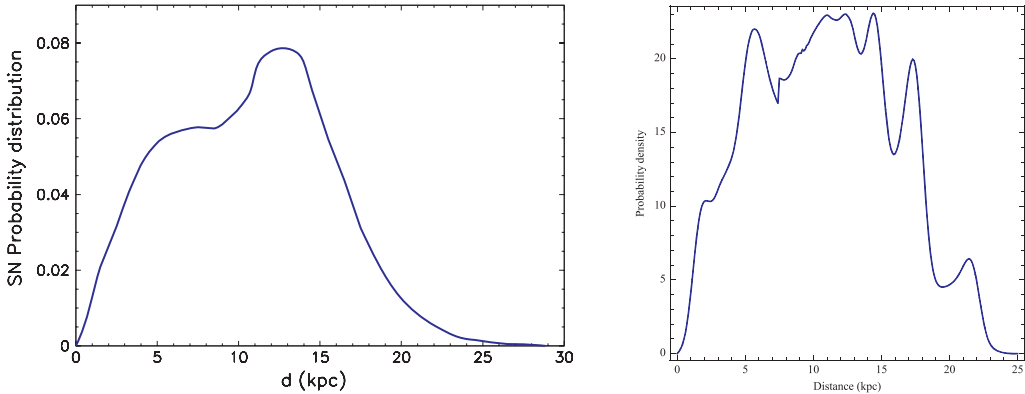


Fig. 53. – SN distance distribution relative to the Earth for a simple model of progenitor distribution [205] (left) and one taking account of the spiral arm structure [206] (right).

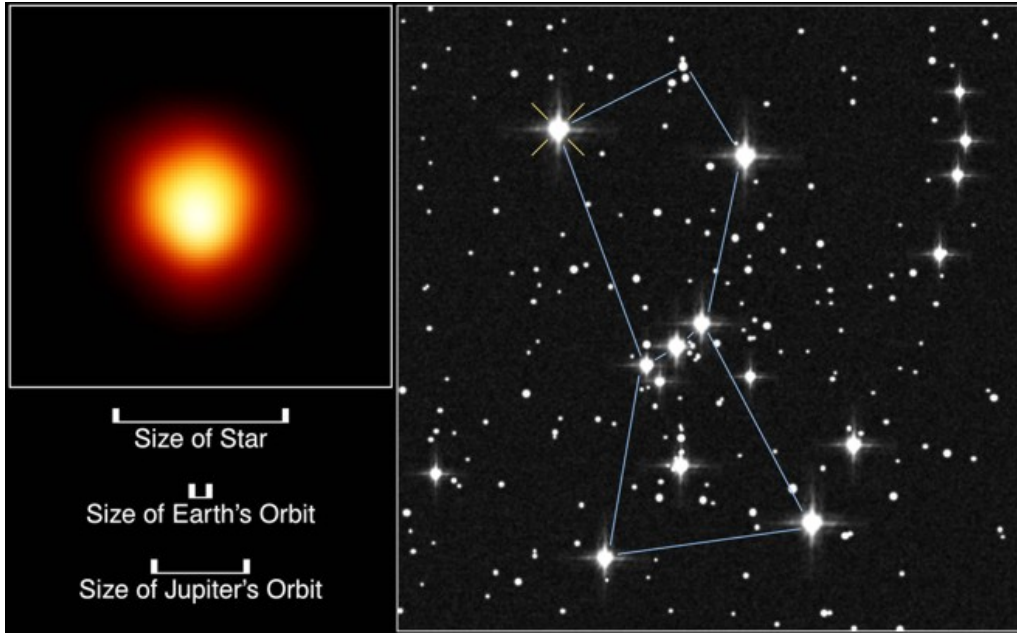


Fig. 54. – The star Betelgeuze (Alpha Orionis) at a distance of 130 pc (425 lyr) is the first resolved image of a star other than the Sun. It is a candidate for the next nearby SN explosion. HST image taken in ultraviolet on 3 March 1995. Credit: A. Dupree (Harvard-Smithsonian CfA), R. Gilliland (STScI), NASA and ESA.

large data flow, special measures for the data acquisition system have to be taken. This is the closest conceivable SN among the known stars in the solar neighborhood, but would still be at a safe distance regarding life on Earth. For such a close SN, one may be able to pick up the neutrino signal of the pre-supernova evolution when silicon burning produces a huge flux of thermal neutrinos with enough energy for the inverse beta reaction. The increased neutron production rate for a few weeks before the explosion could provide early warning of the imminent Betelgeuze explosion [207].

Reaching beyond the galaxy and its satellites requires new strategies. Even megaton class detectors will only reach to the Andromeda galaxy and get only a few tens of events from that distance. A different strategy would be a multi-megaton detector such as the proposed 5 megaton Deep-TITAND, that could pick up mini bursts of a few events from all SNe out to few-Mpc distances [208]. In this way one could build up an average SN neutrino spectrum from many different SNe over a few years. Another way to realize the same idea is with an upgraded deep-core detector in IceCube that could be instrumented with an ever denser grid of optical modules (PINGU project) such as to reach eventually the 10 MeV range threshold [209]. Conceivably one could construct a 10 megaton detector in this way, providing for a novel perspective for low-energy neutrino astronomy.

4.6. *Diffuse supernova neutrino background (DSNB)*. – Another way to reach beyond the galaxy is to search for the diffuse SN neutrino background (DSNB) from all past SNe in the universe [210]. While SNe in any given galaxy are rare, the emitted energy in each core collapse is so large that the long-term average of total neutrino energy emitted is almost exactly the same as the total photon energy. The cosmic average light emitted by all stars adds up to the extra galactic background light (EBL) with an intensity of 50–100 nW m⁻² ster⁻¹, corresponding to an energy density of 13–26 meV cm⁻³, i.e. about 10% of the energy density provided by the cosmic microwave background. In this sense stellar populations emit about as much gravitational binding energy (in the form of neutrinos) as they emit nuclear binding energy (mostly in the form of photons and some thermal neutrinos).

The DSNB signal depends on three ingredients. First, the cosmic core collapse rate R_{cc} , about 10 per second in the causal horizon; this is determined by astronomical measurements that are already precise and quickly improving (fig. 55). Second, the average SN neutrino emission, which is expected to be comparable for all core collapses, including those that fail and produce black holes; this is the quantity of fundamental interest. Third, the detector capabilities, including the energy dependence of the cross section and detector backgrounds.

Detecting the DSNB is important even if a Milky Way burst is observed. DSNB $\bar{\nu}_e$ will provide a unique measurement of the average neutrino emission spectrum to test SN simulations. Comparison to SN 1987A and an eventual Milky Way SN will test the variation between core collapses. While the statistics of DSNB events will be low with foreseeable detectors, comparable to those of SN 1987A, this data will more effectively measure the exponentially falling tail of the spectrum at high energies. The DSNB is also a new probe of stellar birth and death: its energy density is comparable to that of

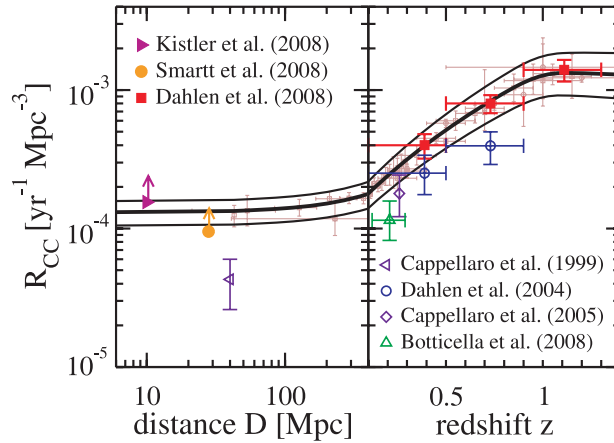


Fig. 55. – Core collapse rate as a function of redshift according to different measurements of the star formation rate [211].

photons produced by stars, but the DSNB is unobscured and has no known competition from astrophysical sources.

The DSNB event rate spectrum follows from a line of sight integral for the radiation intensity from a distribution of distant sources. After integrating over all angles due to the isotropy of the DSNB and the transparency of Earth, it is, in units $\text{s}^{-1} \text{MeV}^{-1}$,

$$(39) \quad \frac{dN_{\text{vis}}}{dE_{\text{vis}}} = N_p \sigma(E_\nu) \int_0^\infty R_{\text{cc}}(z) \left\{ (1+z) \phi[E_\nu(1+z)] \right\} \left| \frac{dt}{dz} \right| dz,$$

where E_{vis} is the detected positron energy. On the right hand side, before the integral is the number of targets (protons) times the detection cross section. Under the integral, the first ingredient is the comoving cosmic core-collapse rate, in units $\text{Mpc}^{-3} \text{yr}^{-1}$; it evolves with redshift (fig. 55). The second is the average time-integrated emission per SN, in units MeV^{-1} ; redshift reduces emitted energies and compresses spectra. The last term is the differential distance, where $|dt/dz|^{-1} = H_0(1+z)[\Omega_\Lambda + \Omega_m(1+z)^3]^{1/2}$; the cosmological parameters are taken as $H_0 = 70 \text{ km s}^{-1} \text{Mpc}^{-1}$, $\Omega_\Lambda = 0.7$, and $\Omega_m = 0.3$. The cosmological factor and the SN rate derived from star formation rate data are really one combined factor proportional to the ratio of the average luminosity per galaxy in SN neutrinos relative to stellar photons. For the example of the foreseen 50 kt LENA scintillator detector, with a fiducial mass of 44 kt, one then finds the detection spectrum shown in fig. 56. Over a measurement time of 10 years it would collect a significant data set, depending on the emission spectrum of SN neutrinos.

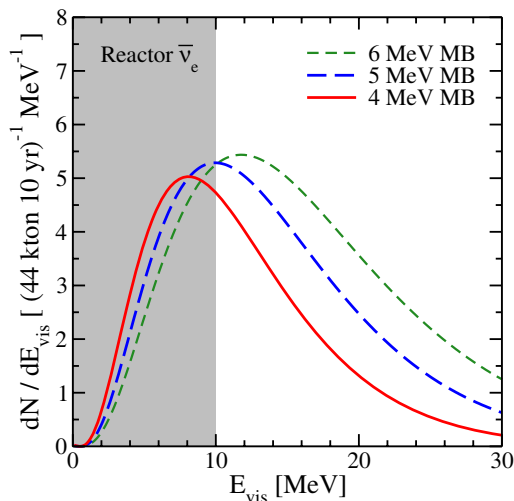


Fig. 56. – Detection positron spectrum in the possible 50 kt LENA scintillator detector for different values of the assumed T of the average SN $\bar{\nu}_e$ emission spectrum [188]. Below about 10 MeV, the background $\bar{\nu}_e$ flux from power reactors completely masks the DSNB. At higher energies, backgrounds from cosmic rays kick in, but should be controllable for 10–30 MeV.

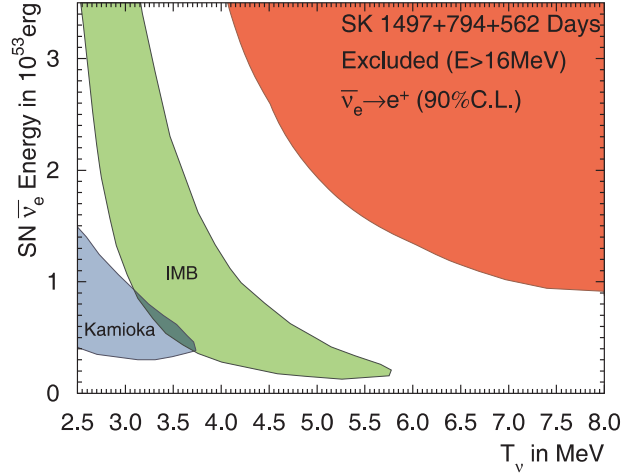


Fig. 57. – DSNB exclusion limits (90% CL), assuming the average SN $\bar{\nu}_e$ emission spectrum is described by a thermal Maxwell-Boltzmann spectrum [212]. For comparison, the best-fit regions for the SN 1987A signal of fig. 48 are also shown.

The detection is more difficult for a water Cherenkov detector because it lacks the native neutron tagging capability due to its larger energy threshold. Therefore, it is not possible to reject irreducible backgrounds caused by cosmic ray events. The Super-Kamiokande detector places an upper $\bar{\nu}_e$ flux limit of $2.8\text{--}3.0\text{ cm}^{-2}\text{ s}^{-1}$ for neutrino energies above 17.3 MeV, the exact value depending on the assumed spectrum [212]. Depending on the assumed total energy emitted in $\bar{\nu}_e$ by any given SN and the spectral shape assumed to be thermal, they find the exclusion range shown in fig. 57. To achieve a detection in Super-K one needs neutron-tagging capability that is currently being developed in terms of loading the detector with gadolinium as explained earlier.

4.7. Particle physics constraints and future possibilities. – The neutrino observations from core collapse and the SN dynamics itself provide formidable laboratories for particle physics [34, 39, 40, 43, 213]. It was Georgiy Zatsepin who first pointed out that the neutrino burst from SN collapse offers an opportunity to measure the neutrino mass by the energy-dependent time-of-flight delay [214]

$$\Delta t = 5.1\text{ ms} \left(\frac{D}{10\text{ kpc}} \right) \left(\frac{10\text{ MeV}}{E_\nu} \right)^2 \left(\frac{m_\nu}{1\text{ eV}} \right)^2.$$

However, when the SN 1987A burst was measured, it provided a mass limit of about 20 eV [168, 215, 216], which even at that time was only marginally interesting and was soon superseded by laboratory limits. The neutrino signal of the next nearby SN could improve this at best to the eV range [217, 218]. It is more interesting to note that the restrictive sub-eV cosmological neutrino mass limits [219] assure that fast time variations

at the source will not be washed out by time-of-flight effects and thus are, in principle, detectable at IceCube [180, 181].

A time-of-flight argument can also be used to constraint a putative neutrino electric charge. It would lead to deflection in the galactic magnetic field and thus to an energy-dependent pulse dispersion in analogy to m_ν , providing $e_\nu \lesssim 3 \times 10^{-17} e$ [220, 221].

From a present-day perspective, the most interesting time-of-flight constraint, however, is the one between neutrinos and photons, testing the equality of the relativistic limiting propagation speed between the two species. SN physics dictates that the neutrino burst should arrive a few hours earlier than the optical brightening, in agreement with SN 1987A. Given the distance of about 160,000 light years one finds [222, 223]

$$\left| \frac{c_\nu - c_\gamma}{c_\gamma} \right| \lesssim 2 \times 10^{-9}.$$

At the time of this writing, this result plays a crucial role for possible interpretations of the apparent superluminal neutrino speed reported by the OPERA experiment [224], $(c_\nu - c_\gamma)/c_\gamma = (2.37 \pm 0.32_{\text{stat}} + 0.34/-0.24_{\text{sys}}) \times 10^{-5}$. No plausible interpretation for this measurement is available at present.

Both neutrinos and photons should be delayed by their propagation through the gravitational potential of the galaxy (Shapiro time delay) which is estimated to be a few months toward the Large Magellanic Cloud. The agreement between the arrival times within a few hours confirms a common time delay within about $0.7-4 \times 10^{-3}$, i.e. neutrinos and photons respond to gravity in the same way [225, 226]. This is the only experimental proof that neutrinos respond to gravity in the usual way. These results could be extended to include the propagation speed of gravitational waves if the next nearby SN is observed both in neutrinos and with gravitational wave detectors. The onset of both bursts would coincide with the SN bounce time to within a few ms and the coincidence could be measured with this precision [182, 183]. In view of the current discussion of superluminal neutrino propagation, such a measurement would provide important additional constraints on possible interpretations.

After core collapse, neutrinos are trapped in the SN core and energy is emitted on a neutrino diffusion time scale of a few seconds [227]. This basic picture was confirmed by the SN 1987A neutrino burst, indicating that the gravitational binding energy was not carried away in the form of some other radiation, more weakly coupled than neutrinos, that would escape directly without diffusion [228, 229, 230]. This “energy-loss argument” has been applied to a large number of cases, notably axions, Majorons, and right-handed neutrinos, often providing the most restrictive limits on the underlying particle-physics model; extensive reviews are Refs. [34, 39, 40, 43, 213]. More recently, the argument was applied to Kaluza-Klein gravitons [231, 232, 233, 234], light neutralinos [235], light dark matter particles [236], and unparticles [237, 238, 239]. While there is no good reason to doubt the validity of this widely used argument, it is based on very sparse data. Measuring a high-statistics neutrino signal from the next nearby SN would put these crucial results on much firmer experimental ground.

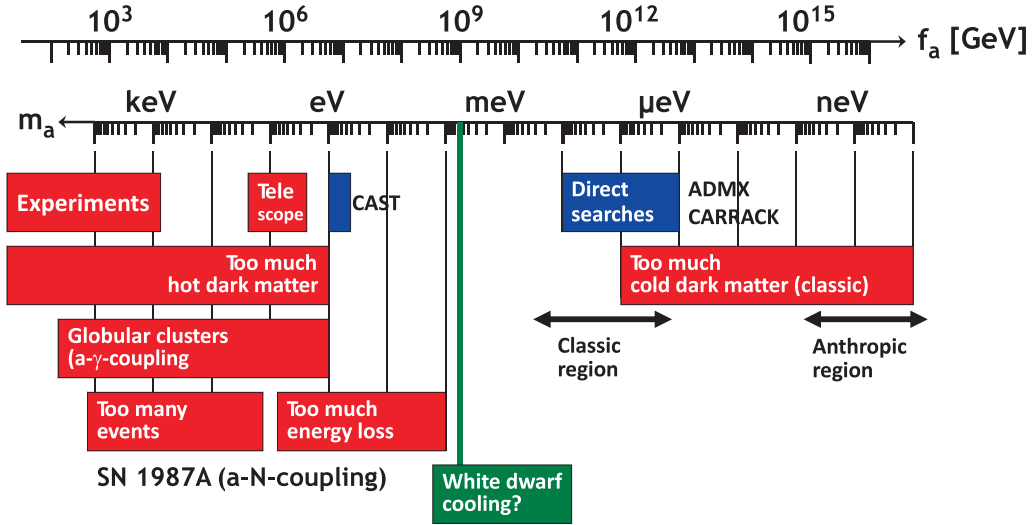


Fig. 58. – Summary of axion bounds, where red bars imply exclusion, green a tentative signature, and blue experimental search ranges [43].

Of particular interest are the SN 1987A axion bounds that squeeze the allowed m_a range to very small values below 10 meV (fig. 58). These bounds leave open the possibility that axions with a nonvanishing electron interaction could account for an additional white-dwarf cooling channel that may be suggested by observations as discussed earlier (see fig. 11). If the white-dwarf axion cooling interpretation were correct, axions would provide a significant energy-loss channel for SNe, although the axion burst from the next nearby SN would not be observable due to the extremely weak axion interactions. Still, the universe would be filled with a diffuse SN axion background (DSAB) with an energy density comparable to the DSNB [54]. Axions would be emitted from the inner SN core and thus have much larger energies than the emitted neutrinos, reflecting in a harder DSAB spectrum (fig. 59). So the universe could be filled with a significant amount of axion radiation that, however, appears to be nearly impossible to measure.

Conventional SN simulations are based on standard particle-physics assumptions that are not necessarily tested in the laboratory. In particular, lepton-number conservation is crucial in the collapse process because it ensures that the liberated gravitational energy is at first stored primarily in the degeneracy energy of electrons and electron neutrinos, i.e. the SN core after collapse is relatively cold. On the other hand, it is now commonly assumed that lepton number is not conserved in that neutrino masses are widely assumed to be of Majorana type. While neutrino Majorana masses would not suffice for significant lepton-number violating effects in a SN core, other sources of lepton-number violation may well be strong enough, e.g. R-parity violating supersymmetric models that in turn can induce Majorana masses. Therefore, it would be intriguing to study core collapse with “internal” deleptonization, leading to a hot SN core immediately after collapse.

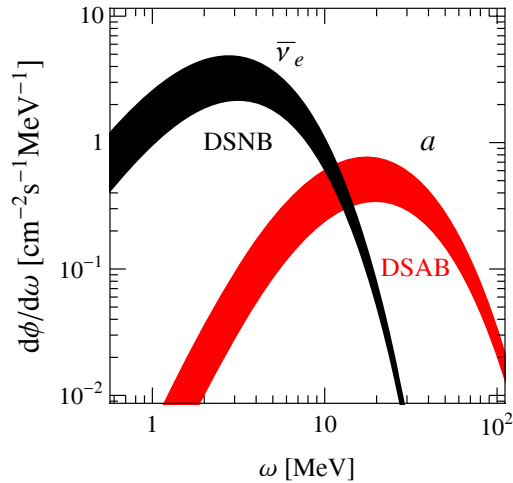


Fig. 59. – Diffuse SN axion background (DSAB) compared with the DSNB [54]. It was assumed that either neutrinos or axions carry away the full SN energy of 3×10^{53} erg. The width of the bands reflects only the uncertainty in the core collapse rate R_{cc} . For $\bar{\nu}_e$ a thermal spectrum with $T = 4$ MeV is assumed, carrying away 1/6 of the total energy, whereas for axions a bremsstrahlung-inspired spectrum with $T_{core} = 30$ MeV was assumed.

In a SN core, the matter potentials are so large that flavor conversion by oscillation is strongly suppressed even though some of the mixing angles are large. Therefore, the initial ν_e Fermi sea is conserved—in a SN core, flavor lepton number is effectively conserved. On the other hand, certain non-standard interactions (NSI) [240] that are not diagonal in flavor space would allow for flavor lepton number violation in collisions and therefore lead to a quick equipartition among flavors of the trapped lepton number. The required interaction strength is much smaller than what is typically envisioned for NSI effects on long-baseline neutrino oscillation experiments. In other words, a SN core is potentially the most sensitive laboratory for NSI effects. While it has been speculated that such effects would strongly modify the physics of core collapse [241, 242], a numerical simulation including the quick equipartition of flavors has never been performed.

4.8. Flavor oscillations of SN neutrinos. – Flavor conversion by neutrino oscillations is a large effect, for example for solar neutrinos, and will also be important for SN neutrinos, but not in the inner SN core. In this nuclear-density environment, the Wolfenstein matter effect is huge and propagation eigenstates are almost identical with weak interaction eigenstates, in spite of the large mixing angles. The weak potential difference of eq. (24) between ν_e and other flavors, that is around 0.2 peV in normal matter, is 14 orders of magnitude larger and thus a few tens of eV. As a consequence, the trapped electron lepton number is conserved on all time scales relevant for SN dynamics. Unless nonstandard flavor lepton number violating effects operate in a SN core, lepton number can disappear only on the neutrino diffusion time scale of seconds.

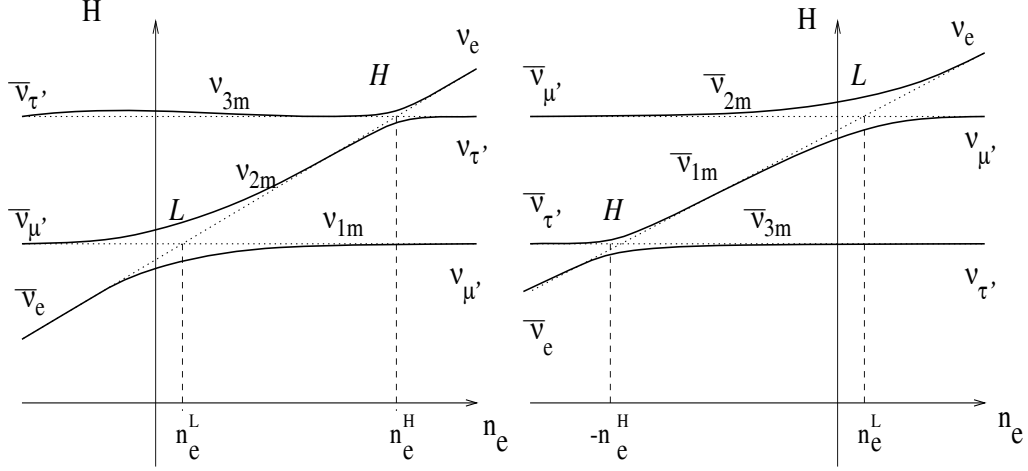


Fig. 60. – Three-flavor level diagram for neutrino propagation eigenmodes, in analogy to fig. 14, relevant for neutrinos streaming from a SN core [243] for normal hierarchy (left) and inverted hierarchy (right).

Of course, as neutrinos stream from the SN core through the stellar envelope, they will eventually encounter MSW resonances corresponding to the atmospheric mass difference (H resonance) and the solar mass difference (L resonance). The corresponding level diagram for the two mass hierarchies (fig. 60) allows one to determine in which mass eigenstate a neutrino will emerge that was produced in a given interaction eigenstate. Of particular interest is the MSW effect at the H-resonance driven by the 13-mixing angle. This resonance occurs in the neutrino sector for the normal mass hierarchy, and among anti-neutrinos for the inverted hierarchy. It is adiabatic for $\sin^2 \theta_{13} \gtrsim 10^{-3}$ and non-adiabatic for $\sin^2 \theta_{13} \lesssim 10^{-5}$. Therefore, the neutrino burst is, in principle, sensitive to the mass hierarchy and the 13-mixing angle [243, 244].

What arrives at Earth after propagation are mass eigenstates that need to be projected on interaction eigenstates to determine the detector response. The arriving flux relevant for detection can then be expressed in terms of the energy-dependent ν_e survival probability $p(E)$ in the form

$$(40) \quad F_{\nu_e} = p(E) F_{\nu_e}^0(E) + [1 - p(E)] F_{\nu_x}^0(E),$$

where the subscript 0 denotes the primary fluxes at emission. An analogous expression pertains to $\bar{\nu}_e$ with the survival probability $\bar{p}(E)$. Table XI summarizes the survival probabilities for different mixing scenarios, assuming that collective flavor conversions are not important (see below). The recent hints for a “large” value for θ_{12} discussed earlier suggest that the H resonance is adiabatic and we are in scenario A or B. The ν_e and $\bar{\nu}_e$ survival probabilities then distinguish between the normal and inverted mass hierarchy. How can this effect be measured?

TABLE XI. – *Survival probabilities for neutrinos, p , and antineutrinos, \bar{p} , in various mixing scenarios, assuming collective flavor conversion plays no role [243, 244].*

Scenario	Hierarchy	$\sin^2 \theta_{13}$	p	\bar{p}	Earth effects
A	Normal	$\gtrsim 10^{-3}$	0	$\cos^2 \theta_{12}$	$\bar{\nu}_e$
B	Inverted	$\gtrsim 10^{-3}$	$\sin^2 \theta_{12}$	0	ν_e
C	Any	$\gtrsim 10^{-5}$	$\sin^2 \theta_{12}$	$\cos^2 \theta_{12}$	ν_e and $\bar{\nu}_e$

The most pronounced flavor-dependent feature in the SN neutrino signal is the prompt ν_e burst, which in addition is rather model independent [142]. In the normal hierarchy, it would completely oscillate into the ν_x flavor so that it could not be seen in the charged-current (CC) channel of a liquid argon detector, whereas the electron-scattering signal would be reduced by about a factor of 7. On the other hand, in the inverted hierarchy, we would have $p = \sin^2 \theta_{12} \sim 0.30$ and thus a significant CC signal. Existing detectors, however, do not have a sufficient ν_e sensitivity for a clear detection.

Another option is to look for a signature in the $\bar{\nu}_e$ channel. During the accretion phase, the expected $\bar{\nu}_e$ and $\bar{\nu}_x$ fluxes are very different (fig. 39) so that the expected detection signal depends strongly on the oscillation scenario (fig. 61). However, in the absence of a quantitatively reliable prediction of the flavor-dependent fluxes and spectra it is difficult to distinguish between these cases. One model-independent signature would be the matter regeneration effect if the SN signal is received through the Earth in a “shadowed” position [205]. The Earth effect would imprint energy-dependent modulations on the received $\bar{\nu}_e$ signal (right panel of fig. 61) with a frequency that depends on the distance traveled through the Earth. In principle, these “wiggles” can be resolved, but not with present-day detectors [245]. With the water Cherenkov technique one would

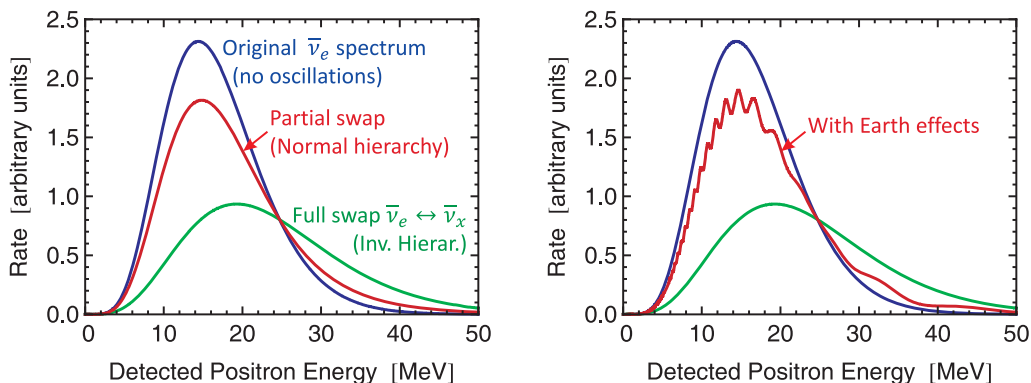


Fig. 61. – Accretion-phase $\bar{\nu}_e$ signal in water Cherenkov or scintillator detectors for different oscillation scenarios. For the regeneration effect (right panel) an 8000 km path length in the Earth is assumed.

need a megaton class detector, whereas with a scintillator detector a few thousand events would be enough due to the superior energy resolution. One may also compare the signals between a shadowed and an unshadowed detector [179]. The signal rise time is generically different between $\bar{\nu}_e$ and $\bar{\nu}_x$ (fig. 40) so that the rise time of the oscillated $\bar{\nu}_e$ signal depends on the mixing scenario. Conceivably, this signature can be used to determine the hierarchy, although the effect is subtle [246].

During the SN cooling phase, the shock wave propagates through the envelope, eventually disturbs the resonance region, and may imprint detectable features on the time-dependent neutrino flux [247, 248, 249, 250, 251]. Of course, the expectation of strong signatures was originally driven by the perception of a strong flavor dependence of the cooling fluxes that is not borne out by modern simulations with the full range of neutrino interaction channels. Therefore, any such signatures are likely somewhat subtle. Moreover, the matter behind the shock wave will exhibit stochastic density fluctuations from turbulent matter flows that can lead to flavor equilibration [252, 253].

A major new issue was recognized only a few years ago, the impact of collective or self-induced flavor conversions. The neutrinos streaming from the SN core are so dense that they provide a large matter effect for each other. The nonlinear nature of this neutrino-neutrino effect renders its consequences very different from the ordinary matter effect in that it results in collective oscillation phenomena [254, 255, 256, 257, 258] that can be of practical interest in the early universe for the oscillation of neutrinos with hypothetical primordial asymmetries [259, 260, 261, 262, 263]. These effects are also important in SNe in the region up to a few 100 km above the neutrino sphere [264, 265], an insight that has triggered a torrent of recent activities [266].

Collective effects are important in regions where the effective neutrino-neutrino interaction energy μ exceeds a typical vacuum oscillation frequency $\Delta m^2/2E$. In an isotropic ensemble we have $\mu \sim \sqrt{2}G_F n_\nu$ with n_ν the neutrino density. The current-current nature of low-energy weak interactions implies that a factor $1 - \cos\theta$ appears in the interaction potential where θ is the angle between neutrino trajectories. If the background is isotropic (approximately true for ordinary matter), this term averages to 1. On the other hand, neutrinos streaming from a SN core become more and more collinear with distance, so the average interaction potential is reduced by a suitable average $\langle 1 - \cos\theta \rangle$. One finds that μ effectively decreases with distance as r^{-4} where two powers derive from the geometric flux dilution, another two powers from the increasing collinearity. Therefore, collective effects are important only fairly close to the neutrino sphere.

Let us assume for now that collective effects are not affected by matter. Let us further assume that we have a pronounced hierarchy of number fluxes $F_{\nu_x} \ll F_{\bar{\nu}_e} < F_{\nu_e}$ that certainly applies after bounce and during the accretion phase, but probably does not apply during the cooling phase. In this scenario the impact of collective oscillations is straightforward. Nothing new happens for normal hierarchy (NH), whereas for the inverted hierarchy (IH) the $\bar{\nu}_e$ flux is swapped with the $\bar{\nu}_x$ flux. In addition, the ν_e flux is swapped with the ν_x flux, but only for $E > E_{\text{split}}$ where the energy E_{split} marks a sharp “spectral split,” separating the swapped part of the spectrum from the unswapped part (fig. 62). E_{split} is fixed by the condition that the net ν_e flux $F_{\nu_e} - F_{\bar{\nu}_e}$ is conserved [267].

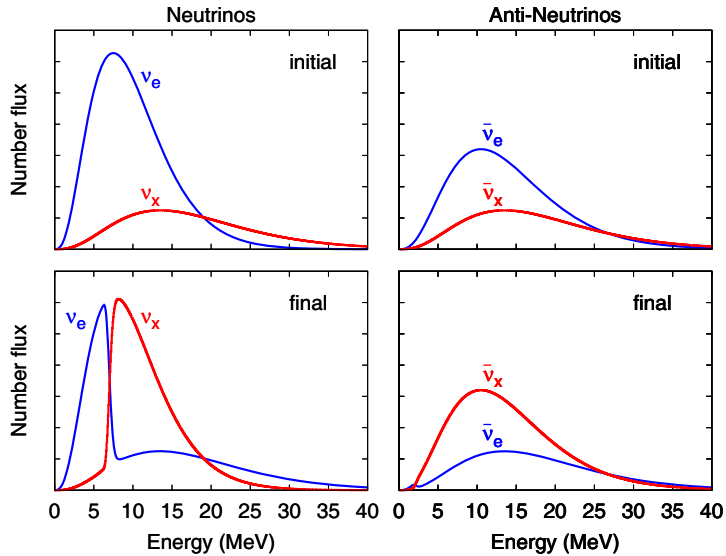


Fig. 62. – Example for SN neutrino spectra before and after collective oscillation, assuming inverted hierarchy and that ordinary matter does not suppress self-induced conversions.

In other words, there is no net flavor conversion: essentially one has self-induced collective pair conversions $\nu_e \bar{\nu}_e \rightarrow \nu_x \bar{\nu}_x$.

Collective oscillations at first seemed unaffected by matter because its influence does not depend on neutrino energies [265]. However, depending on emission angle, neutrinos accrue different matter-induced flavor-dependent phases until they reach a given radius. This “multi-angle matter effect” can suppress self-induced flavor conversion [268]. Based on schematic flux spectra, this was numerically confirmed for accretion-phase SN models where the density near the core is large [269]. Self-induced conversion requires that part of the spectrum is prepared in one flavor, the rest in another. The collective mode consists of pendulum-like flavor exchange between these parts without changing the overall flavor content [255, 270, 271]. The inevitable starting point is a flavor instability of the neutrino distribution caused by neutrino-neutrino refraction. An exponentially growing mode can be detected with a linearized analysis of the evolution equations [272, 273]. This method was applied to realistic multi-angle multi-energy neutrino fluxes and also confirm the suppression of self-induced conversion for the investigated accretion-phase models [274, 275]. If these results turn out to be generic, then for the accretion phase the survival probabilities of table XI remain applicable.

Likewise, the prompt ν_e burst should not be affected by collective oscillations with the possible exception of very low-mass progenitor stars. In this case the matter density is so low even at shock break out that the MSW region is very close to the possible collective oscillation region. In this case, interesting combined effects between MSW and collective conversion have been identified [276, 277, 278].

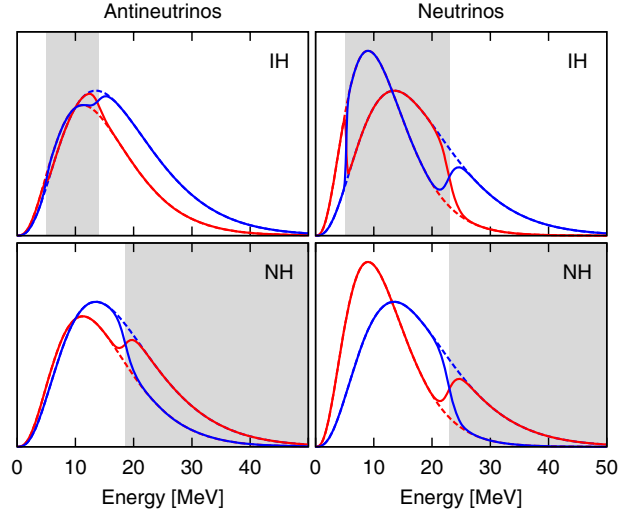


Fig. 63. – Example for possible cooling phase SN neutrino spectra before (dashed lines) and after (solid lines) collective oscillations, but before possible MSW conversions [279]. The panels are for ν and $\bar{\nu}$, each time for inverted hierarchy (IH) and normal hierarchy (NH). Red lines e -flavor, blue x -flavor. Shaded regions mark swap intervals.

During the cooling phase, the matter profile has become so low that self-induced flavor conversions can operate unimpeded. The flavor hierarchy of fluxes and spectral energies is not large, allowing for more complicated conversion patterns—see fig. 63 for an example. Multiple spectral swaps and splits are possible [279], where however multi-angle effects play a crucial role [273, 280, 281]. At the present time it is not obvious if one can arrive at generic predictions for what happens during the cooling phase. The interacting neutrino gas, however, remains a fascinating system for collective motions of what is effectively an interacting spin system [282, 283, 284], with analogies in the area of superconductivity [285, 286].

5. – Conclusion

The physics of stars is inseparably intertwined with that of neutrinos and we have discussed some of the many fascinating topics at the interface of these fields. Solar neutrinos play a special role in that the measured ν_e flux provided first evidence for flavor oscillations: a deep particle-physics issue was directly connected to low-energy neutrino astronomy. Learning about the exact chemical composition of the solar interior is the next frontier of solar neutrino spectroscopy. Beyond the Sun, neutrinos play a crucial role as an energy-loss channel that is a necessary ingredient for understanding stellar evolution. In the same spirit, we can use observed properties of stars, notably in globular clusters, to learn about neutrinos, such as their electromagnetic properties, or about other low-mass particles such as axions. These hypothetical particles would

also emerge from the Sun. The search for solar axions with the CAST experiment has provided important constraints and a next-generation axion helioscope is being discussed. It would probe deeply into realistic parameter space.

Of course, the royal discipline of neutrino astrophysics is their role in stellar core collapse and the dynamics of supernova explosions. SN 1987A remains the only observed astrophysical neutrino source other than the Sun. It has confirmed our basic understanding of supernova physics and has provided several particle-physics limits that remain of topical interest to date. Detecting the diffuse neutrino background from all past supernovae in the universe is the next milestone for low-energy neutrino astronomy. A high-statistics neutrino observation of the next nearby supernova with one of the operating or future large-scale experiments will provide a bonanza of astrophysical, neutrino and particle-physics information. Many questions remain open about supernova dynamics, nucleosynthesis in the neutrino-driven wind, and flavor oscillations in an environment of dense matter and neutrinos. The next generation of large-scale detectors remains to be developed and built. So while we wait for the next supernova neutrino observation, a lot of numerical, theoretical, and experimental work remains to be done.

* * *

Partial support by the Deutsche Forschungsgemeinschaft under Grants No. TR 27 and EXC 153 is acknowledged.

REFERENCES

- [1] H. A. Bethe, Phys. Rev. **55** (1939) 434.
- [2] C. F. von Weizsäcker, Physikalische Zeitschrift **38** (1937) 176; *ibid.* **39** (1938) 633.
- [3] G. Gamow and M. Schoenberg, Phys. Rev. **58** (1940) 1117.
- [4] G. Gamow and M. Schoenberg, Phys. Rev. **59** (1941) 539.
- [5] W. Baade and F. Zwicky, Proc. Nat. Acad. Sci. **20** (1934) 259.
- [6] B. T. Cleveland et al., Astrophys. J. **496** (1998) 505.
- [7] D. D. Clayton, *Principles of Stellar Evolution and Nucleosynthesis* (Univ. of Chicago Press, 1968).
- [8] R. Kippenhahn and A. Weigert, *Stellar Structure and Evolution* (Springer-Verlag, 1990).
- [9] F. Zwicky, Helv. Phys. Acta **6** (1933) 110.
- [10] R. Bonetti et al. (LUNA Collaboration), Phys. Rev. Lett. **82** (1999) 5205.
- [11] S. Chandrasekhar, Astrophys. J. **74** (1931) 81.
- [12] T. A. Weaver, G. B. Zimmerman and S. E. Woosley, Astrophys. J. **225** (1978) 1021.
- [13] G. Raffelt and D. Seckel, Phys. Rev. D **52** (1995) 1780.
- [14] K. Nakamura et al. (Particle Data Group), J. Phys. G **37** (2010) 075021.
- [15] R. B. Stothers, Phys. Rev. Lett. **24** (1970) 538.
- [16] F. J. Hasert et al., Phys. Lett. B **46** (1973) 121 and 138.
- [17] E. Braaten and D. Segel, Phys. Rev. D **48** (1993) 1478.
- [18] N. Itoh, H. Hayashi and A. Nishikawa, Astrophys. J. Suppl. **102** (1996) 411.
- [19] M. Haft, G. Raffelt and A. Weiss, Astrophys. J. **425** (1994) 222; (E) *ibid.* **438** (1995) 1017.
- [20] N. Itoh, A. Nishikawa and K. Yasuharu, Astrophys. J. **470** (1996) 1015.
- [21] J. Bernstein, M. Ruderman and G. Feinberg, Phys. Rev. **132** (1963) 1227.

- [22] J. Schechter and J. W. F. Valle, Phys. Rev. D **24** (1981) 1883; (E) *ibid.* **25** (1982) 283.
- [23] E. K. Akhmedov, Phys. Lett. B **213** (1988) 64.
- [24] C. S. Lim and W. J. Marciano, Phys. Rev. D **37** (1988) 1368.
- [25] O. G. Miranda, T. I. Rashba, A. I. Rez and J. W. F. Valle, Phys. Rev. Lett. **93** (2004) 051304.
- [26] O. G. Miranda, T. I. Rashba, A. I. Rez and J. W. F. Valle, Phys. Rev. D **70** (2004) 113002.
- [27] G. Raffelt and T. Rashba, Phys. Atom. Nucl. **73** (2010) 609.
- [28] S. Ando and K. Sato, Phys. Rev. D **68** (2003) 023003.
- [29] E. K. Akhmedov and T. Fukuyama, JCAP **0312** (2003) 007.
- [30] A. G. Beda et al., Phys. Part. Nucl. Lett. **7** (2010) 667.
- [31] G. G. Raffelt, Phys. Rev. Lett. **81** (1998) 4020.
- [32] M. T. Ressell and M. S. Turner, Comments Astrophys. **14** (1990) 323.
- [33] S. D. Biller et al., Phys. Rev. Lett. **80** (1998) 2992.
- [34] G. G. Raffelt, *Stars as laboratories for fundamental physics* (University of Chicago Press 1996).
- [35] W. E. Harris, “Catalog of parameters of Milky Way globular clusters” (2010 edition), <http://physwww.physics.mcmaster.ca/~harris/mwgc.dat>
- [36] W. E. Harris, “Globular clusters: The view from HST,” Proc. Space Telescope Science Institute Symposium (Baltimore, MD, USA, 11–14 April 2000), ed. by M. Livio, K. Noll, M. Stiavelli. Space Telescope Science Institute Symposium Series, Vol. 14 (Cambridge University Press, 2003), pp 78–100.
- [37] G. G. Raffelt, Astrophys. J. **365** (1990) 559.
- [38] M. Catelan, J. A. d. Pacheco and J. E. Horvath, Astrophys. J. **461** (1996) 231.
- [39] G. G. Raffelt, Phys. Rept. **198** (1990) 1.
- [40] G. G. Raffelt, Ann. Rev. Nucl. Part. Sci. **49** (1999) 163.
- [41] R. D. Peccei, Lect. Notes Phys. **741** (2008) 3.
- [42] P. Sikivie, Lect. Notes Phys. **741** (2008) 19.
- [43] G. G. Raffelt, Lect. Notes Phys. **741** (2008) 51.
- [44] J. E. Kim and G. Carosi, Rev. Mod. Phys. **82** (2010) 557.
- [45] M. Dine, W. Fischler and M. Srednicki, Phys. Lett. B **104** (1981) 199.
- [46] A. R. Zhitnitsky, Sov. J. Nucl. Phys. **31** (1980) 260 [Yad. Fiz. **31** (1980) 497].
- [47] G. Raffelt and A. Weiss, Phys. Rev. D **51** (1995) 1495.
- [48] G. G. Raffelt, Phys. Lett. B **166** (1986) 402.
- [49] J. Isern, E. García-Berro, S. Torres and S. Catalán, Astrophys. J. Lett. **682** (2008) L109.
- [50] J. Isern, S. Catalán, E. García-Berro and S. Torres, J. Phys. Conf. Ser. **172** (2009) 012005.
- [51] J. Isern, M. Hernanz and E. García-Berro, Astrophys. J. **392** (1992) L23.
- [52] J. Isern, E. García-Berro, L. G. Althaus and A. H. Corsico, Astron. Astrophys. **512** (2010) A86.
- [53] A. H. Corsico, L. G. Althaus, A. D. Romero, M. M. M. Bertolami, E. García-Berro and J. Isern, arXiv:1108.3541.
- [54] G. G. Raffelt, J. Redondo and N. Viaux Maira, Phys. Rev. D **84** (2011) 103008.
- [55] J. N. Bahcall, A. M. Serenelli and S. Basu, Astrophys. J. **621** (2005) L85.
- [56] J. N. Bahcall and A. M. Serenelli, Astrophys. J. **626** (2005) 530.
- [57] W. C. Haxton and W. Lin, Phys. Lett. B **486** (2000) 263.
- [58] A. M. Serenelli, W. C. Haxton and C. Peña-Garay, Astrophys. J. **743** (2011) 24.
- [59] R. Davis, Phys. Rev. Lett. **12** (1964) 303.
- [60] J. N. Bahcall, Phys. Rev. Lett. **12** (1964) 300.
- [61] R. J. Davis, Phys. Rev. **97** (1955) 766.
- [62] R. J. Davis, D. S. Harmer and K. C. Hoffman, Phys. Rev. Lett. **20** (1968) 1205.

- [63] V. N. Gribov and B. Pontecorvo, *Phys. Lett. B* **28** (1969) 493.
- [64] L. Wolfenstein, *Phys. Rev. D* **17** (1978) 2369.
- [65] S. P. Mikheev and A. Yu. Smirnov, *Sov. J. Nucl. Phys.* **42** (1985) 913 [*Yad. Fiz.* **42** (1985) 1441].
- [66] H. A. Bethe, *Phys. Rev. Lett.* **56** (1986) 1305.
- [67] M. Altmann et al. (GNO Collaboration), *Phys. Lett. B* **616** (2005) 174.
- [68] J. N. Abdurashitov et al. (SAGE Collaboration), *Phys. Rev. C* **80** (2009) 015807.
- [69] S. Fukuda et al. (Super-Kamiokande Collaboration), *Phys. Rev. Lett.* **86** (2001) 5651.
- [70] K. Abe et al. (Super-Kamiokande Collaboration), *Phys. Rev. D* **83** (2011) 052010.
- [71] J. N. Bahcall, P. I. Krastev and A. Yu. Smirnov, *Phys. Rev. D* **58** (1998) 096016.
- [72] Y. Fukuda et al. (Super-Kamiokande Collaboration), *Phys. Rev. Lett.* **81** (1998) 1562.
- [73] S. Fukuda et al. (Super-Kamiokande Collaboration), *Phys. Rev. Lett.* **86** (2001) 5656.
- [74] Q. R. Ahmad et al. (SNO Collaboration), *Phys. Rev. Lett.* **89** (2002) 011301.
- [75] K. Eguchi et al. (KamLAND Collaboration), *Phys. Rev. Lett.* **90** (2003) 021802.
- [76] S. Abe et al. (KamLAND Collaboration), *Phys. Rev. Lett.* **100** (2008) 221803.
- [77] G. Bellini et al., *Phys. Rev. Lett.* **107** (2011) 141302.
- [78] G. Bellini, Talk at TAUP 2011 conference, Munich, 5–9 Sept. 2011, <http://taup2011.mpp.mpg.de>
- [79] G. L. Fogli, E. Lisi, A. Marrone, A. Palazzo and A. M. Rotunno, *Phys. Rev. D* **84** (2011) 053007.
- [80] M. C. Gonzalez-Garcia, M. Maltoni and J. Salvado, *JHEP* **1004** (2010) 056
- [81] H. De Kerret (for the Double Chooz Collaboration), Talk at LowNu, Seoul, Nov. 11, 2011 <http://workshop.kias.re.kr/lownu11>
- [82] J. Christensen-Dalsgaard, “Lecture notes on stellar oscillations,” <http://users-phys.au.dk/jcd/oscilnotes>
- [83] A. Serenelli, arXiv:1109.2602.
- [84] N. Grevesse and A. J. Sauval, *Space Sci. Rev.* **85** (1998) 161.
- [85] M. Asplund, N. Grevesse, A. J. Sauval and P. Scott, *Ann. Rev. Astron. Astrophys.* **47** (2009) 481.
- [86] E. Caffau, H.-G. Ludwig, M. Steffen, B. Freytag and P. Bonifacio, *Sol. Phys.* **268** (2011) 255.
- [87] G. Mention, M. Fechner, T. Lasserre, T. A. Mueller, D. Lhuillier, M. Cribier and A. Letourneau, *Phys. Rev. D* **83** (2011) 073006.
- [88] G. Bellini et al. (Borexino Collaboration), *Phys. Lett. B* **696** (2011) 191.
- [89] G. G. Raffelt, *Phys. Rev. D* **31** (1985) 3002.
- [90] G. Raffelt and L. Stodolsky, *Phys. Lett. B* **119** (1982) 323.
- [91] P. Sikivie, *Phys. Rev. Lett.* **51** (1983) 1415; (E) *ibid.* **52** (1984) 695.
- [92] G. Raffelt and L. Stodolsky, *Phys. Rev. D* **37** (1988) 1237.
- [93] D. M. Lazarus et al., *Phys. Rev. Lett.* **69** (1992) 2333.
- [94] S. Moriyama, M. Minowa, T. Namba, Y. Inoue, Y. Takasu and A. Yamamoto, *Phys. Lett. B* **434** (1998) 147.
- [95] Y. Inoue, T. Namba, S. Moriyama, M. Minowa, Y. Takasu, T. Horiuchi and A. Yamamoto, *Phys. Lett. B* **536** (2002) 18.
- [96] Y. Inoue, Y. Akimoto, R. Ohta, T. Mizumoto, A. Yamamoto and M. Minowa, *Phys. Lett. B* **668** (2008) 93.
- [97] K. Zioutas et al. (CAST Collaboration), *Phys. Rev. Lett.* **94** (2005) 121301.
- [98] S. Andriamonje et al. (CAST Collaboration), *JCAP* **0704** (2007) 010.
- [99] E. Arik et al. (CAST Collaboration), *JCAP* **0902** (2009) 008.
- [100] M. Arik et al. (CAST Collaboration), *Phys. Rev. Lett.* **107** (2011) 261302.

- [101] K. van Bibber, P. M. McIntyre, D. E. Morris and G. G. Raffelt, *Phys. Rev. D* **39** (1989) 2089.
- [102] S. Hannestad, A. Mirizzi, G. G. Raffelt and Y. Y. Y. Wong, *JCAP* **1008** (2010) 001.
- [103] I. G. Irastorza et al., *JCAP* **1106** (2011) 013.
- [104] H. Schlattl, A. Weiss and G. Raffelt, *Astropart. Phys.* **10** (1999) 353.
- [105] P. Gondolo and G. Raffelt, *Phys. Rev. D* **79** (2009) 107301.
- [106] A. Burrows, *Ann. Rev. Nucl. Part. Sci.* **40** (1990) 181.
- [107] A. Burrows, *Nature* **403** (2000) 727.
- [108] H.-T. Janka, K. Langanke, A. Marek, G. Martínez-Pinedo and B. Müller, *Phys. Rept.* **442** (2007) 38.
- [109] L. Scheck, K. Kifonidis, H.-T. Janka and E. Müller, *Astron. Astrophys.* **457** (2006) 963.
- [110] A. Wongwathanarat, H.-T. Janka and E. Müller, *Astrophys. J.* **725** (2010) L106.
- [111] E. Cappellaro and M. Turatto, “Supernova types and rates,” in: *The influence of binaries on stellar population studies* (Dordrecht: Kluwer Academic Publishers, 2001) [astro-ph/0012455].
- [112] A. Goobar and B. Leibundgut, *Ann. Rev. Nucl. Part. Sci.* **61** (2011) 251.
- [113] S. Perlmutter et al. (Supernova Cosmology Project), *Astrophys. J.* **517** (1999) 565.
- [114] A. G. Riess et al. (Supernova Search Team), *Astron. J.* **116** (1998) 1009.
- [115] O. Krause, M. Tanaka, T. Usuda, T. Hattori, M. Goto, S. Birkmann and K. Nomoto, *Nature* **456** (2008) 617.
- [116] S. A. Colgate, W. H. Grasberger and R. H. White, *Astron. J.* **70** (1961) 280.
- [117] S. A. Colgate and R. H. White, *Astrophys. J.* **143** (1966) 626.
- [118] J. R. Wilson, “Supernovae and post-collapse behavior,” in: *Numerical Astrophysics, Proc. Symposium in honour of James R. Wilson, held at the University of Illinois Urbana Champaign, October, 1982*. Ed. by J. M. Centrella, J. M. LeBlanc and R. L. Bowers (Boston: Jones and Bartlett Publ., 1985) p. 422.
- [119] H. A. Bethe and J. R. Wilson, *Astrophys. J.* **295** (1985) 14.
- [120] D. Z. Freedman, *Phys. Rev. D* **9** (1974) 1389.
- [121] D. Z. Freedman, D. N. Schramm and D. L. Tubbs, *Ann. Rev. Nucl. Part. Sci.* **27** (1977) 167.
- [122] D. N. Schramm and J. R. Wilson, *Astrophys. J.* **260** (1982) 868.
- [123] Z. Berezhiani and A. Drago, *Phys. Lett. B* **473** (2000) 281.
- [124] G. M. Fuller, R. Mayle, B. S. Meyer and J. R. Wilson, *Astrophys. J.* **389** (1992) 517.
- [125] Y. Suwa, K. Kotake, T. Takiwaki, M. Liebendörfer and K. Sato, *Astrophys. J.* **738** (2011) 165.
- [126] B. Dasgupta, E. P. O’Connor and C. D. Ott, *Phys. Rev. D* **85** (2012) 065008.
- [127] J. Hidaka and G. M. Fuller, *Phys. Rev. D* **76** (2007) 083516.
- [128] G. M. Fuller, A. Kusenko and K. Petraki, *Phys. Lett. B* **670** (2009) 281.
- [129] F. S. Kitaura, H.-T. Janka and W. Hillebrandt, *Astron. Astrophys.* **450** (2006) 345.
- [130] F. Hanke, A. Marek, B. Müller and H.-T. Janka, arXiv:1108.4355.
- [131] J. M. Blondin, A. Mezzacappa and C. DeMarino, *Astrophys. J.* **584** (2003) 971.
- [132] N. Ohnishi, K. Kotake and S. Yamada, *Astrophys. J.* **641** (2006) 1018.
- [133] T. Foglizzo, P. Galletti, L. Scheck and H.-T. Janka, *Astrophys. J.* **654** (2007) 1006.
- [134] A. Marek, H.-T. Janka and E. Müller, *Astron. Astrophys.* **496** (2009) 475.
- [135] J. W. Murphy, C. D. Ott and A. Burrows, *Astrophys. J.* **707** (2009) 1173.
- [136] A. Marek and H.-T. Janka, *Astrophys. J.* **694** (2009) 664.
- [137] C. Y. Cardall, *Nucl. Phys. Proc. Suppl.* **217** (2011) 275.
- [138] J. Nordhaus, A. Burrows, A. Almgren and J. Bell, *Astrophys. J.* **720** (2010) 694.
- [139] A. Burrows, E. Livne, L. Dessart, C. D. Ott and J. Murphy, *Astrophys. J.* **655** (2007) 416.

- [140] C. J. Horowitz, Phys. Rev. D **65** (2002) 043001.
- [141] T. Fischer, S. C. Whitehouse, A. Mezzacappa, F. K. Thielemann and M. Liebendörfer, Astron. Astrophys. **517** (2010) A80.
- [142] M. Kachelriess, R. Tomàs, R. Buras, H.-T. Janka, A. Marek and M. Rampp, Phys. Rev. D **71** (2005) 063003.
- [143] K. Langanke, G. Martínez-Pinedo and J. M. Sampaio, Phys. Rev. C **64** (2001) 055801.
- [144] L. Hüdepohl, B. Müller, H.-T. Janka, A. Marek and G. G. Raffelt, Phys. Rev. Lett. **104** (2010) 251101; (E) *ibid.* **105** (2010) 249901.
- [145] T. Totani, K. Sato, H. E. Dalhed and J. R. Wilson, Astrophys. J. **496** (1998) 216.
- [146] M. T. Keil, G. G. Raffelt and H.-T. Janka, Astrophys. J. **590** (2003) 971.
- [147] A. Burrows and J. M. Lattimer, Astrophys. J. **307** (1986) 178.
- [148] W. Keil and H.-T. Janka, Astron. Astrophys. **296** (1995) 145.
- [149] H. Suzuki, Numer. Astrophys. Japan **2** (1991) 267; *Frontiers of Neutrino Astrophysics*, ed. by H. Suzuki and K. Nakamura (Univ. Acad. Press, Tokyo, 1993), p. 219.
- [150] J. A. Pons, S. Reddy, M. Prakash, J. M. Lattimer and J. A. Miralles, Astrophys. J. **513** (1999) 780.
- [151] G. G. Raffelt, Astrophys. J. **561** (2001) 890.
- [152] R. Buras, M. Rampp, H.-T. Janka and K. Kifonidis, Astron. Astrophys. **447** (2006) 1049.
- [153] N. Panagia, “Distance to SN 1987 A and the LMC,” in: *New Views of the Magellanic Clouds*, IAU Symposium No. 190, Ed. by Y.-H. Chu, N. Suntzeff, J. Hesser and D. Bohlender, p. 549.
- [154] A. Gould and O. Uza, Astrophys. J. **494** (1998) 118.
- [155] K. Hirata et al. (Kamiokande-II Collaboration), Phys. Rev. Lett. **58** (1987) 1490.
- [156] K. Hirata et al. (Kamiokande-II Collaboration), Phys. Rev. D **38** (1988) 448.
- [157] R. M. Bionta et al. (IMB Collaboration), Phys. Rev. Lett. **58** (1987) 1494.
- [158] C. B. Bratton et al. (IMB Collaboration), Phys. Rev. D **37** (1988) 3361.
- [159] E. N. Alekseev, L. N. Alekseeva, V. I. Volchenko and I. V. Krivosheina, Pisma Zh. Eksp. Teor. Fiz. **45** (1987) 461 [JETP Lett. **45** (1987) 589].
- [160] E. N. Alekseev, L. N. Alekseeva, I. V. Krivosheina and V. I. Volchenko, Phys. Lett. B **205** (1988) 209.
- [161] V. L. Dadykin et al., Pisma Zh. Eksp. Teor. Fiz. **45** (1987) 464 [JETP Lett. **45** (1987) 593].
- [162] M. Aglietta et al., Europhys. Lett. **3** (1987) 1315.
- [163] V. S. Imshennik and O. G. Ryazhskaya, Pisma Astron. Zhurnal, **30** (2004) 17 [Astron. Lett. **30** (2004) 14].
- [164] M. Koshiha, Phys. Rept. **220** (1992) 229.
- [165] A. K. Mann, *Shadow of a star: The neutrino story of supernova 1987A* (Freeman, 1997).
- [166] W. D. Arnett, J. N. Bahcall, R. P. Kirshner and S. E. Woosley, Annu. Rev. Astron. Astrophys. **27** (1989) 629.
- [167] B. Jegerlehner, F. Neubig and G. Raffelt, Phys. Rev. D **54** (1996) 1194.
- [168] T. J. Loredo and D. Q. Lamb, Phys. Rev. D **65** (2002) 063002.
- [169] A. Mirizzi and G. G. Raffelt, Phys. Rev. D **72** (2005) 063001.
- [170] G. Pagliaroli, F. Vissani, M. L. Costantini and A. Ianni, Astropart. Phys. **31** (2009) 163.
- [171] P. Vogel and J. F. Beacom, Phys. Rev. D **60** (1999) 053003.
- [172] A. Strumia and F. Vissani, Phys. Lett. B **564** (2003) 42.
- [173] K. Scholberg, J. Phys. Conf. Ser. **203** (2010) 012079.
- [174] P. Antonioli et al., New J. Phys. **6** (2004) 114.
- [175] K. Scholberg, Astron. Nachr. **329** (2008) 337.
- [176] Supernova Early Warning System (SNEWS), <http://snews.bnl.gov/>
- [177] C. Pryor, C. E. Roos and M. S. Webster, Astrophys. J. **329** (1988) 335.

- [178] F. Halzen, J. E. Jacobsen and E. Zas, *Phys. Rev. D* **49** (1994) 1758 and **53** (1996) 7359.
- [179] A. S. Dighe, M. T. Keil and G. G. Raffelt, *JCAP* **0306** (2003) 005.
- [180] R. Abbasi et al. (IceCube Collaboration), *Astron. Astrophys.* 535 (2011) A109.
- [181] T. Lund, A. Marek, C. Lunardini, H.-T. Janka and G. Raffelt, *Phys. Rev. D* **82** (2010) 063007.
- [182] F. Halzen and G. G. Raffelt, *Phys. Rev. D* **80** (2009) 087301.
- [183] G. Pagliaroli, F. Vissani, E. Coccia and W. Fulgione, *Phys. Rev. Lett.* **103** (2009) 031102.
- [184] J. F. Beacom and M. R. Vagins, *Phys. Rev. Lett.* **93** (2004) 171101.
- [185] H. Watanabe et al. (Super-Kamiokande Collaboration), *Astropart. Phys.* **31** (2009) 320.
- [186] M. Apollonio et al. (CHOOZ Collaboration), *Phys. Rev. D* **61** (2000) 012001; *Eur. Phys. J. C* **27** (2003) 331.
- [187] K. A. Hochmuth, M. Lindner and G. G. Raffelt, *Phys. Rev. D* **76** (2007) 073001.
- [188] M. Wurm et al. (LENA Collaboration), *Astropart. Phys.* **35** (2012) 685.
- [189] J. F. Beacom, W. M. Farr and P. Vogel, *Phys. Rev. D* **66** (2002) 033001.
- [190] B. Dasgupta and J. F. Beacom, *Phys. Rev. D* **83** (2011) 113006.
- [191] P. R. Sala (ICARUS Collaboration), *Nucl. Phys. Proc. Suppl.* **217** (2011) 186.
- [192] I. Gil Botella and A. Rubbia, *JCAP* **0408** (2004) 001.
- [193] D. Autiero et al., *JCAP* **0711** (2007) 011.
- [194] J. Engel, G. C. McLaughlin and C. Volpe, *Phys. Rev. D* **67** (2003) 013005.
- [195] C. A. Duba et al., *J. Phys. Conf. Ser.* **136** (2008) 042077.
- [196] D. Väänänen and C. Volpe, *JCAP* **1110** (2011) 019.
- [197] S. van den Bergh and R. D. McClure, *Astrophys. J.* **425** (1994) 205.
- [198] E. Cappellaro, R. Evans and M. Turatto, *Astron. Astrophys.* **351** (1999) 459.
- [199] R. Diehl et al., *Nature* **439** (2006) 45. For a review of supernova rates from various methods see the supplementary material provided in the electronic version of the Nature article and in astro-ph/0601015.
- [200] R. G. Strom, *Astron. Astrophys.* **288** (1994) L1.
- [201] G. A. Tammann, W. Löffler and A. Schröder, *Astrophys. J. Suppl.* **92** (1994) 487.
- [202] E. N. Alekseev and L. N. Alekseeva, *Zh. Eksp. Teor. Fiz.* **95** (2002) 10 [*J. Exp. Theor. Phys.* **95** (2002) 5].
- [203] J. F. Beacom and P. Vogel, *Phys. Rev. D* **60** (1999) 033007.
- [204] R. Tomàs, D. Semikoz, G. G. Raffelt, M. Kachelriess and A. S. Dighe, *Phys. Rev. D* **68** (2003) 093013.
- [205] A. Mirizzi, G. G. Raffelt and P. D. Serpico, *JCAP* **0605** (2006) 012.
- [206] M. Ahlers, P. Mertsch and S. Sarkar, *Phys. Rev. D* **80** (2009) 123017.
- [207] A. Odrzywolek, M. Misiasek and M. Kutschera, *Astropart. Phys.* **21** (2004) 303.
- [208] M. D. Kistler, H. Yüksel, S. Ando, J. F. Beacom and Y. Suzuki, *Phys. Rev. D* **83** (2011) 123008.
- [209] M. Kowalski “Detecting extragalactic SNe at South Pole,” Talk at TAUP 2011 (Munich 5–9 Sept. 2011), <http://taup2011.mpp.mpg.de>
- [210] J. F. Beacom, *Ann. Rev. Nucl. Part. Sci.* **60** (2010) 439.
- [211] S. Horiuchi, J. F. Beacom and E. Dwek, *Phys. Rev. D* **79** (2009) 083013.
- [212] T. Bays et al. (Super-Kamiokande Collaboration), *Phys. Rev. D* **85** (2012) 052007.
- [213] D. N. Schramm, *Comments Nucl. Part. Phys.* **17** (1987) 239.
- [214] G. T. Zatsepin, *Pisma Zh. Eksp. Teor. Fiz.* **8** (1968) 333 [*JETP Lett.* **8** (1968) 205].
- [215] T. J. Loredo and D. Q. Lamb, *Annals N. Y. Acad. Sci.* **571** (1989) 601.
- [216] P. J. Kernan and L. M. Krauss, *Nucl. Phys. B* **437** (1995) 243.
- [217] J. F. Beacom and P. Vogel, *Phys. Rev. D* **58** (1998) 053010.
- [218] E. Nardi and J. I. Zuluaga, *Nucl. Phys. B* **731** (2005) 140.
- [219] K. N. Abazajian et al., *Astropart. Phys.* **35** (2011) 177.

- [220] G. Barbiellini and G. Cocconi, *Nature* **329** (1987) 21.
- [221] J. N. Bahcall, *Neutrino Astrophysics* (Cambridge University Press, 1989).
- [222] M. J. Longo, *Phys. Rev. D* **36** (1987) 3276.
- [223] L. Stodolsky, *Phys. Lett. B* **201** (1988) 353.
- [224] T. Adam et al. (OPERA Collaboration), arXiv:1109.4897.
- [225] M. J. Longo, *Phys. Rev. Lett.* **60** (1988) 173.
- [226] L. M. Krauss and S. Tremaine, *Phys. Rev. Lett.* **60** (1988) 176.
- [227] R. F. Sawyer, D. J. Scalapino and A. Soni, “The neutrino pulse from a newly born neutron star”, *Proc. Neutrino 1979*, Bergen, Norway, 18–22 June 1979, vol. 2, pg. 429.
- [228] G. Raffelt and D. Seckel, *Phys. Rev. Lett.* **60** (1988) 1793.
- [229] M. S. Turner, *Phys. Rev. Lett.* **60** (1988) 1797.
- [230] R. Mayle, J. R. Wilson, J. R. Ellis, K. A. Olive, D. N. Schramm and G. Steigman, *Phys. Lett. B* **203** (1988) 188; *Phys. Lett. B* **219** (1989) 515.
- [231] S. Cullen and M. Perelstein, *Phys. Rev. Lett.* **83** (1999) 268.
- [232] C. Hanhart, D. R. Phillips, S. Reddy and M. J. Savage, *Nucl. Phys. B* **595** (2001) 335.
- [233] C. Hanhart, J. A. Pons, D. R. Phillips and S. Reddy, *Phys. Lett. B* **509** (2001) 1.
- [234] S. Hannestad and G. G. Raffelt, *Phys. Rev. D* **67** (2003) 125008; (E) *ibid.* **69** (2004) 029901.
- [235] H. K. Dreiner, C. Hanhart, U. Langenfeld and D. R. Phillips, *Phys. Rev. D* **68** (2003) 055004.
- [236] P. Fayet, D. Hooper and G. Sigl, *Phys. Rev. Lett.* **96** (2006) 211302
- [237] H. Davoudiasl, *Phys. Rev. Lett.* **99** (2007) 141301.
- [238] S. Hannestad, G. Raffelt and Y. Y. Y. Wong, *Phys. Rev. D* **76** (2007) 121701.
- [239] S. Dutta and A. Goyal, *JCAP* **0803** (2008) 027.
- [240] C. Biggio, M. Blennow and E. Fernandez-Martinez, *JHEP* **0908** (2009) 090.
- [241] P. S. Amanik and G. M. Fuller, *Phys. Rev. D* **75** (2007) 083008.
- [242] O. Lychkovskiy, S. Blinnikov and M. Vysotsky, *Eur. Phys. J. C* **67** (2010) 213
- [243] A. S. Dighe and A. Yu. Smirnov, *Phys. Rev. D* **62** (2000) 033007.
- [244] A. Dighe, *Nucl. Phys. Proc. Suppl.* **143** (2005) 449.
- [245] A. S. Dighe, M. T. Keil and G. G. Raffelt, *JCAP* **0306** (2003) 006.
- [246] P. D. Serpico, S. Chakraborty, T. Fischer, L. Hüdepohl, H.-T. Janka and A. Mirizzi, *Phys. Rev. D* **85** (2012) 085031.
- [247] R. C. Schirato and G. M. Fuller, arXiv:astro-ph/0205390.
- [248] R. Tomàs, M. Kachelriess, G. Raffelt, A. Dighe, H.-T. Janka and L. Scheck, *JCAP* **0409** (2004) 015.
- [249] G. L. Fogli, E. Lisi, A. Mirizzi and D. Montanino, *JCAP* **0504** (2005) 002.
- [250] B. Dasgupta and A. Dighe, *Phys. Rev. D* **75** (2007) 093002.
- [251] S. Choubey, N. P. Harries and G. G. Ross, *Phys. Rev. D* **74** (2006) 053010.
- [252] A. Friedland and A. Gruzinov, arXiv:astro-ph/0607244.
- [253] G. L. Fogli, E. Lisi, A. Mirizzi and D. Montanino, *JCAP* **0606** (2006) 012.
- [254] J. Pantaleone, *Phys. Lett. B* **287** (1992) 128.
- [255] S. Samuel, *Phys. Rev. D* **48** (1993) 1462.
- [256] S. Samuel, *Phys. Rev. D* **53** (1996) 5382.
- [257] S. Pastor, G. G. Raffelt and D. V. Semikoz, *Phys. Rev. D* **65** (2002) 053011.
- [258] R. F. Sawyer, *Phys. Rev. D* **72** (2005) 045003.
- [259] A. D. Dolgov, S. H. Hansen, S. Pastor, S. T. Petcov, G. G. Raffelt and D. V. Semikoz, *Nucl. Phys. B* **632** (2002) 363.
- [260] Y. Y. Y. Wong, *Phys. Rev. D* **66** (2002) 025015.
- [261] K. N. Abazajian, J. F. Beacom and N. F. Bell, *Phys. Rev. D* **66** (2002) 013008.
- [262] S. Pastor, T. Pinto and G. G. Raffelt, *Phys. Rev. Lett.* **102** (2009) 241302.

- [263] G. Mangano, G. Miele, S. Pastor, O. Pisanti and S. Sarikas, JCAP **1103** (2011) 035; Phys. Lett. B **708** (2012) 1.
- [264] H. Duan, G. M. Fuller and Y.-Z. Qian, Phys. Rev. D **74** (2006) 123004.
- [265] H. Duan, G. M. Fuller, J. Carlson and Y.-Z. Qian, Phys. Rev. D **74** (2006) 105014.
- [266] H. Duan, G. M. Fuller and Y.-Z. Qian, Ann. Rev. Nucl. Part. Sci. **60** (2010) 569.
- [267] G. G. Raffelt and A. Yu. Smirnov, Phys. Rev. D **76** (2007) 081301; (E) *ibid.* D **77** (2008) 029903.
- [268] A. Esteban-Pretel, A. Mirizzi, S. Pastor, R. Tomàs, G. G. Raffelt, P. D. Serpico and G. Sigl, Phys. Rev. D **78** (2008) 085012.
- [269] S. Chakraborty, T. Fischer, A. Mirizzi, N. Saviano and R. Tomàs, Phys. Rev. D **84** (2011) 025002; Phys. Rev. Lett. **107** (2011) 151101.
- [270] S. Hannestad, G. Raffelt, G. Sigl and Y. Y. Y. Wong, Phys. Rev. D **74** (2006) 105010; (E) *ibid.* **76** (2007) 029901.
- [271] H. Duan, G. M. Fuller, J. Carlson and Y.-Z. Qian, Phys. Rev. D **75** (2007) 125005.
- [272] R. F. Sawyer, Phys. Rev. D **79** (2009) 105003.
- [273] A. Banerjee, A. Dighe and G. Raffelt, Phys. Rev. D **84** (2011) 053013.
- [274] S. Sarikas and G. Raffelt, Proc. HANSE 2011, arXiv:1110.5572.
- [275] S. Sarikas, G. G. Raffelt, L. Hüdepohl and H.-T. Janka, Phys. Rev. Lett. **108** (2012) 061101. S. Sarikas, I. Tamborra, G. Raffelt, L. Hüdepohl and H.-T. Janka, Phys. Rev. D, in press (2012), arXiv:1204.0971.
- [276] H. Duan, G. M. Fuller, J. Carlson and Y.-Z. Qian, Phys. Rev. Lett. **100** (2008) 021101.
- [277] B. Dasgupta, A. Dighe, A. Mirizzi and G. G. Raffelt, Phys. Rev. D **77** (2008) 113007 .
- [278] J. F. Cherry, M. R. Wu, J. Carlson, H. Duan, G. M. Fuller and Y.-Z. Qian, Phys. Rev. D **84** (2011) 105034.
- [279] B. Dasgupta, A. Dighe, G. G. Raffelt and A. Yu. Smirnov, Phys. Rev. Lett. **103** (2009) 051105.
- [280] G. G. Raffelt, Phys. Rev. D **78** (2008) 125015.
- [281] H. Duan and A. Friedland, Phys. Rev. Lett. **106** (2011) 091101.
- [282] A. B. Balantekin and Y. Pehlivan, J. Phys. G **34** (2007) 47.
- [283] G. G. Raffelt and I. Tamborra, Phys. Rev. D **82** (2010) 125004.
- [284] G. G. Raffelt, Phys. Rev. D **83** (2011) 105022.
- [285] Y. Pehlivan, A. B. Balantekin, T. Kajino and T. Yoshida, Phys. Rev. D **84** (2011) 065008.
- [286] E. A. Yuzbashyan, Phys. Rev. B **78** (2008) 184507.